The Synthesis and Characterization of AuPd Nanoparticle Catalysts for Systematically Investigating the Effects of Bimetallic Interactions on Catalytic Performance

by

Adria R Wilson

Department of Chemistry
Duke University

Date:_____

Approved:

_____
Benjamin Wiley, Supervisor

_____
H. Henry Lamb

_____
Stephen Craig

_____
David Beratan

Dissertation submitted in partial fulfillment of
the requirements for the degree of Doctor
of Philosophy in the Department of
Chemistry in the Graduate School
of Duke University

2014

ABSTRACT

The Synthesis and Characterization of AuPd Nanoparticle Catalysts for Systematically Investigating the Effects of Bimetallic Interactions on Catalytic Performance

by

Adria R Wilson

Department of Chemistry
Duke University

Date:_____
Approved:

_____
Benjamin Wiley, Supervisor

_____
H. Henry Lamb

_____
Stephen Craig

_____
David Beratan

An abstract of a dissertation submitted in partial fulfillment of the requirements for the degree of Doctor of Philosophy in the Department of Chemistry in the Graduate School of Duke University

2014

Abstract

Heterogeneous catalysts are a major energy-saving tool in industrial chemical processes, by reducing energy input requirements for reactions as well as waste disposal costs. Currently, platinum group metals are the industry standard in terms of performance and robustness. Unfortunately, the most valuable catalytic materials of today are also the most costly and scarce, and as such it is important to find ways to optimize catalysts to be as effective as possible and to use a minimum of precious metal. One method of doing this is by constructing bimetallic nanoparticles, which, in addition to lessening the amount of expensive active metal required per gram of catalyst, has been shown in many cases to improve the performance of the catalyst. Our current understanding of the mechanisms by which the introduction of a second element to a first alters its catalytic properties is limited by how well we can characterize the structure of a catalyst, and this has been a considerable challenge. By developing uniform bimetallic nanoparticle catalysts that can be tuned to discretely change either the composition of the particle or the morphology of the particle, we have systematically studied how two metals interact to change the pathway of catalysis. The gold-palladium (AuPd) system was employed to demonstrate this concept because of its simplicity and ubiquity in the literature. By altering the amounts of Pd precursor, reducing agent, and reaction quenching agent, as well as varying the rate of Pd ion incorporation to the reaction solution, 4.3 nm Au core particles were coated with Pd shells determined to be 0.7 ± 0.2, 1.9 ± 0.3, and 3.8 ± 0.8 atomic monolayers thick. Upon immobilization on silica and calcination and reduction at 300 °C, the particles transformed to alloys containing 10, 20.2, and 28.5% by weight Pd per particle. A variety of spectroscopic and microscopic characterization techniques were used to investigate the bimetallic particles'

ability to resist sintering during heating, as well as their propensity to absorb hydrogen into their bulk depending on the thickness of the Pd shell present. Testing the catalysts in the conversion of α-limonene to *p*-cymene demonstrated that the sintering resistance imparted by the inclusion of Au in the particles made the particles competitive in their selectivity to *p*-cymene; specifically, the 20 and 28.5% $AuPd/SiO_2$ catalysts achieved higher selectivity to *p*-cymene than a solution-synthesized Pd/SiO_2 control. The core-shell and alloy particles were compared to one another in low temperature ethylene hydrogenation reaction, and it was shown that conversion of ethylene over the 1.9 $Pd@Au/SiO_2$ catalyst is structure sensitive, with its rate of conversion before calcination and reduction measured to be ten times higher than it is afterwards, likely because of its unique ability to store hydrogen below its surface. In general, these reactions demonstrate that the interactions between Au and Pd may be described in terms of experimentally observable effects, which occur as a consequence of the traditionally described geometric and electronic effects under a given set of experimental conditions. Using composite effects such as these, rather than ones that are difficult to isolate, will render our heightened understanding of the effect of structure on catalytic function more directly practicable in developing better catalysts for specific reactions.

Contents

List of Tables

List of Figures

Acknowledgements

I would like to thank the Dr. Benjamin Wiley for not only his guidance regarding my research project, but for his role in helping to teach me the balance between determination and resilience that makes for a successful scientist. I am also indebted to Dr. H. Henry Lamb for his willingness to let me conduct research in his laboratory at N.C. State for the majority of my time in graduate school. Through his encouragement and commitment to thorough investigation, I have gained a breadth of knowledge and practical experience in catalysis that I wouldn't have acquired otherwise. The graduate students in both of these labs have also provided an intellectually rich space for me to do research, and I am very grateful for the open flow of ideas and discussions that came as a result of working alongside of them, research-centered or otherwise.

1. Introduction

Heterogeneous nanoparticle catalysts are an integral part of industrial chemical processes. They allow industrial reactions to proceed at lower temperatures and pressures than they would otherwise, thus lowering the energy cost of reaction, and can redirect a reaction pathway to select for only a desired product, thereby removing any cost required for separating and disposing of unwanted waste products.[1] Unlike their homogeneous counterparts, heterogeneous catalysts are also easily separable from liquid and gas phase reactions, making catalyst recovery and reuse straightforward while avoiding heavy metal waste generation or the use of organic solvents[2]. Solid catalysts have been studied extensively, but the extent of our understanding regarding how they work is limited by the inherent variability of the nanoparticles that constitute a typical catalyst.[3-6] This is even truer with regards to bimetallic nanocatalysts, which comprise of two metals dispersed upon a support material. In this case, there are two extra degrees of variability to consider: the relative composition of each particle, and the distribution of particle morphologies that are formed.[7, 8] To control these parameters for the sake of research requires careful nanoparticle construction, yet the most common methods of preparing industrial catalysts inherently produce non-uniform particles and offer no control over the bimetallic architecture of the particles formed.[3] In fact, many model catalysts that have been studied have been made in the fashion of industrial catalysts, resulting in similar distributions of particle shapes and sizes. With non-uniform catalysts like these, the most useful correlations that can be drawn are empirical ones between the synthesis used to make a catalyst and its performance.[1] However, in order to understand the interplay of two metals in bimetallic catalysts, and to begin attributing changes in catalyst performance to atomic scale structural changes, model

catalyst uniformity is key. To that end, developing monodisperse bimetallic nanoparticle catalysts that can have tunable compositions and elemental distributions, one can systematically study how two metals interact to change the pathway of catalysis.[4] With this foundation, we can better understand the factors that are affecting the behavior of more polydisperse industrial catalysts, and aim to alter those contributing characteristics by redesigning the overall structure of the catalyst such that a more efficient catalyst might be developed. Guided design of catalysts is still well in the future and is beyond the scope of this work, but is a motivating factor for it.

1.1 Methods for synthesizing particle catalysts

Using nanoparticles as catalysts has the so that most of the atoms are on the particle surface and can participate in adsorption.[1, 5] The high ratio of surface-to-bulk atoms inherent in nanomaterials also lends them unique characteristics. One of these is an increased surface energy due to a higher number of undercoordinated terrace, kink, and edge surface atoms.[6] Their electronic properties, also a consequence of dimensions that approach the atomic scale, are highly dependent upon particle size, shape, and composition, especially as their size decreases below 10 nm.[7] Taken together, these qualities make nanoparticles a medium that can be tuned to match their catalytic purpose. However, manipulate nanostructure properties effectively requires an understanding of the relationship between particle structure and performance that in turn necessitates study of controlled structures.

To that end, single crystal surface studies have been very useful in determining catalytic pathways on multi-element catalysts[4, 13-16], but the surfaces studied in these experiments are not representative of real catalysts and so fall short of adequately describing their behavior. Similarly, simulations can reveal valuable information about

the potential pathways of reactions over catalytic surfaces, but computational studies have yet to fully capture the environmental influences affecting a reaction.[16-18] Studies that do present work on well-controlled nanoparticle catalysts may or may not focus on a catalytically relevant size regime (>10 nm), a threshold above which the utility of the information gathered may not be relevant to the directed design of catalysts, since the electronic properties change rapidly as a function of size below this threshold.[19, 20]

Complicatedly, the very quality that makes nanoparticles ideal catalysts, i.e., their large proportion of undercoordinated surface sites, endows them with a propensity for rearranging morphologically and aggregating to reduce their surface energy.[5] To mitigate this, nanoparticle catalysts are often immobilized on or formed in the presence of an unreactive support material to prevent them from merging with one another.[21, 22] The timing of when the metal is introduced to the support material can be thought of as a parameter that divides the two main methods for producing heterogeneous catalysts. When metals are introduced to the support before having been formed into particles, by impregnation with a metal salt containing solution or similar methods, the catalysts produced often contain a wide range of nanoparticle sizes and compositions.[8-10] For example, in one study, the formation of Au and Pd particles on an alumina support by the incipient wetness impregnation method, in which a support material is titrated with metal precursor solution until its saturated and subsequently dried and reduced, resulted in distinct phases of the two metals on the support as shown by FTIR-CO and XRD analysis.[8]

Other methods in this regime of synthesis include the ion exchange preparation method, which employs charge-based interactions to localize metal ions before reduction to more fully disperse the metal material as smaller and more uniformly sized

particles. These approaches become insufficient for forming controlled structures when two metals are involved, because metals reduce to form nanoparticles that are not just variable in size but also in the composition of each particle and in the arrangement of metal in the particle. Much of the diversity in the particles produced by this method is inherent in the dispersion of the support pore structure.[1] In one instance that demonstrates this dependence, Co particles were formed by co-reduction in silica supports prepared to have pore diameters ranging from 3 to 22 nm, and it was shown that the variation affected the size and packing arrangement of the Co particles formed, as well as their activity in Fischer-Tropsch reaction.[9] Generally speaking, this method offers less than optimal control over the particle morphology.

Alternatively, by synthesizing nanoparticles prior to immobilizing them on a support material, one can exercise greater control over the uniformity of the particles (since there are no secondary nucleation sites in solution to complicate the temporal distribution of particle formation) and over the morphology of the particles.[9, 12] In this way, core-shell[10], alloy[7, 9, 28, 29], and other types[8, 11] of particles (like anisotropic[30-32] and high-facet particles[33, 34], which will not be discussed in detail here) can be formed and well-characterized before being employed as a catalyst. When nanoparticles are synthesized by solution phase methods before deposition onto a support, this technique is known as sol-immobilization. Even some of these sol-immobilization procedures can result in polydispersity depending on the method utilized.[12] As one might expect, two primary contributing factors to uniformity are the identity of the reducing agent and stabilizing agent employed in the synthesis. We can compare two such syntheses that both involve the co-reduction of chloroauric acid ($HAuCl_4$) and Pd chloride complexes to form alloy particles, for example, and find that utilizing polyvinyl alcohol as a

stabilizing agent and sodium borohydride as the reducing agent results in a nanoparticle size distribution of 2 - 6 nm[12], whereas employing cetyltetraammonium chloride as both reducing and stabilizing agent in addition to ascorbic acid (to equilibrate the reduction rates of the Au and Pd ions in solution) generates alloy nanoparticles that are 35 - 45 nm in diameter and octahedral in shape.[13] In the latter case, simply decreasing the amount of L-ascorbic acid in solution increases the size of the particles to 60 nm and truncates their octahedral shape, and completely removing the ascorbic acid from synthesis results in core-shell AuPd nanocrystals ranging between 36 and 42 nm in diameter.[13] Pairing L-ascorbic acid with polyvinylpyrrolidone (PVP) as the stabilizing agent with the same metal precursors, alternatively, can result in the formation of alloy nanoflower structures ranging between 24 and 28 nm in diameter, depending on the ratio of metal precursors used.[14]

As implied above, stabilizing agents are often a necessary addition to colloidal syntheses to prevent aggregation of the particles in solution, typically doing so by occupying otherwise undercoordinated surface sites on the particle during and/or after the reduction process.[15] Because surface sites necessarily need to be available on a catalyst, a stabilizing agent can prove detrimental to the effectiveness of a sol-derived catalyst if nothing is done to remove it.[4] In certain cases, the effect of a stabilizer on the surface of a particle may be more complicated than simply blocking active sites; it may effectively alter the route of binding to the surface and change the pathway of a reaction.[16] For example, rhodium (Rh) nanoparticles of a variety of sizes were synthesized in ordered, mesoporous silica (SBA-15) in the presence of PVP were used as CO oxidation catalysts before and after being heat-treated to remove the stabilizer. It was concluded that when PVP is left on the surface of the particles one sees a size-

dependent enhancement in catalysis. As particles decrease in size, the Rh particles are more active due to a combination of the ease of oxidation of smaller particles[10] and the propensity for CO to bind to the surface in bridging mode rather than atop mode when PVP is still on the surface.[17] Because the interaction of bridged CO with O_2 is size dependent, then, PVP on the surface imposes a size dependancy.[10] In another instance, where Au nanoparticles were synthesized using PVP, polyvinyl alcohol (PVA), and sodium citrate, three common stabilizing agents, and compared in the oxygen reduction reaction (ORR), it was found that PVP-coated particles were six times less active than the particles coated by either of the other materials once the sizes of the particles were accounted for.[10] The observed difference in size observed in particles in this study underlines again the pivotal role of stabilizers in affecting the overall structure of the nanoparticles formed in a synthesis, and how their strength of binding to the particle affects catalysis on its surface.

PVP is one of the most common stabilizing agents used in particle synthesis, and one of the more difficult to remove, as it covalently bonds to the surface of metal particles through its amino functional groups, may also hydrogen bond with solvents or surfaces through the electron-rich oxygen present on each monomer, and also possesses hydrophobic molecular components.[18] Thus, PVP can stabilize through multiple pathways, as opposed to associating with the metal surface solely through electrostatic surfaces or other weak binding interactions.[19] In order to completely remove PVP from the surface of a nanoparticle catalyst, it is generally accepted that the catalyst powder must be calcined, or heated in the presence of oxygen, at temperatures upwards of 573 K.[39, 43, 44] This is a non-trivial part of the catalyst preparation process, because introducing stabilized nanoparticles to heat can cause dramatic changes to the metal

nanoparticles themselves, spurring an increase in the size of the nanoparticles on the support, as well as potentially altering the distribution of two metals within the particle.[20] For example, when AuPd alloy nanoparticles are formed by impregnation on an alumina support and calcined in air at 400 °C for 4 h, Pd segregates to the outer edge of the particles, thereby forming core-shell particles.[20] Extra care must be taken when crafting catalysts from pre-formed, stabilized nanoparticles to find a method that will remove stabilizer from the surface without altering the structure of the particles. Failure to do so ultimately defeats the purpose of this type of preparation technique.

Since they are simpler, and typically one-pot synthetic procedures, methods in which nanoparticles are formed directly on the surface of the support structure - i.e. impregnation, ion exchange, and the like - are typically utilized in industrial catalyst generation.[1] The second category of preparation discussed above is clearly more intensive in several respects, as it includes multi-step particle syntheses, the extra steps required to immobilize the particles on a support and to remove stabilizer, and the several rounds of heat treatment required to accomplish this and then re-reduce any oxidized metal (although many times a heating step is necessary in impregnation techniques to form particles or reduce oxides that have formed before reaction[20]). However, catalysts made by sol-immobilization are a useful tool for understanding the more easily made but ultimately more complex catalysts used in industry, because of their uniformity and tunability.

1.2 Monometallic versus bimetallic particles

As is true for metals in the bulk, combining more than one metal in a nanoparticle catalyst alters the properties of the catalyst, and in the right combination can yield an enhancement in its catalytic properties.[3, 9, 20, 46-48] For example, adding a

small amount of ruthenium to cobalt improves the conversion, usually expressed as turnover frequency (TOF), rates of the Fischer Tropsch reaction and increases the selectivity of it to more valuable, higher carbon number products by preventing the deactivation of Co in presence of CO, a participating reactant but also a catalyst poison.[47, 49-52] Carbon-supported AuPd alloy nanoparticles of different metallic ratios, synthesized by the co-reduction of both metals by oleylamine in an organic-based solution, were used to catalyze the dehydrogenation of formic acid at 50 °C and it was found that a $Au_{41}Pd_{59}$ catalyst was 7.7 times more active than Pd alone and 2.9 times more than Au alone.[21] Adding Au to Pd catalysts used in the production of vinyl acetate monomer minimizes the formation of unwanted intermediates on the catalyst surface[22] and improves the rate of reaction three-fold compared to Pd catalysts alone.[23]

As might be intuitive, the relative arrangement of two metals within a bimetallic nanoparticle has a significant impact on its catalytic properties. To a certain extent, the organization of two metals within a nanoparticle can be controlled by the synthetic method chosen, as described in the previous section. It can also be controlled by reaction conditions that are employed, by changing the amount and identity of the reagents used, as exemplified by the discussion on PVP, as well as the timing of addition. Both alloyed and core-shell nanoparticles may be synthesized by making alterations of this sort to solution-based syntheses. Since alloy particles are by definition a homogeneous single phase of the two metals, it typically requires less of an effort to directly synthesize these, whether it be by colloidal synthesis or an impregnation technique.[24] Again, however, the colloidal technique of synthesis is superior due to the greater control afforded over particle structure and homogeneity.[25] In the case of AuPd on alumina, Pawelec *et al* compared two AuPd alloy syntheses: one involving reduction

by ethanol in the presence of PVP against a co-impregnation method, and observed a homogeneous alloy formation in the former case as opposed to separate phase formation in the latter.[8] Alloyed particles have also been formed by flame spray pyrolysis[8], a method that forms smaller and more uniform particles without requiring post-synthesis cleaning and filtering steps; however, the process requires specialized equipment and less environmentally-friendly, organic solvents.[26]

The generation of core-shell particles generally relies on the sequential reduction of two metals.[13] It is possible to influence the individual rates of reduction of two metals in solution simultaneously to this effect[13], but more often than not, this is accomplished by step-wise introduction of the metals throughout the synthesis.[9, 57, 58] For example, the Au_{core}-Pd_{shell} nanoparticles that are the focus of this work here were made by first reducing $HAuCl_4$ with sodium borohydride, and subsequently adding hydroquinone, a mild reducing agent, followed by Na_2PdCl_4 solution. There is particular value in utilizing core-shell nanoparticles as model catalysts, because their structures allow us to focus on the ways that an inert metal, such as Au, can influence an active metal, like Pd, *without* being on the surface of the particle.[9, 58] The bimetallic interactions that are the sources of catalytic enhancement will be discussed in detail in Section 1.4.

There are, of course, other types of nanoparticles that have been investigated in the literature, although they are less commonly used as model catalysts. Janus particles are those in which two materials make up two halves or hemispheres of a nanoparticle.[59, 60] They have been utilized as emulsifiers in catalytic reactions, where the two halves of the particles rest at the interface of a biphasic catalytic reaction; these make recoverability of a single phase possible without heating, and replace surfactants as an easily removable alternative.[27] These can be made by selectively depositing a metal on

one half of a nanoparticle surface. In some cases, the nanoparticle substrate is made of a support-like material, such as silicon oxide or carbon.[27] In such a case, when Pd was deposited selectively on either side of silica particle/carbon nanotube Janus hybrid particles, it was possible to selectively catalyze reactions in the aqueous[28] and oil[27] phases of a reaction, respectively. These particles are effectively a small-scale construction of a typical catalyst's global structure, with small Pd particles attached to bigger support particles. In another work, two-sided metal nanoparticles were used as a scaffold for introducing hydrophilic and hydrophobic characteristics to two sides of the same particle.[29] These particles were generated by capping metal particles with alkanethiol stabilizer and then employing the Langmuir film technique; the particles reside at the solution-air interface, and are refunctionalized only on the side in contact with the solution.[29] Three-band "Neapolitan" Au/Pt/Ag particles were also reported using this technique.[30]

This striped particle mentioned is in effect a special type of three-layer particle. Trimetallic particles are also present in the literature although much less commonly than either alloy or core-shell particles.[64, 65] Three-layer bimetallic Pd@Au@Pd nanoparticles were found to form when a Au shell was deposited on a Pd core in a solution-phase synthesis, but only when the particle was allowed to grow larger than 5 nm; investigation of these particles helped to elucidate the size-dependence of the interaction between Au and Pd in the formation process of these nanoparticles.[31] Three layer particles may also be utilized to minimize the amount of noble metal present per nanoparticle in a given system.[32] In one particular study, cobalt and nickel nanoparticles doped with a small amount of a noble metal (Au, Ag, or Pd) were heated to form a monolayer of the noble metal around the non-noble core, and then Cu was deposited

atop as a second monolayer by underpotential deposition (UPD).[32] The copper was galvanically displaced by Pt, forming a monolayer of the noble metal, and the catalytic performance of three such samples (Pt/Au/Ni, Pt/Pd/Co, and Pt/Pt/Co) were tested against a monometallic Pt/C catalyst in the electrocatalyzed reduction of oxygen. The second noble metal layer, in these reaction conditions, has a practical purpose - it protects the non-noble core metal from interacting with and dissolving into the acidic electrolyte during electrocatalysis - but fundamentally, it also offers a means for probing the effect of lattice strain caused by a variety of subsurface metal substrates (Au, Pd, and Pt in this case) on the d-band of the Pt residing at the surface and therefore its catalytic properties as well.[32]

Both of these particle types, because of the careful synthesis for the structural design, boast high monodispersity in shape and size, and present interesting structure types for analysis in catalytic reactions. However, this paper will not come back to the subject again, but rather focus on alloyed and bimetallic core-shell particles, which form a sufficient and equally interesting basis set of possible metal configurations to probe. The study of trimetallic particles adds a layer of complexity to structure-function investigations, and as such, there is not yet a great deal of work that focuses on catalytic enhancement produced as a result of the interactions of three separate metals.

1.3 Electronic and geometric effects on catalyst performance and the AuPd system

The effect of the bimetallic system on a reaction is very much a function of the chemical properties of the two metals that form the system. For example, Tedsree *et al* present data showing that the formic acid decomposition over M_{core}-Pd_{shell} nanoparticles

correlates linearly with the work function of the core metal M.[33] At least in monometallic systems, the concept of catalytic activity varying as a function of the element used is described by the Sabatier principle. This principle states that in order for a catalyst to be effective, substrate-adsorbate binding interaction must be neither too weak nor too strong.[34] Thus, plotting the rate of a given reaction and holding all else equal, as a function of heat of adsorption of different catalysts comprised of different elements or complexes results in a volcano-shaped relationship.[66, 67] Figure 1 illustrates the volcano-shaped relationship for the ammonia synthesis reaction over different transition metals as modeled by DFT.[35]

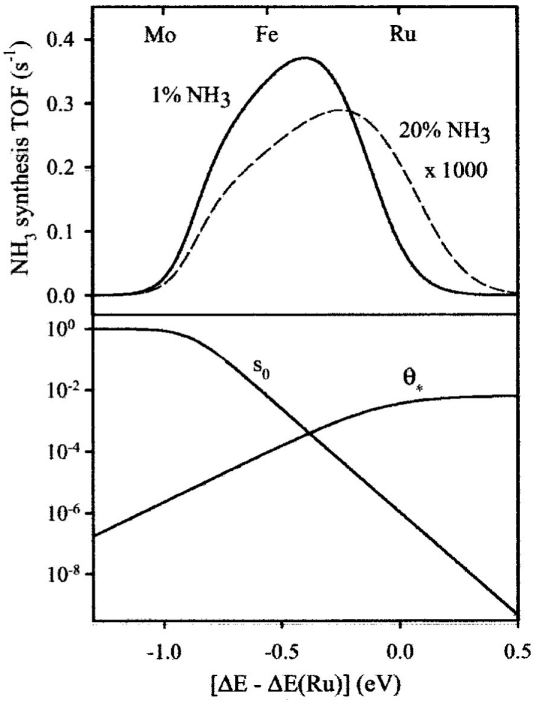

Figure 1: Rate of NH_3 synthesis over transition metals as a function of the heat of adsorption of N_2 on the metal surface.[35]

The catalytic activity over a surface is dependent on the adsorbate-metal bond strength, which is in turn intimately tied to the electronic character of the material. In

particular, the strength of adsorbate binding to the catalyst surface is tied to the position of the center of the metal's d-band, the degree of filling of the metal d-band, and the degree of interaction between the metal d-band and the adsorbate states involved.[36] A second example, shown in Figure 2, shows the clear relationship between the initial rate of formic acid decomposition and the d-band center of the metal used to catalyze the reaction.[33] Generally, as the degree of filling of the metal d-states increases (moving to the right on the periodic table), the metal-adsorbate bond strength decreases, thereby influencing the ability of the metal surface to effectively bind reactants and intermediates while catalyzing a reaction.[37]

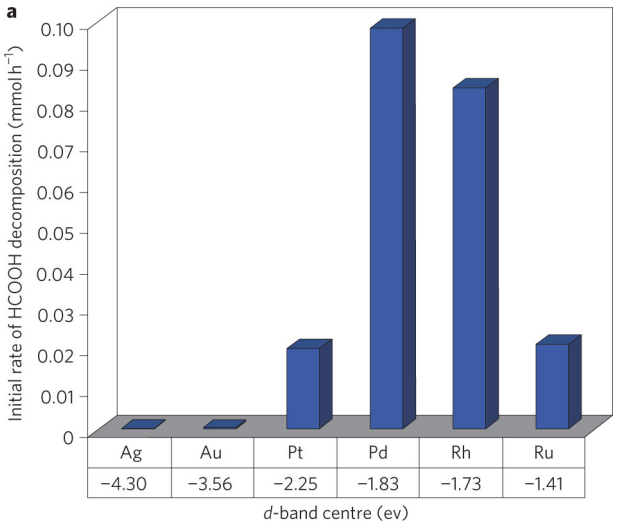

Figure 2: The initial rate of HCOOH decomposition as a function of d-band center over several metal catalyst surfaces.[33]

Since the electronic structure of a metal atom depends on the environment in which it exists, it is not surprising that introducing a second metal to a first either as an alloyed mixture or as a layer on a substrate (core-shell) considerably changes the electronics and therefore the activity of the metal, as seen already.[36, 38] In heterometallic

surfaces, charge transfers from the element with more electron density to the one with more vacancy in its d-state, and the larger the charge flow between dissimilar atoms, the greater the change in the nature of adsorbate binding to active metal sites on the surface.[38]

The influence of charge transfer on the catalytic properties of bimetallic catalysts is termed the electronic effect, and is one of the ways by which a metal, like Au can alter the activity of an active metal like Pd. For example, the inclusion of inactive Sn atoms in Pt nanoparticles supported on Nb_2O_5 weakens the adsorption of CO on Pt atoms present on the surface, caused by the transfer of electron density from Sn to Pt.[39] Generally speaking, then, electron transfer alters the binding properties of a surface and can in this way alter reaction pathways and rates.

Another principle intermetallic effect that alters the catalytic properties of a surface arises when a second metal is interspersed on the surface itself. This is termed the geometric, or ensemble effect. In this case, the second metal modulates the geometry of surface sites, breaking up multiatom ensembles of the first, active metal, and thereby altering the reaction pathway. Venezia *et al* studied the catalytic dehydrosulfurization capacity of AuPd alloy catalysts, and found them to be up to four times more active than Pd alone, due to the break-up of multiatom Pd surface sites that bind hydrogen, as well as the decrease in sulfur poisoning imparted by Au to the particle.[40] In addition to diluting multiatom ensembles on the surface of a particle, a second metal can also cause an alteration in ordering of an active metal on the surface. For example, a CuPt alloy particle sample was dealloyed to form a core-shell morphology in the structure, and it was found that the activity of the particles was enhanced for the oxygen reduction reaction.[41] The alteration in activity here was attributed to a modification of Pd-Pd bond

distances in the surface layer caused by the initial presence of Cu in the particle.[41]

Whether it is present at the surface or not, another way by which a second metal can affect the ordering and electronics of a first is through lattice strain effects. Either compressive or tensile strain can arise in bimetallic particles, depending on the nature of and the ordering of the two metals. When a metal shell is grown on a core particle of different elemental composition, for example, the lattice of the shell will often deposit on the core surface pseudomorphically, which induces expansion of the shell lattice relative to the pure metal if the substrate material possesses a larger lattice parameter, or contraction of the lattice if deposited on a metal of smaller lattice parameter.[42, 43] For compositions where two metals are soluble in one another, alloys form with crystal structures generally in keeping with Vegard's law, an empirical relationship that describes the lattice parameter of bimetallic materials as roughly an average of the two lattice parameters of the constituent metals weighted by their composition.[44]

The catalytic properties of the AuPd bimetallic system have been studied often because such catalysts are useful in many reactions, from vinyl acetate monomer synthesis[33], to CO formic acid methanol oxidation reactions, related to fuel cell development[25, 71, 72], dehydrosulfurization, dehydrogenation, hydrogenation, hydrogen peroxide formation[48, 73-76], and selective alcohol oxidation, among others. It is often found that the combination of the two in catalyst form enhances either the rate or selectivity of a reaction. For example, AuPd on TiO_2 selectively oxidizes benzyl alcohol to benzaldehyde at a rate thirteen times higher than that over Pd on TiO_2.[45] AuPd nanoparticles on TiO_2 are twice as productive as TiO_2-supported palladium alone in the direct synthesis of hydrogen peroxide from $H_2(g)$ and $O_2(g)$,[46] and graphene-supported hollow AuPd particles catalyze formic acid electrooxidation at current densities two

times higher than solid Pd nanoparticles.[11] AuPd catalysts provide similar enhancements in several other industrially-relevant reactions.[47] Even though Au is inert as a catalyst in these cases, it can interact with Pd surface atoms to alter the way in which this active metal catalyzes the reaction.

In the context of using model bimetallic catalysts to understanding structure-function relationships of heterogeneous catalysts, the AuPd system is a close to ideal one to study because in addition to being useful in a wide range of reactions, it is also a relatively simple system to study.[48] Au and Pd are soluble at all compositions, so that effects of different phases need not be considered.[31, 49] In many reactions, Au is catalytically inert, so any catalytic activity can be ascribed to Pd. To date, a variety of mechanisms have been proposed for the greater catalytic activity and selectivity of AuPd compared to Pd alone.[48-51] Enache and co-workers found that AuPd/TiO_2 is twice as productive as Pd for benzyl alcohol conversion to benzaldehyde, and proposed that Au is an electronic promoter of Pd.[50] Vinyl acetate monomer production is enhanced 13-fold over 1:4 AuPd/SiO_2 nanoparticles relative to Pd/SiO_2, and this has been attributed to changes in the electronic and geometric properties of Pd upon alloying with Au.[22] Studies of vinyl acetate formation rates over submonolayers of Pd on single-crystal gold surfaces suggest isolated pairs of Pd on Au(100) enhance binding of acetate with ethylene, and suppress the formation of reaction by-products.[22] An AuPd/SiO_2 catalyst with 0.2 monolayer coverage of Pd hydrogenated propene with twelve times the activity of Pd alone; the authors proposed Au breaks up three-fold surface sites of Pd, and thereby increases the formation of highly reactive propylene relative to less reactive propylidene.[51] Similar enhancements of AuPd relative to Pd are observed in many other reactions.[9, 45, 53-58] These examples suggest that the specific way in which Au enhances Pd

activity varies depending on the reaction being catalyzed, and that a clearer, more general depiction of the mechanisms by which AuPd exhibits relatively greater activity, selectivity, and stability will begin to emerge only after examining its properties in a wide variety of reactions.

1.4 Observables changes in catalytic behavior

It is extremely important to note that the behavior of catalysts is only relevant when one considers the environment in which a catalyst is being studied, or more specifically the reaction and its conditions in which a catalyst is employed. For what we learn about bimetallic catalyst behavior to be useful, then, we need to express it in a way that is applicable to a large array of reactions. In the literature, the standard has become to express the interaction between Au and Pd (as well as other metals) as a combination of electronic, geometric, and lattice effects that ultimately alter the catalytic process in a favorable way.[17, 80-83] However, it is impossible to actually segregate electronic and geometric effects from one another, because of the intimate tie between the structure of atoms in and below a surface and its resultant work function.[52]

For this reason, it is proposed that it is most useful to study the effect of the introduction of a second metal into a catalyst - here, Au in Pd - in the context of observable changes in the structural or chemical properties in realistic reaction conditions. Such practicable effects have often been observed in the literature, whether it be in the formation of hydrogen subsurface reservoirs, resistance to CO poisoning, oxidation, or sulfur poisoning, or physical properties like the formation of isolated spillover sites on the surface.[53] For example, Tierney *et al* found that by incorporating a 0.01 monolayer (ML) of Pd into a Cu(111) surface, they could increase the production of

adsorbed hydrogen present on the entire surface.[53] The small percentage of Pd atoms present on the surface, which are extremely active for hydrogen dissociation, were enough to induce the break up of H_2 and to facilitate its diffusion onto the Cu surface, where it could be an active participant in Cu-catalyzed reaction for which the limiting step is the dissociative adsorption of H_2.[53, 54] It is the basis of the work reported here that, while it is important to understand the underlying electronic and atomic-level factors that govern these more directly observable characteristics, it is more useful to begin forming a basis set of catalyst structure function relationships that can be directly employed knowing the chemical characteristics needed to achieve a successful reaction. One observable that will be focused on in the following work presented is the prevention of particle growth under high temperature treatment conditions, conferred by an inhibition in the oxidation of Pd in the presence of Au. Physical prevention of particle oxidation and aggregation, as in the passivation of a Cu particle surface with carbon during synthesis, has been observed before, but there are little to no reports of size control conferred by the incorporation of a second metal into a first.[55] The second observed chemical outcome of incorporating Au into a Pd particle is the ability of the particles to form hydrogen reservoirs within their bulk, something that is useful not only in catalytic applications but also in hydrogen storage for fuel cell applications. In both cases, this is the first time a systematic study has been undertaken to investigate the effects of the surface and overall particle structure and composition on the propensity of AuPd bimetallic catalysts to have these effects.

1.5 Characterization Methods

Characterization of model nanoparticle catalysts is central to assessing their performance in a meaningful way. For bimetallic nanoparticle catalysts in particular, it

is paramount to have the best understanding possible not just of the global structure of the catalyst material, but also of the relative positioning of the two metals on an atomic scale. Knowing as much as possible about the nature of the active sites formed by the arrangement of the two metals within the particles makes it possible to quantify the catalyst activity and to describe the behavior in terms of the interactions a second metal has with the catalytically active metal. In this section, particle visualization and surface site analysis techniques will be discussed, focusing on the useful information that can be derived from each that can contribute to a full understanding of the bimetallic AuPd catalysts.

1.5.1 Visualizing nanoparticles - transmission electron microscopy

TEM is a technique that takes advantage of the inelastic scattering of a coherent electron beam at high energies to create a two-dimensional rendering of specimen nearing the atomic scale. Unlike typical microscopes, the TEM can also generate secondary signals characteristic to the sample at hand, such as x-rays, that can be detected and interpreted to give information about the sample.[56] It also can achieve resolution levels that are not possible with a conventional microscope, which allow one to image nanoscale materials.[56] The contrast that is seen in a TEM image is a result of differences in atomic ordering, thickness, and the elemental composition of the specimen analyzed. Scattering and other high-energy processes that occur when the electron beam impinges on the sample, therefore, can be manipulated to visualize the distribution of elements within a single particle, as well as the ordering of atoms within a particle.

In short, the TEM works as follows: electrons are generated from a source and accelerated, using a potential drop, to have a certain energy. The higher the energy of

the beam, the higher the resolution that may be achieved until aberrations associated with the electromagnetic lenses used to focus and align the beam limit the resolution, but can be corrected to achieve atomic resolution.[56] Relatively higher energies may be used when analyzing heavy metal containing specimens, and this is an advantage in the characterization of the analysis of bimetallic nanoparticles.

The incident electron beam interacts with the sample it impinges upon in several ways: it may cause the atoms present to emit characteristic x-rays, create electron-hole pairs, or eject electrons from the specimen, and in turn, the beam may be either inelastically or elastically scattered by the specimen. The degree of forwarding scattering of the beam depends on the crystallinity of the sample, and also on the elemental identity of the atoms comprising the sample. By nature, nanoparticles are thin enough that not all of the beam will interact with the sample, and a portion of it will pass through unadulterated to the detection screen. The variation in contrast caused by any number of these interactions results in an image that is a two-dimensional projection of a three-dimensional space.

1.5.1.1 Conventional TEM (Bright field) and Z-contrast (Dark field) TEM

When TEM images are taken by detecting electrons that have not been scattered or only deviate slightly from the direction of the incident electron beam, the result is a conventional bright-field TEM image, in which objects on the specimen appear darker than the background (generally, the sample is supported on a film made of a light element, like carbon, which scatters relatively very little of the electron beam). The contrast of this image is the cumulative result of contributing factors, one being amplitude contrast, in which the variation in the contrast recorded in an image derives

from variation in the mass or the thickness of the specimen. Another lesser contributor is phase contrast, deriving from a change in the phase of different electrons that pass through a very thin specimen. This second type of contrast can be harnessed to capture high-resolution images of specimens. Conventional TEM images, which rely on the first, are useful for determining the size distribution of nanoparticles on a catalyst as well for visualizing the degree of distribution of the particles on the support material.

The electrons that do not travel through the sample to form the direct beam, but which are scattered from the beam, are deflected as a result of interaction with the nuclei and electron clouds of atoms comprising the sample.[56] Electrons are scattered coherently (Bragg scattering) from planes of atoms in a crystalline sample at small scattering semi-angles (caused by interaction with the electron cloud, < 3°) to form diffraction patterns. They are scattered incoherently to higher scattering angles due to interaction with nuclei; the propensity for this high angle scattering to occur, quantified as the scattering cross section, can be described by the Rutherford equation, given below:

Equation 1: Rutherford cross section describing high-angle elastic scattering.[56]

$$\sigma_R(\theta) = \frac{e^4 Z^2}{16(4\pi\varepsilon_0 E_0)^2} \frac{d\Omega}{\sin^4 \frac{\theta}{2}}$$

An important implication of this equation for the purposes of imaging is the dependency of the cross section on the square of the atomic number, Z, of the scattering nucleus. Because high angle scattering is so dependent on the Z-number of the atoms interacting with the beam, detection of the electrons scattered to high radial angles generates an image in which the variation in intensity is element-dependent. So-called z-contrast images can be captured by high-angle annular dark field scanning

transmission electron microscopy (HAADF-STEM); Figure 3 shows a schematic of the detector set up for this process relative to typical bright field images.

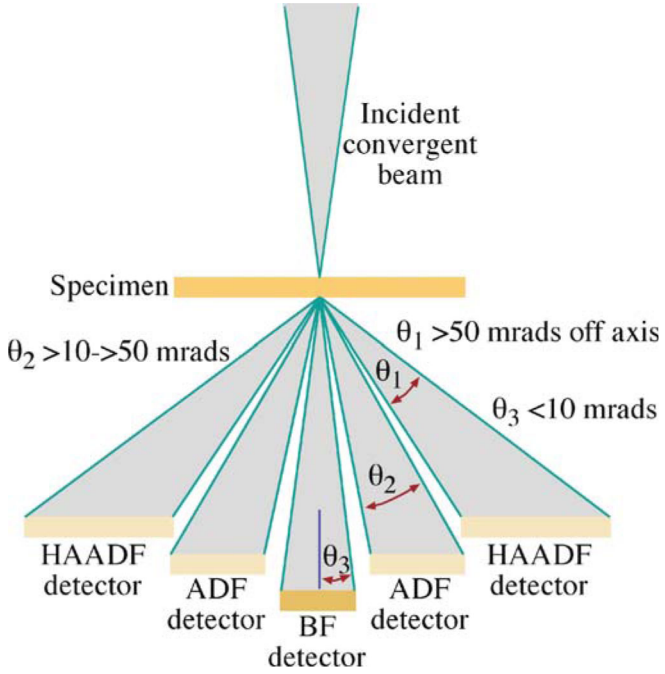

Figure 3: Relative positions of high angle (HAADF) and typical bright field (BF) detectors for imaging z-contrast and conventional images, respectively.[56]

In the context of analyzing bimetallic nanoparticles, z-contrast dark field imaging is very useful in visualizing the relative positions of two metals, because the high Z-number of platinum group and transition metals translate to large cross-sections and a high degree of inelastic scattering, the intensity of which can be directly correlated with relative positions of the metals on the periodic table.

1.5.1.2 High resolution TEM imaging

High resolution TEM (HRTEM) is useful in nanoparticle characterization because it allows us to literally see the atoms comprising the particles. In conventional TEM,

spatial resolution is limited because electrons that are scattered coherently at higher angles pass through the objective lens of the microscope at its edges, and are not quite focused back to the same position as electrons that pass through the objective lens at smaller angles of deviation from the direct beam.[56] This so-called "spherical aberration" causes the resultant spread in points recorded in the image, and therefore, spherical aberration correctors, an accessory that is non-trivial to incorporate into microscopes, are paramount to achieving high quality high resolution TEM images.[42]

Because electrons scattered to high angles are scattered incoherently, the risk that such electrons would scatter more than one time while passing through a specimen and interfere with other electrons moving through the same path is minimized greatly.[42] HRTEM are often acquired as dark field images because the high resolution relies primarily on phase contrast produced as the beam travels through the specimen, and can be drastically altered by multiple scattering events.[56] Such so-called dynamical interference introduces unnecessary complexity into the interpretation the image acquired.[56]

Acquiring HRTEM in dark field intrinsically couples the technique with z-contrast imaging, which is especially useful in characterizing bimetallic nanoparticles, because one can directly see how the different metals being analyzed situate themselves in a particle. Theoretically, one can measure the spacing between planes of atoms and gather information on the degree of elemental intermixing in alloy particles, uncover whether a shell deposits pseudomorphically upon the core surface it is grown upon, or look for indications of any surface reconstruction that may have occurred.[42, 57] In our case, HRTEM gives an idea of the thickness of the Pd shell surrounding a Au core in terms of the number of monolayers of Pd present.[4] The HRTEM image in Figure 4 demonstrates

the utility of being able to capture the atomic spacing in this case of three-layer Pd-Au-Pd bimetallic nanoparticles. Measurement of the interplanar spacings in this case revealed that the lattice parameter matches with the value expected for the particle composition and that the particles are single crystalline, displaying a seamless transition between areas of different relative composition.[42]

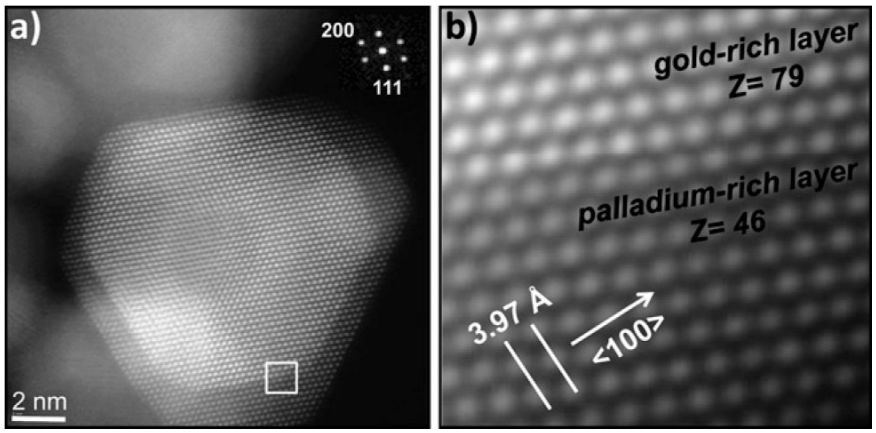

Figure 4: An ultra-high resolution HAADF-STEM image of three layer Pd@Au@Pd nanoparticles.[42]

1.5.1.3 Energy-dispersive x-ray spectroscopy coupled with scanning TEM (EDX-STEM)

Perhaps one of the most visually straightforward and therefore useful techniques for characterizing the elemental distribution of metals in bimetallic nanoparticles is EDX-STEM. This technique takes advantage of the fact that x-rays are emitted when the electron beam impinges upon a sample. These x-rays are characteristic of the core electron levels in the particular elements that are present in the sample, and with a special detector, one can probe the overall elemental breakdown of the sample in the area of focus, or, with a scanning detector, can generate an elemental map of particles

comprising a sample.[9, 87, 88] The latter is tantamount to collecting an EDX spectrum at every pixel the detector scans over.[56]

It should be noted that there are dangers in taking the results of HRTEM or EDX-STEM imaging and interpreting them on their own, in that these techniques characterize only a single nanoparticle at a time among a sea of particles that numbers upwards of 10^{14} that might have been made by the same synthetic pathway. To that end, conventional imaging is important in confirming the uniformity of the nanoparticles in a catalyst sample, so that higher-magnification, single particle-based analytical electron microscope methods can be confirmed to give an accurate representation of the particle morphology.

1.5.2 Nanoparticle active surface area characterization techniques

One of the main parameters used to judge a catalyst's performance is its turnover frequency (TOF), or its activity quantified as the rate of conversion of molecules of reactant per unit time per active surface site. Without an accurate count of surface sites, the best approximation that can be given is the rate of conversion as a function of the mass of metal incorporated into a catalyst, or the mass of the catalyst used in the reaction[45]. The problem with this approach is that it introduces uncertainty to the quantification of activity that only serves to obscure the process of correlating the particle structure with its performance.

1.5.2.1 CO chemisorption for quantitation of active surface site density on a catalyst

CO chemisorption analysis is the most common tool for obtaining a quantitative measure of the number of active surface sites on a supported nanoparticle catalyst. The working assumption of the technique is that any active site on the surface that chemisorbs a CO molecule is available as a surface site upon which other reactants may

adsorb and be transformed into a product. Typically, a known quantity of the catalyst is exposed to a known volume of CO(g), and the quantity of CO(g) that is evacuated from the chamber after exposure is measured. The difference in the initial and final volumes of CO(g) is indicative of the number of active surface sites on the sample. The volume of CO adsorbed on the surface is related to the number of active surface sites by :

Equation 2: Relationship between volume of chemisorbed CO and number of active surface sites per gram of catalyst.

$$\frac{V_{CO}\rho_{CO}N_A m}{M_{co}} = n_{surface}$$

where V_{CO} is the volume of CO adsorbed per gram of catalyst, ρ_{CO} is the density of CO at the analysis temperature (generally room temperature), M is the molecular weight of CO, N is Avogadro's number, $n_{surface}$ is the number of active surface sites per gram of catalyst, and m describes the average number of surface atoms coordinated to one CO molecule. The inclusion of factor m to describe the ratio of atoms per adsorbed CO molecules throws light on the fact that there are often several types of active sites on nanoparticle surfaces. Altering the distribution of surface sites available can be a key mechanism by which the inclusion of a second metal changes both the selectivity and activity of a surface, and so it is important to gauge the identities of the types of surface sites on a catalyst particle. This can be accomplished again by utilizing CO(g) and its propensity to form metal-carbonyl binding species when it interacts with metal surfaces.

1.5.2.2 Diffuse reflectance infrared Fourier transform spectroscopy (DRIFTS) to qualitatively describe surface site geometry and identity

Carbon monoxide binds with metals through the interaction of its 5σ and $2\pi^*$ orbitals with d-band electrons in transition metals, and can bind with more than one metal

surface atom, depending on the nature of the surface. The strength as well as the multiplicity of the bond can vary depending on the degree of surface coverage by the adsorbing species, but also depending on the composition of a surface containing more than one type of metal.[58] Because of the role of the d-state metal surface electrons in the binding of CO to the surface of the particles, the vibrational spectrum of the stretching frequencies of adsorbed CO molecules can be used to directly interpret the geometry of the surface active sites on the catalyst being probed.[59]

Diffuse reflectance infrared Fourier transform (DRIFT) spectroscopy is a technique in which CO is pulsed over the powder catalyst to be analyzed, and an infrared light source containing a range of wavelengths between 4000 cm^{-1} and 400 cm^{-1} is allowed to impinge upon it. The light is diffusely reflected from the rough surface of the catalyst powder, after interacting with the CO absorbed onto the surface of the catalyst. A given CO molecule adsorbed onto the surface will possess a resonant frequency that is modulated depending on the type of active surface site it is bound to, and so the wavelength of IR light absorbed by it is directly correlated to the character of the surface site. The data collected is Fourier transformed to extract the absorption of the IR radiation as a function of wavenumber, rendering the data into a form that can be used to characterize nanoparticle surfaces.[60]

1.5.3 Bulk measurements of the particle structure - XAFS, UV-Vis spectroscopy, temperature-programmed desorption

Examination of bimetallic catalysts by techniques that do not necessarily distinguish between the finer details in the structure of the particle surfaces are useful because they confer an understanding of the global effect of those detailed structural components.

They can also act as a gauge of the homogeneity of the catalyst structure. In this work, x-ray absorption spectroscopy, UV-visible spectroscopy and temperature programmed desorption were utilized to gather an understanding of the average particle structures, to confirm the discrete difference in the three core-shell catalysts, and to probe the overall propensity of the particles to oxidize and hold hydrogen, respectively.

1.5.3.1 X-ray absorption fine structure spectroscopy

X-ray absorption fine structure spectroscopy (XAFS) is a technique that takes advantage of the ability of high energy x-rays, when tuned to the appropriate wavelength, to be absorbed via the photo-electric effect and to eject the core electrons of a metal atom.[61] XAFS yields information about the number and types of atoms present in the first coordination shell surrounding the atoms of the element being analyzed, called the absorber atom, the bond distances between the absorber and these surrounding atoms, and the static disorder, or degree of uniformity of the interactions between the absorber and surrounding atoms, termed the Debye-Waller factor of the interaction.[44] Since the absorption coefficient is related to the atomic number Z of an element to the fourth power (see Equation 3), XAS is ideal for analyzing the heavier metallic elements that comprise catalytically active metal nanoparticles.[61] In this equation, ρ is the sample density, A is the atomic mass of the sample, and E is the energy of an x-ray impinging upon the sample.

Equation 3: the relation of the absorption coefficient μ of a metal of an x-ray as a function of atomic number and x-ray energy.[61]

$$\mu = \frac{\rho Z^4}{AE^3}$$

As the energy of the x-ray incident on an element are scanned in the region of a core electron binding energy, μ increases slowly, until E matches the binding energy of one of its core electrons, at which the absorption coefficient jumps significantly, forming an absorption edge on the spectrum. At the absorption edge energy, E_0, for a given core electron, the electron is removed to the continuum, where it propagates as an electron wave from the absorbing atom. As the electron wave moves radially outwards from the absorbing atom, it encounters the atoms that surround the absorber and interacts with these. The surrounding atoms are referred to as backscatterers, interacting with the electron wave and propagating a backscattered wave that constructively or destructively interferes with the initial electron, depending on the distance of and identity of the backscatterer from the absorber. A schematic of this process is shown in Figure 5.[62]

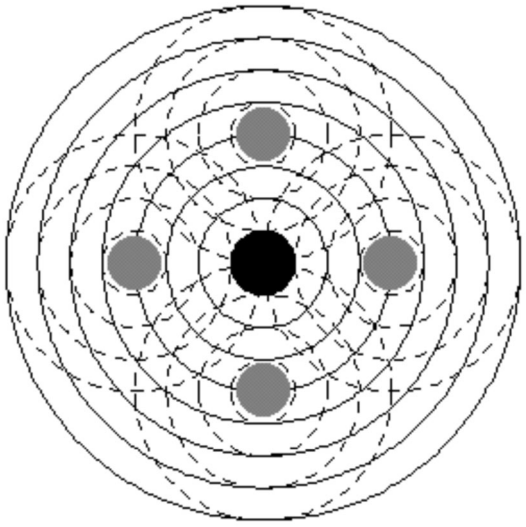

Figure 5: Schematic of the emission of a core electron wave from an absorber atom and subsequent interaction with scatters to produce modulated absorption of the incident X-ray.[62]

As the x-ray wavelengths scanned through during the acquisition of an XAFS spectrum continue past E_0 to higher energies, the excess energy $E - E_0$ absorbed by the emitted electron manifests as kinetic energy, which changes the interference pattern that

is produced when the electron wave interacts with the surrounding backscatterers. The result is an oscillation in the absorption coefficient with increasing E above E_0 known as the fine structure in the X-ray absorption spectrum. An example of a typical EXAFS spectrum is shown in Figure 6A. For Au, XAFS spectra are typically collected at the energy of the LIII core electron, and for Pd, spectra are collected at the edge corresponding K electron ejection.

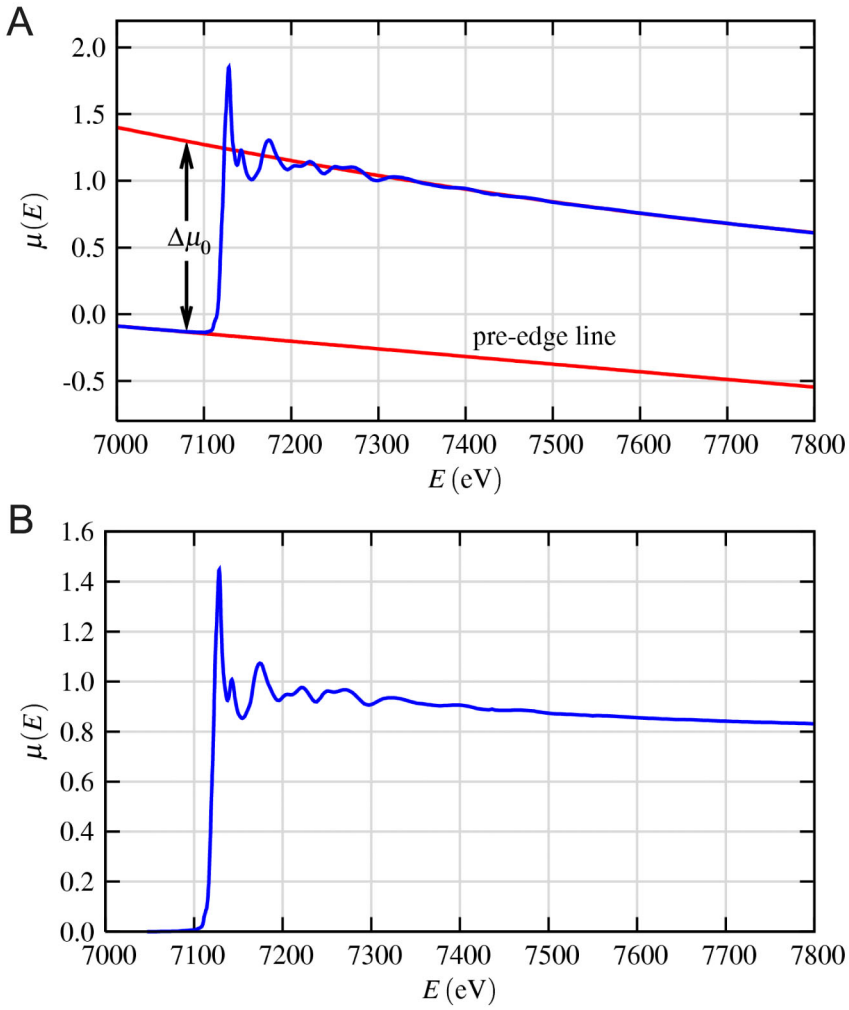

Figure 6: Example XAFS spectrum A) before background subtraction and B) after subtraction of the background, or normalization, of the data.[61]

To isolate the fine structure features for analysis, analytical software is used to model the background of the spectrum collected, yielding normalized data like that shown in Figure 6B. The energy-based spectrum is then converted using Equation 4 to k, the photoelectron wave vector, at which point the data, now in k-space, can be Fourier transformed to give the distribution of contributions to the XAFS signal as a function of distance from the absorbing atom. Typically, the k-space spectrum is weighted by either k^2 or k^3 to amplify oscillations at higher k, which contains the information describing interactions between heavy metals, before being transformed to R-space.[61] In addition to amplifying the signals from the high Z-atom backscatterers of interest, k weighting also dampens the contributions (at low chi-values) to the data arising from static and thermal oscillations.

Equation 4: Conversion of photo-electron energy into wave vector *k*.[61]

$$k = \sqrt{\frac{2m(E - E_0)}{\hbar^2}}$$

An example of XAFS data that has been transformed into k-space and R-space is shown in Figure 7. The R-space spectrum is typically shown as the magnitude of the Fourier transform, which is the sum of the real and imaginary parts of the transform.[61]

To extract information from the XAFS data, the experimental data is fit using the XAFS equation, given in Equation 5. This equation describes the k-space chi function of the sample as a sum of *j* oscillatory contributions arising from interactions with backscatterers of different identities and at different distances from the scattering centers.

Equation 5: the XAFS equation.[61]

$$\mathrm{X}(k) = \Sigma_j \frac{N_j f_j(k) e^{-2k^2\sigma_j^2}}{kR_j^2} \sin\left[2kR_j + \delta_j(k)\right]$$

In this equation, the scattering amplitude $f_j(k)$ and the phase shift of the photoelectron $\delta_j(k)$ are dependent upon Z of the backscatterer j, and can be calculated through a theoretical calculation that employs structures with known coordination environments and absorber-backscatterer distances.[61] Once these values have been determined, they can be set, allowing the calculation of the distance to neighboring atoms j, R_j; the coordination number of neighbors N_j; and the mean-square displacement, or Debye-Waller factor of neighbors j, σ^2. In the case of XAFS spectra collected at the Pd K edge for AuPd nanoparticles, for example, the scattering amplitude was calculated by fitting the known Pd crystal structure to the XAFS equation. The experimental data was then fit by setting this parameter and using a theoretical bimetallic Au:Pd 1:1 alloy structure as a starting point for determining the number of scattering paths and deviations from the theoretical model in terms of disorder and changes in bond distances required to fit the experimental data.

It is important to remember that the fit results of XAFS data represent an average of the coordination shells surrounding all of the absorbers of a particular type, and for this reason, the parameters extracted from XAFS fitting give an idea of the uniformity of the nanoparticle structures throughout the entire catalyst sample, particularly in the form of the Debye-Waller factor value. In this work, the coordination numbers N and bond distances R act as an indicator of the segregation of Au and Pd within the nanoparticles, which is useful in determining the nature of the Au-Pd interface in core-shell nanoparticles and the extent of intermixing in alloy samples.

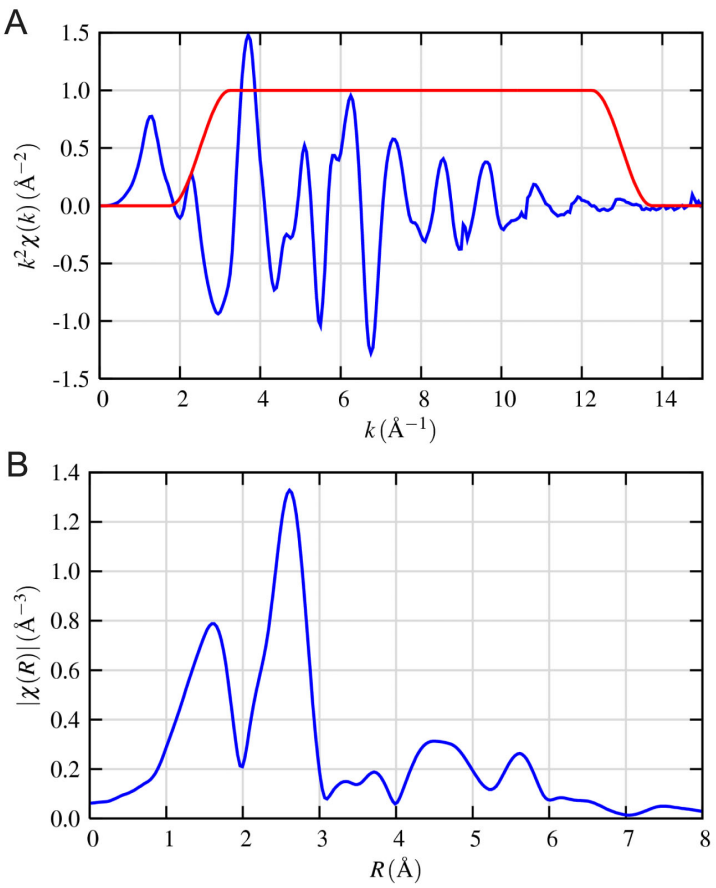

Figure 7: Example XAFS data in A) k-space and B) R-space. In A), the k-space spectrum has been weighted by k^2.[61]

1.5.3.2 Temperature programmed reduction and temperature programmed desorption

Temperature-programmed reduction is a relatively straightforward technique in which a sample is heated at a controlled linear rate with respect to time in a hydrogen-containing atmosphere, and the desorption or uptake of hydrogen is monitored by mass spectrometry as a function of both parameters. Theoretically, the technique can be used to monitor the desorption of a wide range of adsorbates present on the surface of a catalyst particle, giving an idea of its adsorption energy; in this case the technique is termed temperature programmed desorption (TPD).[5] For example, the desorption of

ammonia from the surface of alumina-supported Au-Pd particles was used to determine the strength and number of acidic sites on the catalyst, and to determine how their presence affected the sulfurization tolerance of the catalysts.[63]

By limiting analysis to the uptake and desorption of hydrogen, one can investigate the oxidation state of the metals comprising the catalyst, as well as the ability of the catalyst to hold hydrogen upon or within its structure. Depending upon the extent of surface oxidation of the catalysts before beginning a TPR experiment, the degree of hydrogen taken up to re-reduce the metal in the particles can vary drastically. Generally, uptake is signified by positive peaks on TPR spectra, while desorption of hydrogen from the particle is denoted by an inverted peak on the spectrum. When a second TPR is carried out on a sample, it is typically referred to as temperature-programmed hydrogen desorption (TPHD).

1.5.3.3 Surface plasmon resonance monitoring by UV-Visible spectroscopy

Noble metal nanoparticles are well-known to absorb light in the visible wavelength region of the electromagnetic spectrum through the stimulation of localized surface plasmon resonance of electrons at the particle surface, and this phenomenon has been exploited in many optical and sensing applications of such particles.[94-96] Because the absorption of light and occurs at the surface of particles, it can be altered dramatically when that surface is covered or otherwise manipulated. Since Au possesses a surface plasmon around 520 nm, but Pd does not exhibit one in the visible range of the spectrum, the disappearance of the Au SPR peak may be monitored by UV-visible spectroscopy to ensure the deposition of Pd to form core-shell particles rather than the formation of separate Pd species during synthesis. In short, UV-Vis provides a simple

way to develop a synthetic method for making bimetallic particles by multistep procedures. In our work UV-Vis analysis was also valuable in establishing the existence of discrete differences between particles intended to have differing shell thicknesses before extensive microscopy-based characterization was employed.

As a side note, there are many other surface analytical techniques that exist that were not employed here, but which could provide valuable information regarding the structure of bimetallic catalysts. These include techniques like Auger electron spectroscopy and electron energy loss spectroscopy (EELS), which are more appropriate for elements of lower atomic number, as well as atomic force microscopy (AFM) and x-ray photoemission spectroscopy, which can both yield valuable information regarding the surface structure, though in the case of AFM, perhaps not on particles in the size range studied here (~5 nm in diameter).[5] The characterization techniques used in the work presented here, however, serve to present a detailed illustration of the physical and chemical properties of the AuPd nanoparticle catalysts studied.

1.6 Au_{core}-Pd_{shell} nanoparticle and alloy AuPd nanoparticles as uniform bimetallic catalysts for studying the influence of bimetallic arrangement on catalyst performance

To begin to investigate how Au and Pd interact with one another to produce observable alterations in catalyst behavior, a series of three polyvinylpyrrolidone (PVP)-stabilized Au-Pd core-shell nanoparticles was synthesized via a two-step solution phase reduction method.[4] By altering the amounts of Pd precursor, reducing agent, and reaction quenching agent, as well as varying the rate of introduction of Pd ion to the reaction solution, 4.3 nm Au core particles were coated with Pd shells determined to be 0.7 ± 0.2, 1.9 ± 0.3, and 3.8 ± 0.8 atomic monolayers thick from HAADF-STEM analysis.

Here, 0.7 symbolizes an incomplete monolayer of Pd on the inner core of Au; in fact, as will be discussed in Chapter 4, XAFS reveals that because it is an incomplete layer when deposited on the Au core, the surface Pd on the 0.7 Pd@Au particles reconstructs into the Au-Pd interface.

Representative HAADF-STEM images of each core-shell particle (denoted by Pd@Au from this point forward) are shown in Figure 8A-C. In these images, z-contrast makes it possible to see the more intense Au that forms each particle core as well as the lower intensity Pd atoms that surround the seed particle. The observed Pd shell thickness corresponds closely with the number of monolayers expected, as calculated from the amount of $Na_2PdCl_4(aq)$ introduced into each Au seed solution, deviating only in the case of the 3.8 Pd@Au particles; Table 1 details this comparison. The UV-visible spectra (Figure 8D) of the Au seeds and each type of Pd@Au particle, acquired while still in solution, show the 520 nm plasmon resonance peak of Au blue shifts and ultimately disappears as the Pd shell on the core increases in thickness.

TEM size distributions of the Au NPs and the AuPd NPs are shown in Figure 9. Analysis of conventional TEM images shows the Au seeds are 4.3 ± 0.6 nm in diameter. The calculated average diameters of the 0.7, 1.9 and 3.8 Pd@Au particles are 4.6 ± 0.6 nm, 4.9 ± 0.6 nm, and 5.2 ± 0.8 nm, respectively. The relative standard deviation, representing the polydispersity of the particles, is $13.2 \pm 1.3\%$ for all of the particles. The average size of the Au seed was subtracted from the average sizes of the Pd@Au particles to give the average shell thicknesses shown in Figure 9.

After depositing the nanoparticles onto the silica support, the compositions of the catalysts were analyzed by ICP-AES. This data was used to calculate the shell thickness using the density of bulk Pd ($12.02\ g/cm^3$), and the Au seed diameter as

determined from bright-field TEM. Table 1 compares these shell thicknesses derived from ICP-AES with those measured by bright-field TEM and HAADF-STEM, while Table S2 presents the same data in terms of nanoparticle composition. The values determined by ICP-AES match reasonably well with the shell thicknesses (and thus compositions) calculated from the bright-field TEM images. We hypothesize that the difference between the HAADF and the average values from TEM and ICP-AES stems from the fact that the Pd shell becomes more jagged and uneven as it grows in thickness, leading to a shell that appears thicker in HAADF-STEM imaging mode than can be accounted for by comparing the ratio of Pd to Au in the sample. This hypothesis is supported by observations that the intensity of the Pd shell around the 3.8 Pd@Au in Figure 1C is not uniform and that the outer edge of the particle appears to be irregular. Although they contain some error due to the hypothesized jagged nature of the shell, the HAADF-STEM measurements of shell thickness on individual nanoparticles give a sense of the variance in the composition between the nanoparticles. In comparison, the bright-field TEM and ICP-AES measurements can only give a sense of the average composition, with the variance principally coming from the variance in the diameters of the Au seeds.

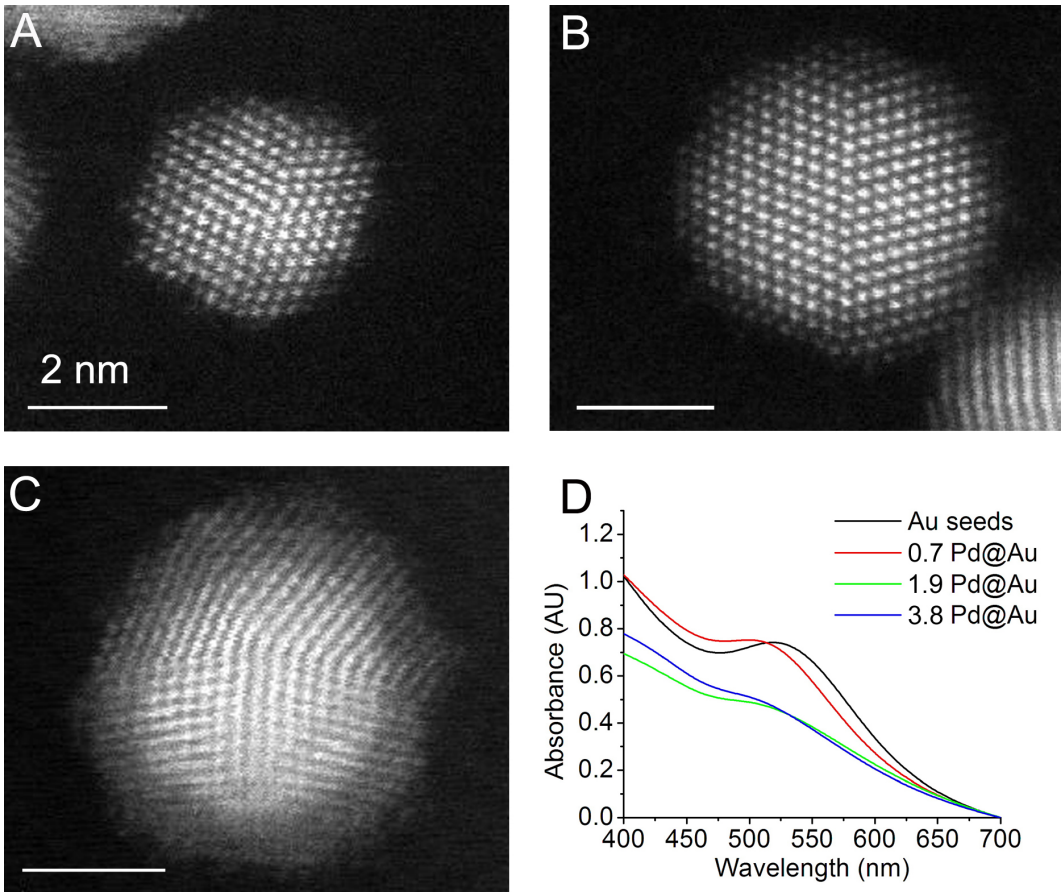

Figure 8: HAADF-STEM images of A) 0.7 Pd@Au, B) 1.9 Pd@Au, and C) 3.8 Pd@Au nanoparticles after synthesis. Panel D) shows the UV-Visible spectra of the nanoparticles in aqueous solution.

Table 1: The Pd shell thickness as determined by bright-field TEM, HAADF-STEM, and ICP-AES analysis.

sample	expected shell thickness from Pd added to the rxn (atoms)	shell thickness from TEM (atoms)	shell thickness from HAADF-STEM (atoms)	shell thickness from ICP-AES (atoms)[a]
0.7 Pd@Au	0.5	0.60 ± 0.1	0.7 ± 0.2	0.56 ± 0.1
1.9 Pd@Au	1.5	1.39 ± 0.3	1.9 ± 0.2	1.15 ± 0.2
3.8 Pd@Au	5.0	2.03 ± 0.4	3.8 ± 0.8	1.72 ± 0.3

After depositing the nanoparticles onto the silica support, the compositions of the catalysts were analyzed by ICP-AES. This data was used to calculate the shell thickness using the density of bulk Pd (12.02 g/cm^3), and the Au seed diameter as determined from bright-field TEM. Table 1 compares these shell thicknesses derived from ICP-AES with those measured by bright-field TEM and HAADF-STEM, while Table 2 presents the same data in terms of nanoparticle composition. The values determined by ICP-AES match reasonably well with the shell thicknesses (and thus compositions) calculated from the bright-field TEM images. It was hypothesized that the difference between the HAADF and the average values from TEM and ICP-AES stems from the fact that the Pd shell becomes more jagged and uneven as it grows in thickness, leading to a shell that appears thicker in HAADF-STEM imaging mode than can be accounted for by comparing the ratio of Pd to Au in the sample. This hypothesis is supported by observations that the intensity of the Pd shell around the 3.8 Pd@Au in Figure 8C is not uniform and that the outer edge of the particle appears to be irregular. Although they contain some error due to the hypothesized jagged nature of the shell, the HAADF-STEM measurements of shell thickness on individual nanoparticles give a sense of the variance in the composition between the nanoparticles. In comparison, the bright-field TEM and ICP-AES measurements can only give a sense of the average composition, with the variance principally coming from the variance in the diameters of the Au seeds.

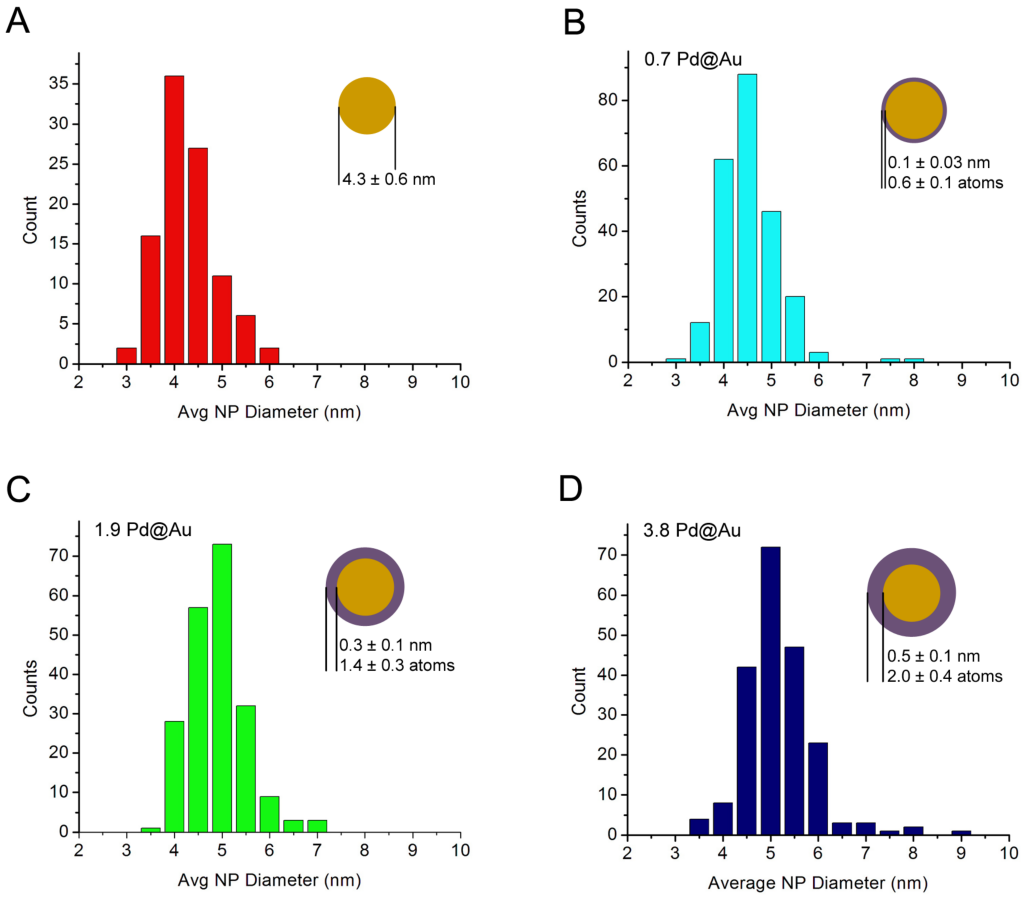

Figure 9: Histograms of the size of Au and AuPd nanoparticles. The relative standard deviation of the particle size is 13.2 ± 1.3%.

Table 2: The composition of Pd in the nanoparticles in terms of weight percent, as calculated from the shell thicknesses listed in Table 1, and using the bulk density of Pd as a conversion factor. [a]The Pd loading per particle was determined using the bulk density of Pd (12.02 g/cm^3) as a conversion factor, and a Pd interlayer spacing of 0.225 nm.

sample	expected %Pd per particle from Pd added to rxn (atoms)	%Pd per particle from TEM (w/w)[a]	%Pd per particle from HAADF-STEM (w/w)[a]	%Pd (w/w) per total metal from ICP-AES
0.7 Pd@Au	9.3	11.1 ± 3.7	12.9 ± 7.0	10.9 ± 2.3
1.9 Pd@Au	25.5	23.9 ± 9.3	31.2 ± 9.3	20.2 ± 4.3
3.8 Pd@Au	61.2	32.9 ± 12.1	52.0 ± 19.6	28.5 ± 6.1

The core-shell nanoparticles were deposited on a silica support, and were found to transform into alloy nanoparticles consisting of 10.9 ± 2.3, 20.2 ± 4.3, and 28.5 ± 6.0% Pd per nanoparticle, respectively, upon being calcined and reduced at 300 °C. Using the core-shell particles as a precursor in the production of alloyed nanoparticles facilitates the determination of the per-particle Pd content by measuring changes in shell thickness *via* standard bright-field TEM and HAADF-STEM. Additionally, it provides two series of AuPd catalysts that match in their Pd composition and differ in morphology in a way that minimizes the introduction of variables that would complicate the comparison of the behavior of the two types of particles. These catalysts are an ideal starting point for uncovering practicable effects that arise from incorporating Au into Pd nanoparticle catalysts.

In addition to characterization by the techniques discussed in the previous section, the particle catalysts were also used in three chemical reactions: the dehydrogenation of α-limonene to *p*-cymene, the hydrogenation of ethylene to ethane, and the dehydrogenation of formic acid to form carbon dioxide and hydrogen gas. Each of these reactions provides a different environment for testing the properties of the catalysts. The conversion of limonene was carried out at 250 °C, a high enough temperature regime to limit tests to the alloy particles, but is a good system for exploring the ability to tune the selectivity of these particles by altering their Pd composition, as limonene can be transformed into several terpinene-based isomers as well as its fully hydrogenated form, *p*-menthane, and *p*-cymene, its aromatic derivative. The structures of limonene, the intermediate isomerization species monitored for: γ-terpinene, α-terpinene, and terpinolene, and *p*-cymene and *p*-menthane are displayed in Figure 10. It is shown that the retention of size during the alloying process, facilitated by role of Au near the

surface of the particle in preventing Pd oxidation during heat treatment, in combination with the presence of a minimum threshold of at least 20% Pd per particle, helps to improve the selectivity of the AuPd catalysts to *p*-cymene conversion over monometallic Pd catalysts.

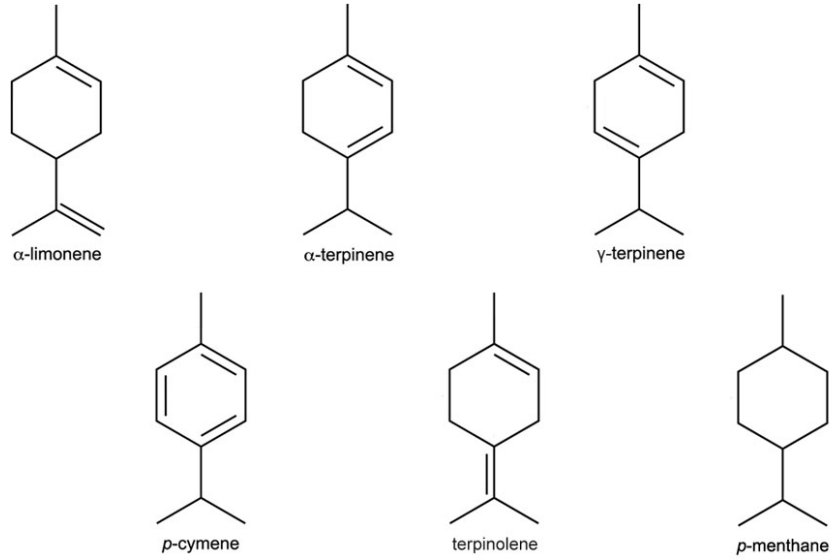

Figure 10: Molecular structures of limonene; terpinene isomers α-terpinene, γ-terpinene, and terpinolene that were monitored for; *p*-cymene, and *p*-menthane.

Because ethylene hydrogenation takes place at lower temperatures, it is not necessary to treat the catalysts at the high temperatures that cause the core-shell particles to transform into their alloy counterparts. As such, this reaction allows a comparison of the Pd@Au and AuPd/SiO_2 catalysts in a vapor phase reaction. Since there is only one hydrogenation product expected from this reaction, this experiment is focused on how the activity of the particles is altered by not only the amount of Au incorporated with Pd into the particles but also by how the two metals are arranged with respect to the surface. Characterization by TPR and XAFS suggests the Pd@Au

catalysts can be tuned to act as a reservoir for subsurface hydrogen, and the conclusions from these investigations are coupled with results from the reaction to determine the extent to which these reserves can affect the rate of the reaction.

2. Experimental Methods

2.1 Synthesis of AuPd bimetallic and monometallic nanoparticle catalysts

2.1.1 Chemical Information

Gold(III) chloride trihydrate (520918), sodium citrate tribasic dihydrate (S4641), sodium tetrachloropalladate(II) (205818), hydroquinone (H9003), polyvinylpyrrolidone MW = 55,000 (856568, PVP55), and polyvinylpyrrolidone MW = 29,000 (234257, PVP29) were purchased from Sigma-Aldrich. Hydrochloric acid (UN1789), and *p*-menthane (320-53122) were purchased from Fisher Scientific. Limonene (10162783), *p*-cymene (A0300974), acetone (BDH1101-4LP), ethanol (UN1170), terpinolene (TCT0817-025ML), α-terpinene (TCM0317-025ML), and γ-terpinene (TCM0318-025ML) were purchased from VWR. Palladium(II) nitrate hydrate (22403000) and palladium tetrammine dinitrate (19843400) were purchased from Strem Chemical, and the silica used for all of the catalysts was Aerosil 300 from Degussa (specific surface area = 300 m^2/g). All chemicals were used without further purification. Ethylene of 99.5% purity and hydrogen used for GC flame ionization detector (FID) operation, 5.0 grade, were purchased from Machine Welding and Supply Company. Hydrogen used in the ethylene reactor was UHP from Airgas National Welders.

2.1.2 Solution-phase synthesis of Pd@Au nanoparticles and monometallic Au and Pd nanoparticle controls

2.1.2.1 Synthesis of 5-nm Au seed particles

Stirring rapidly, 980 uL of 1% (w/w) $HAuCl_4$(aq) solution was added to 100 mL DI H_2O in a round-bottom flask. To this, 740 uL of 1% (w/v) sodium citrate and 3 mL of 0.1 M $NaBH_4$(aq) were added in immediate succession. The $NaBH_4$(aq) solution was

chilled to 0 °C in an ice bath before being used. Upon the addition of $NaBH_4$(aq), the solution immediately turned pink-orange in color, indicating nanoparticle formation. The solution was left to sit for one hour before use, during which time it turned bright red. These nanoparticles were used as a substrate on which to grow shells of Pd, and were also used to make the monometallic Au control catalyst tested by the various methods described throughout this work. Before the particles were deposited onto silica in the manner described below, 4 mL of aqueous 1% PVP55 was added to 100 mL of solution, such that the same amount of PVP was introduced to both the Au and AuPd particle samples.

2.1.2.2 Synthesis of 0.7, 1.9, and 3.8 monolayer (ML) Pd@Au particles

Making shell@core Pd@Au nanoparticles with different shell thicknesses was achieved by varying the amounts of reducing agent and Pd precursor ion introduced to the Au seed particle solution during the shell formation phase of the reaction.[63] For each type of nanoparticle made, the Au seed solution was stirred at 450 rpm at room temperature throughout the course of the shell formation, and the reactions were run for 3 h after the initial addition of Pd. For 0.7 Pd@Au, 2 mL of 1% (w/w) hydroquinone was added to 100 mL of Au seed solution, and 2.5 mL of 2 mM aqueous disodium tetrachloropalladate (Na_2PdCl_4(aq)) was infused into the solution at a rate of 67 μL/min. The 1.9 Pd@Au particles were synthesized in 50 mL batches so that the Na_2PdCl_4 solution could be completely infused at the same rate (67 μL/min) within the three-hour reaction time. In this case, 1 mL of 1% hydroquinone to each 50 mL batch, and 9.65 mL of 2 mM Na_2PdCl_4(aq) was infused directly after at 67 μL/min. To make the 3.8 Pd@Au particles, 4 mL of 1% hydroquinone and 2 mL of 20 mM Na_2PdCl_4(aq) were added in succession, the Pd solution being pipetted in all at once. At the end of the reaction, 2 mL

of 1% (w/v) HCl(aq) was pipetted into 100 mL of the 0.7 and 1.9 Pd@Au solutions and 4 mL of 1% (w/v) HCl(aq) into 100 mL of the 3.8 Pd@Au solution to stop the reaction, followed by 4 mL of 1% (w/v) PVP55 aqueous solution to stabilize the particles.

2.1.2.3 Solution-phase synthesis of PVP-stabilized Pd nanoparticles

PVP-stabilized Pd nanoparticles were synthesized using a method based on a synthesis reported by Han *et al*.[4] A 250 mL round-bottom flask fit with a reflux condenser was filled with 100 mL of DI H_2O, 1.06 g PVP29 was added to it, followed by 3 mL of 2M HCl(aq), and the mixture was heated to a rolling boil (hotplate set to 120 °C). Once the reaction was refluxing, 0.53 mL of 0.47 M Na_2PdCl_4(aq) was added, and 80 mL of EtOH was poured in slowly through the reflux condenser, taking care not to let it bump, so to speak. The reaction refluxed for 3h before being removed from heat and cooled while stirring.

2.2 Catalyst preparation

2.2.1 Catalysts prepared by depositing solution-phase PVP-stabilized nanoparticles

To successfully deposit the PVP-stabilized nanoparticles from solution onto a silica support, it was found that the particle solutions first needed to be reduced in volume to decrease the ratio of the number concentration of particles to the concentration of silica in solution; the more intimate the contact between the particles and silica particles, which were initially 10 nm in diameter, the more completely that the particles were removed from the reaction liquid after separation by centrifugation. Each nanoparticle solution was concentrated four-fold by flowing nitrogen gas over the surface of the stirring solution for several hours. The silica powder itself was plasma

cleaned for an hour prior to being dispersed in solvent and combined with the concentrated, still mixing, nanoparticle solution. The combined silica-nanoparticle solution was centrifuged for 1h at a spin rate of 15,000 rpm to precipitate out the catalyst as a gel. For the AuPd and Au nanoparticle catalysts, 0.27 g of plasma-cleaned silica was dispersed in 20 mL DI H_2O before being combined with the nanoparticle solution, and the precipitated catalyst gel was washed two additional times by replacing the supernatant with 15 mL of fresh DI H_2O, remixing the gel into the solvent, and centrifuging at 15,000 rpm for 20 min. These extra steps were employed to remove any unreacted Pd ion or excess PVP55 from the catalyst before drying. Each 100 mL batch of Pd NPs was mixed with 0.73 g plasma-cleaned silica dispersed in 80 mL acetone. Unlike the Au-based catalysts, this sample was not washed after the initial centrifugation step, because upon doing so, significant aggregation of the Pd nanoparticles was observed. After centrifugation was complete, the catalysts were collected into glass vials and dried under house vacuum at 100 °C for 5 h. For each catalyst prepared from a colloidal nanoparticle solution, the number of nanoparticles per liter of solution per gram of silica was kept at a constant value of 1.01×10^{18} NP/L g.

When used in the conversion of ethylene to ethane, it was necessary to dilute the particle concentration per gram of silica support for the catalysts in order to achieve accurate turnover frequency calculations; this is discussed further in Section 2.4.2. To dilute the catalysts, amount of nanoparticle solution added to a given volume of silica was decreased by the intended dilution factor. The 0.7, 1.9, and 3.8 Pd@Au/SiO2 catalysts were diluted by 15, 250, and 500 times, respectively, and both monometallic catalysts were made at 50-fold dilutions. Centrifugation, washing, drying, and pretreatment steps were carried out in the same manner as for the undiluted samples.

2.2.2 Monometallic silica-supported Pd catalysts prepared by conventional impregnation and ion-exchange techniques

2.2.2.1 Synthesis of a silica-supported nanoparticle catalyst by incipient wetness impregnation

The conversion results obtained for the series of solution-phase synthesized nanoparticle catalysts employed in limonene conversion were also compared to monometallic Pd catalysts prepared by traditional techniques; i.e., in which metal particles are formed in the presence of the support material. One such catalyst containing 1.78% (w/w) Pd on silica was prepared by incipient wetness impregnation, and is denoted Pd/SiO_2 (iw). To make this, an aqueous solution of 0.2 g $Pd(NO_3)_2$ dissolved in 18.96 mL DI H_2O was added dropwise to a beaker containing 4 g silica. The resultant saturated material was dried overnight in air, in an oven set to 40 °C, and was subsequently calcined under oxygen at 300 °C for 2 h. The temperature during the calcination procedure was incremented to 300 °C at a ramp rate of 5 °C/min.

2.2.2.2 Synthesis of a Pd/SiO_2 catalyst by the ion exchange method

Ion exchange catalysts, as discussed before, often result in smaller particles and a narrower size distribution than impregnation catalysts, because they take advantage of the cationic nature of unreduced metals to evenly disperse the metal precursor upon a support containing negatively charged surface moieties.[63] To synthesize a 0.6% by weight Pd/SiO_2 sample by the ion exchange method (denoted Pd/SiO_2 (i.e.)), silica powder was mixed with 50 mL of DI H_2O to form a silica gel. The gel was subsequently impregnated with palladium through the dropwise addition of a solution comprised of

1.6 g $Pd[(NH_3)_4](NO_3)_2$ in 40 mL DI H_2O. Afterwards, the solvent was removed by filtration with filter paper and the catalyst was washed three times with DI H_2O before being dried in an oven at 100 °C overnight. The catalyst was then calcined under oxygen with a temperature ramp of 0.5 °C/min from room temperature to 250 °C, where it was held for two hours.

2.2.3 Heat-treatment of PVP-stabilized Pd@Au and monometallic silica-supported nanoparticle catalysts

Heat-treating the PVP-stabilized Pd@Au/SiO_2 catalysts, as well as their PVP-stabilized monometallic counterparts, before utilizing them in higher temperature catalytic reactions, like the conversion of limonene into cymene, was necessary in order to remove as much PVP from the surface of the particle as possible [cite]. Serendipitously, we also observed that this heat treatment caused the core-shell bimetallic particles to alloy, and so the following procedure was also employed to affect alloying for further analysis in lower temperature reactions (i.e., formic acid decomposition and ethylene hydrogenation). First, the dried catalysts were calcined in a tube furnace at 300 °C for 1h under air flowing at 0.6 L/min. The temperature was increased to 300 °C at a rate of 5 °C/min. These calcination conditions have previously been shown to remove PVP from AuPd catalysts.[51] For samples used in limonene conversion and for TEM analysis, the catalyst was reduced at 300 °C for 1h *in situ* under a stream of 100% H_2(g) flowing at 50 sccm. For characterization with DRIFTS, the catalysts were reduced under 30 sccm 10% H_2(g) in He(g) for 1h, and then under 30 sccm 100% He(g) for 30 min.

2.3 Catalyst characterization methods

Inductively coupled plasma atomic emission spectroscopy (ICP-AES) was performed on the three supported bimetallic catalysts to determine the weight percent of the metal loadings on each by Galbraith Laboratories. UV-visible spectroscopic analysis was carried out using a Cary 6000 UV-Vis-NIR spectrometer, scanning the spectrum of the solution-phase Au-containing particles using a double-beam experimental setup. The blank solution used as a reference was prepared as an aqueous solution containing all of the reagents utilized in the Au seed synthesis aside from chloroauric acid.

Bright-field TEM images of each catalyst were acquired with a Tecnai FEI G^2 twin microscope at Duke University, and high-resolution HAADF-STEM images were taken using the JEOL 2010F located at Oak Ridge National Laboratory in Oak Ridge, Tennessee as well as the FEI Titan STEM at North Carolina State University. Specimens of the powder catalyst samples were prepared by dispersing a small amount of the powder in less than 100 uL of methanol and pipetting 4 uL of this on to 400 mesh Cu TEM grids coated with an ultrathin film of holey carbon (08124, Ted Pella).

In order to measure the diameters of the nanoparticles when imaged by conventional TEM, ImageJ64 software was used to measure two perpendicular diameters per particle over at least 100 particles for each sample. The diameters recorded for each particle were averaged before averaging the diameters of all of the particles. The surface areas of each particle measured were calculated in this way and were averaged over the total number of particles analyzed to produce the surface area averages that were used to determine the number of geometry-based active surface sites per gram of catalyst, in turn used to calculate the ethylene hydrogenation TOFs presented in Chapter 4.

Diffuse reflectance infrared Fourier transform (DRIFT) spectra were acquired using a Bruker Optics Vertex 70 FT-IR spectrometer equipped with a Harrick Praying Mantis Diffuse Reflection Accessory with a Praying Mantis High Temperature Reaction Chamber *in situ* reaction cell and OPUS data analysis software. Pulsed CO chemisorption measurements were made using a Micromeritics ASAP 2920 Surface Area and Porosity Analyzer to determine active surface area on the catalyst. For CO chemisorption experiments, the catalysts were reduced at 300 °C or 100 °C in H_2(g) during analysis, based on the sample being analyzed. Cumulative quantities adsorbed were used to calculate the number of active surface sites per gram of catalyst that were in turn used to determine the CO chemisorption-based TOFs reported in Chapter 4. Before chemisorption analysis of calcined and reduced bimetallic catalysts, temperature-programmed reduction (TPR) and temperature-programmed hydrogen desorption (TPHD) analyses were carried out on the same instrument, ramping to either 300 °C or 100 °C in 5% H_2(g)/Ar (flowing at 50 mL/min) at a rate of 10 °C/min. In the TPR profiles shown, a 5% H_2/Ar mixture was used, and a TCD was used to measure H_2 uptake (or evolution). The H_2 and Ar combination was chosen to maximize the TCD detection difference between H_2 and the carrier gas. TPHD refers specifically to decomposition of the bulk palladium hydride phase, as measured in 5% H_2/Ar.

X-ray absorption fine structure spectroscopy (XAFS) experiments were performed on beamline 10-BM-A,B at the Advanced Photon Source at Argonne National Lab in Argonne, IL to determine the extent of alloying and oxide formation on each of Pd@Au/SiO_2 and the PVP-stabilized Au/SiO_2 and Pd/SiO_2 samples in their untreated ("as is") state, after being subjected to calcination conditions, after being calcined and then re-reduced, and after only having been heated to 100 °C in a reducing atmosphere

of 5% H_2 in He. All of the heat treatments took place in the sample holder cell immediately prior to analysis, and all experiments were performed in transmission mode. The samples were analyzed at both the Pd K edge (24350 eV) and the Au LIII edge (11919 eV). The experimental XAFS data collected was normalized, and the resultant chi function was Fourier transformed into R-space using the Athena program included in the FEFF6 XAFS analysis package written by Bruce Ravel. The data were fit in Artemis, also included in this package, using Pd-Au, Au-Pd, and Pd-O references constructed using ATOMS and FEFF 6. Pd-Pd and Au-Au references were determined by measuring Au and Pd foils at the beamline.

2.4 Reaction setups for testing the catalytic properties of the Pd@Au and AuPd model catalysts

2.4.1 Limonene and Menthane Reactor

The limonene and menthane conversion reactions were carried out in a homemade vapor phase glass tube reactor coupled to an HP 5890 Series II gas chromatograph. For each run, 250 mg of calcined catalyst was loaded into the reactor, where it was reduced under 50 sccm H_2(g) at 300 °C for 1h. Immediately after reduction, the reactor temperature was dropped to 250 °C and α-limonene or *p*-menthane was continuously injected by syringe pump (Harvard Instruments) at 6 uL/min. All lines were kept at 220 °C. The GC utilized an FID detector and the oven temperature was maintained at 80 °C, with He(g) as the carrier gas through a Restek Stabiliwax Bonded Packed Column (Cat# 80416-810). Injections were performed every 10 min. Once the reactor temperature and the feed flow stabilized, the reactor was run between 1.5 and 3 hours.

2.4.2 Ethylene Hydrogenation Reactor

Ethylene hydrogenation experiments were performed at room temperature in a quartz tube reactor coupled to an HP 5890 II gas chromatograph. For each reactor run, approximately 100 mg of catalyst was loaded into the reactor tube, and the system was purged with He for several minutes before switching to reaction conditions. Sample dilution was necessary to achieve differential conversion conditions, or conditions under which a catalyst converts only a small fraction of the reactant flowing over the catalyst bed. This ensures that the entire reactor bed mass is exposed to approximately the same amount of reactant, and that all of the catalyst material contributes to the conversion observed, and in turn allows the calculation of meaningful TOF values. Immediately before beginning to collect data, flow of He was increased to 200 mL/min, and H_2 then C_2H_4 were introduced to the reactor in a 6:1 H_2:C_2H_4 molar ratio. The total percentage of reactant gases in the stream was approximately 15% (v/v). The product mixture was sampled every 10 min for at least 3 h to determine the conversion of ethylene to ethane. The GC was equipped with a flame ionization detector, and was calibrated to find the response factors for ethylene and ethane using a Scotty gas calibration standard containing 1% C1 - C5 in N_2. The Pd@Au/SiO_2 , Au/SiO_2, and Pd/SiO_2 catalysts were tested without further treatment aside from being subjected to a flow of He for several minutes before switching to reaction conditions (termed "as is"), as well as after being subjected to the conditions which cause alloying of the AuPd particles; i.e., calcining the particles at 300 °C in air for 1 h in a tube furnace (see Section 2.2.3), and then reducing the sample *in situ* at 300 °C in 10% H_2/He mix flowing at 50 mL/min. A third set of catalysts was heated to 100 °C for 1 h in 10% H_2/He in the reactor tube before being utilized in the conversion of ethylene.

3. Bimetallic Contribution 1: The Prevention of Particle Sintering

Particle sintering is a major obstacle in industrial catalysts in terms of maintaining optimal catalyst performance. In many reactions, the rate of conversion to a product is limited by the amount of active catalyst surface area available to it, and so it is important for the catalyst used to retain the high surface-to-bulk ratio it was presumably synthesized to have - that is, retain its small size - even after being used and regenerated.[21] However, the very processing techniques that are employed to maximize the performance of the catalyst and prolong its utility can cause the particles to sinter into larger aggregates, unavoidably altering the structure and number of surface sites, and thus changing it fundamentally.[64] The regeneration process utilized in industrial settings, for example, is meant to remove hydrocarbon buildup on spent catalysts, but can often cause a loss in the number of active sites by inducing sintering.[102-104] Typically, removal of carbon build-up requires higher temperatures in an oxygen-containing atmosphere to combust the materials away, but this process usually results in regenerated catalysts with lower activity and different selectivity than a fresh catalyst.[64] Thus, from an industrial perspective it is highly desirable to be able to prevent particle sintering.

Stabilizing agents that are present on colloid-derived model catalysts are removed in a manner that is very similar to regeneration. Palladium nanoparticles in particular, even when dispersed on a support material, aggregate into larger particles upon exposure to calcination conditions at temperatures milder than 300 °C.[64] This is thought to be the result of palladium oxide formation; oxygen can fully coat and oxidize a Pd(111) surface at pressures in the millibar range at temperatures as low as 150 °C, and

heating the surface to just under 200 °C under the same atmospheric conditions causes small clusters of PdO to form on the surface.[65] PdOx species exhibit a smaller wetting angle than that of pure Pd metal, conferring upon Pd oxide species a greater propensity to spread over a support once formed.[66] Pd particles of approximately 3 nm in size supported on alumina were found to spread on the surface of the support material upon being heated to 350 °C in air, while larger ones, about 35 nm in diameter, formed pits on their surface.[66] These pit formed at active sites on the surface of the larger particles, an indication that altering the properties of the Pd active sites on a particle by inclusion of Au in its structure may help prevent Pd mobility when heated.[66]

When the 0.7, 1.9, and 3.8 monolayer Pd@Au/SiO_2 catalysts were calcined and subsequently reduced to remove PVP from their surfaces in preparation for use as catalysts, it was found that, unlike the monometallic Pd/SiO_2 control which sintered and formed larger nanoparticles as expected, the Au-containing particles retained their size.[67] In this chapter, the characterization results that expose the morphological changes to the particles as they convert from core-shell to alloy are presented, along with those results that can be taken together to offer an explanation of how the inclusion of Au in the otherwise Pd particles works to prevent particle growth. It is hypothesized that the presence of Au in the particles can to a varying degree prevent the formation of PdO during pretreatment, but that the efficacy of including Au in the core-shell particles is correlated with the percentage of Au per particle. We see that while the size of all of the different types of particles are retained, there is a degree of oxide formation that takes place during the calcination of the 3.8 Pd@Au/SiO_2 particle that does not occur for the higher Au content bimetallic particles, as evidenced by TPR analysis. XAFS analysis corroborates the TPR results here, and suggests that there is partial segregation of Pd in

this sample in addition to alloying. Finally, the results of using the alloy particle catalysts in the vapor phase conversion of limonene to the aromatic product *p*-cymene demonstrates that in this case, the preservation of the particle size allows us to minimize the amount of Pd present per particle while maintaining a slightly better selectivity to the intended product when it is possible to select for any of several partially hydrogenated isomerized derivatives as well as the fully hydrogenated product.

3.1 Characterization of Pd@Au/SiO_2 to AuPd/SiO_2 Transition

3.1.1 TEM analysis showing concomitant alloying and preservation of particle size

Several different TEM and analytical electron microscopy techniques were employed to characterize the elemental composition, morphology and size of the Pd@Au particles in the treatment steps leading up to their use as catalysts. Conventional bright field TEM images taken of the Au/SiO_2, 3.8 Pd@Au/SiO_2, and Pd/SiO_2 samples before any treatment, and then after calcination in oxygen at 300 °C for 1h followed by reduction in 10% H_2/He for 1 h at 300 °C, demonstrate the variation in the morphological changes of the catalysts upon exposure to heat (Figure 11). Visually, it is very clear that the Au and 3.8 Pd@Au samples retain the same size distribution after exposure to treatment temperatures, whereas the Pd nanoparticles increase in size appreciably during the same process. Figure 12 shows the size distribution of each type of nanoparticle in terms of the average measured particle diameter, acquired from the direct measurement of at least 100 imaged particles per sample using ImageJ software. The distributions shown provide a quantitative depiction of the comparative constancy of the size of the Au and 3.8 Pd@Au particle sizes relative to the supported Pd particles.

These images strongly suggest that the presence of Au in the Pd@Au particles prevents the sintering of the nanoparticles on the support before being introduced into a catalytic reaction.

As already mentioned, the most likely cause of Pd particle sintering, at least in oxidative environments, is thought to be the conversion of Pd to PdO. Perhaps unsurprisingly, then, upon inspection of the particle morphology after each step in the pretreatment process, it was found that the Pd particles grow in size almost exclusively during calcination. Figure 13 shows conventional TEM images of the PVP-Pd/SiO_2 sample in particular at each step: as is, after calcination, and after calcination and subsequent reduction. In this side-by-side comparison of the catalyst structure, one can see that the Pd particles, initially 5 nm in diameter, reach a size of nearly 20 nm upon calcination, and do not increase in size any further upon continued heating in a reductive environment. This is supporting evidence that oxygen plays a principal role in the sintering process, and that the inclusion of Au in the Pd@Au nanoparticles fundamentally alters the high temperature interaction of Pd with O_2.

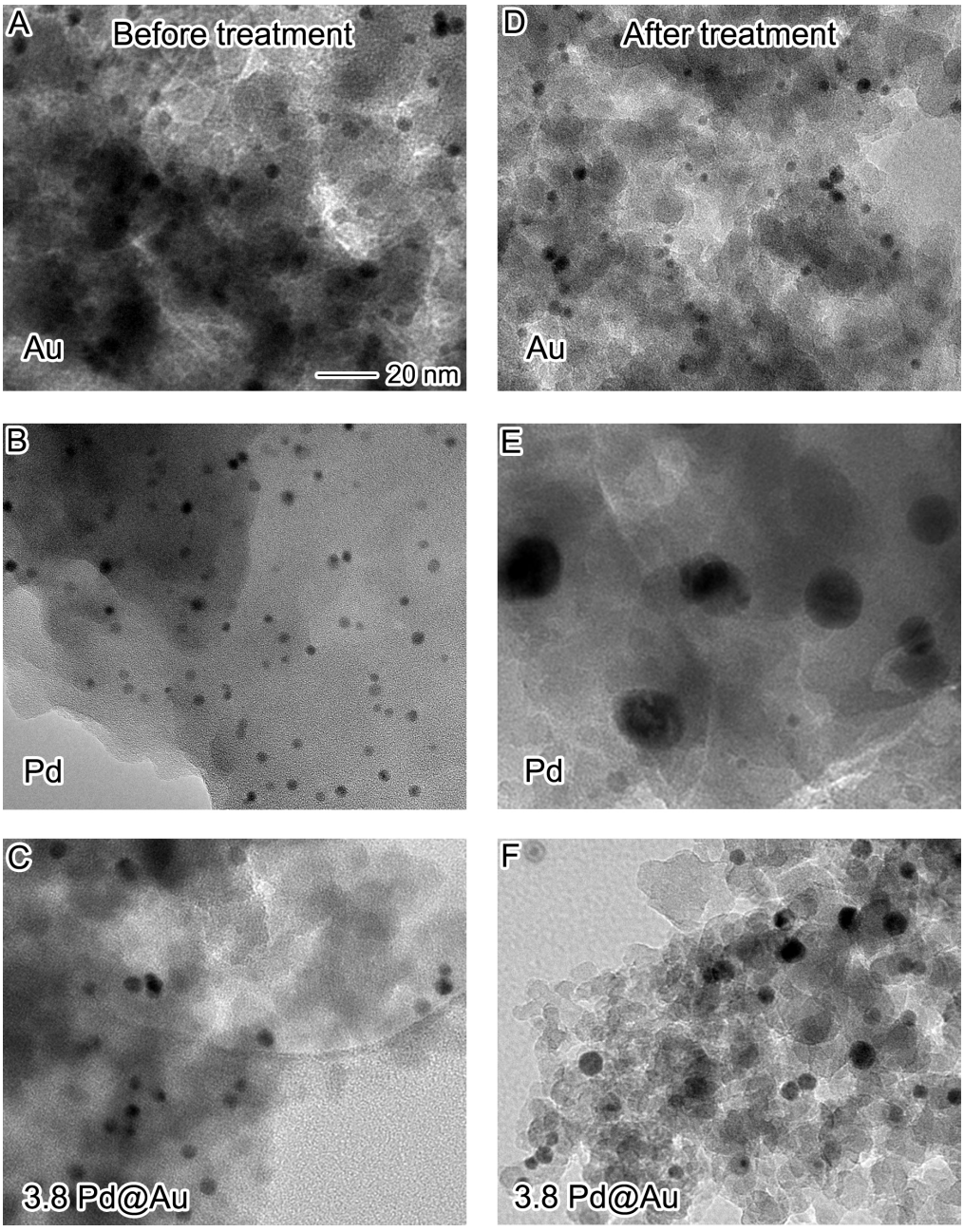

Figure 11: Conventional TEM images of the Au/SiO_2, $Pd@Au/SiO_2$, and Pd/SiO_2 samples as synthesized and after calcination at 300 °C for 1 h in air followed by reduction at 300 °C in 10% H_2/He for 1 h.

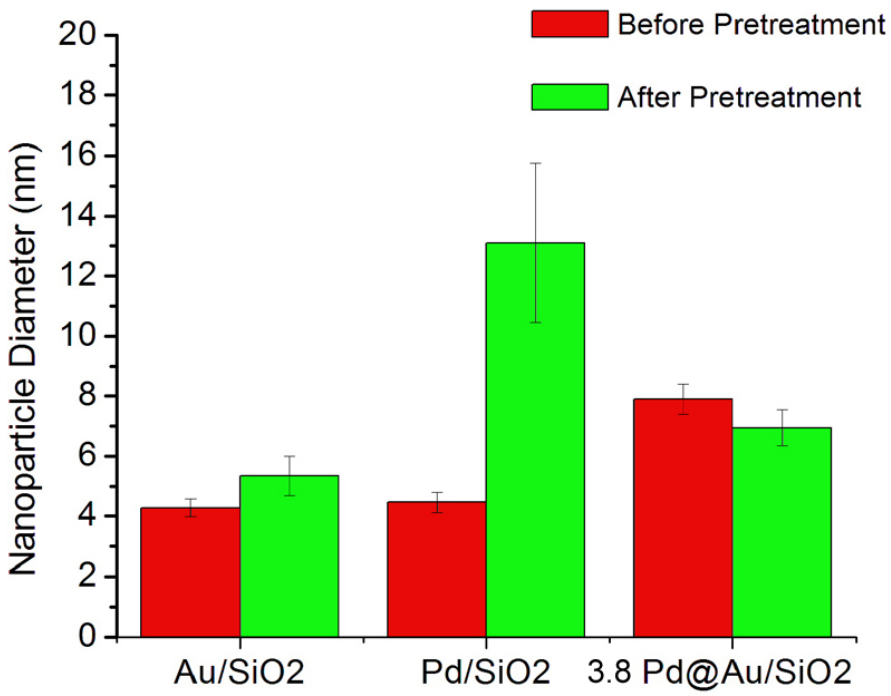

Figure 12: Size distribution of silica-supported Au, 3.8 Pd@Au, and Pd catalyst particles before and after pretreatment comprised of both calcination and reduction at 300 °C.

The 3.8 Pd@Au/SiO_2 sample was further analyzed at each pretreatment step using EDX-STEM mapping to visualize the relative positioning of Au and Pd within the particles, and to see the progression of changes to the core-shell morphology as a function of surface treatment conditions. Energy dispersive elemental maps of the as-is and fully treated particle catalysts initially revealed the core-shell to alloy transformation of the particles, and prompted acquisition of EDX images for intermediate treatment state to learn more about the elemental rearrangement. At each stage, a small portion of catalyst was dispersed in approximately 0.1 mL of MeOH, as

were typical samples during the process of specimen deposition for TEM analysis, but were also sonicated for 30 s in an effort to remove the particles from the silica support and thereby remove sources of resolution loss from the particle scans.

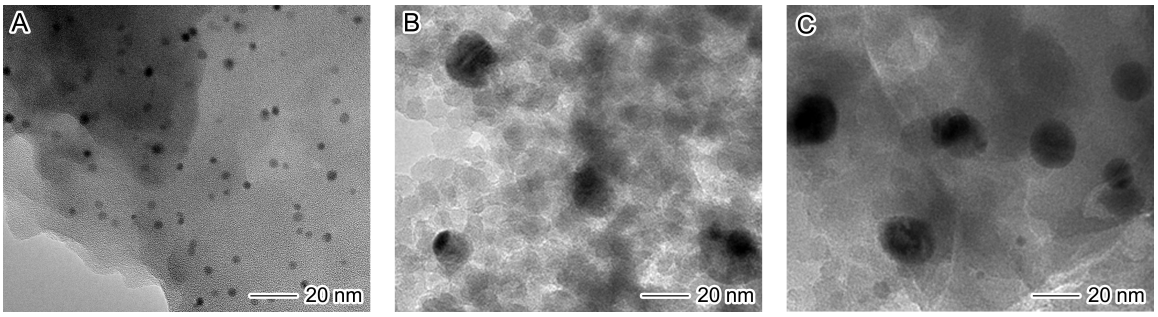

Figure 13: Conventional BF TEM images of Pd/SiO_2 showing the size distribution of the particles A) as is, B) after calcination in oxygen for 1 h at 300 °C, and C) after calcination as in B followed by reduction at 300 °C in 10% H2/He for 1 h.

Figure 14 depicts the energy dispersive x-ray (EDX) maps of representative 3.8 $Pd@Au/SiO_2$ particles as is (A - C), after calcination (D - F), and after calcination and subsequent reduction (G - I), as two-element overlays followed by the compiled image in terms of the single-element contributions from Au and Pd. The EDX image of the particles before treatment shows clearly the core-shell morphology of the nanoparticle; the single element map of the Au core shows that Au exists as a discrete core that is smaller in diameter than the area containing Pd, and the single-element Pd image shows that there is a higher intensity of Pd detected around the edge of where the Au core would be were it present, giving an intensity profile that one would expect for a uniform shell structure.[67] Once subjected to calcination conditions, however, the particles clearly transform to a homogeneous alloy, and there is no distinguishable difference in the single element maps shown in Figure 14E and F. This is another indication that the

presence of Au in proximity to surface Pd can inhibit the oxidation of Pd, as palladium oxide does not alloy with Au but typically segregates from it.[4]

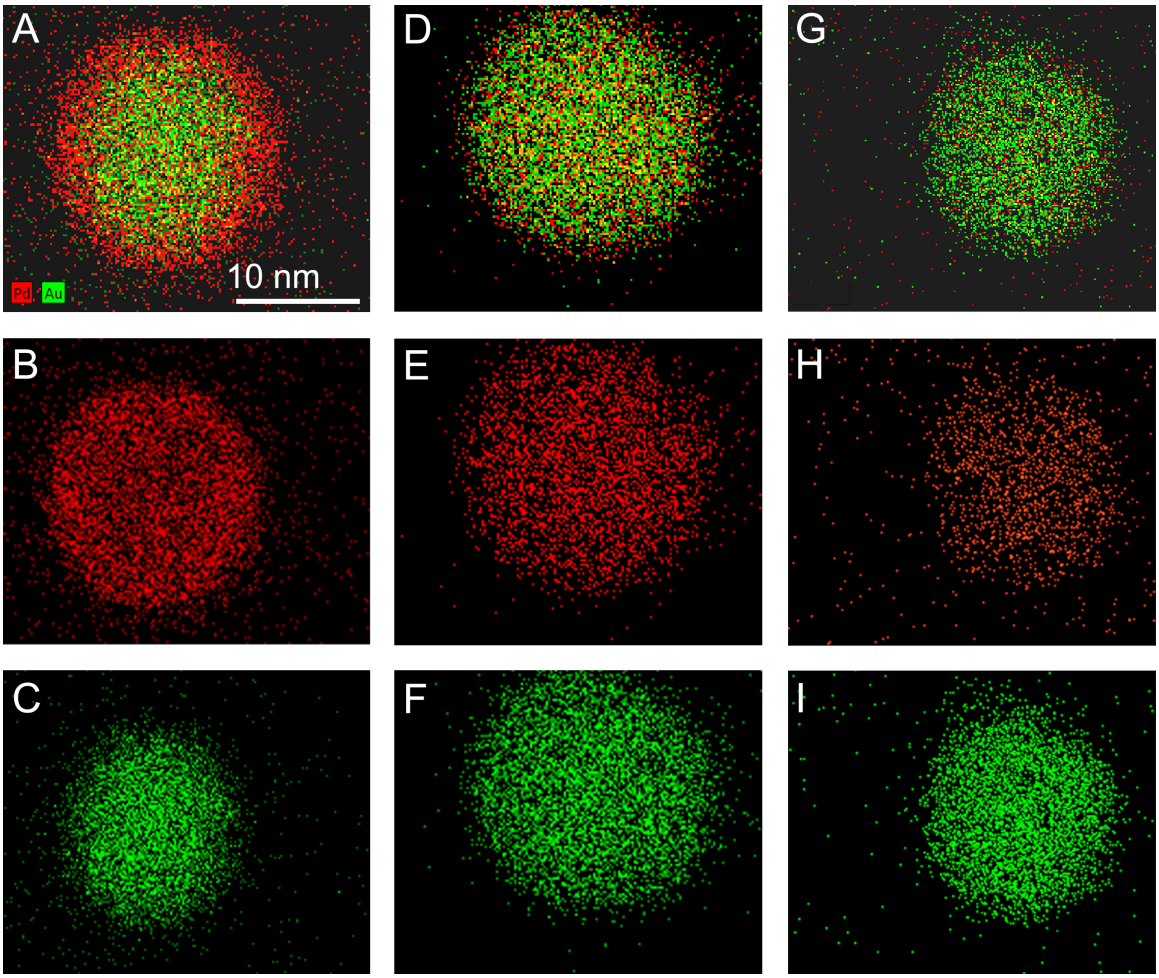

Figure 14: EDX-STEM images of the 3.8 Pd@Au/SiO_2 catalyst as-is (A - C), after calcination at 300 °C for 1h (D - F), and after calcination under the conditions specified followed by reduction at 300 °C for 1 h (G - I).

It is important to note here that a fraction of the particles scanned after calcination exhibited an alloyed structure as well as a degree of partitioning of Pd to one side of the nanoparticle. One such particle is shown in Figure 15 (note: the color coding of the elements in this case are reversed from the scheme in Figure 14). The particles

found to exhibit this morphological change were typically much larger than the size distribution range of the 3.8 Pd@Au/SiO_2 nanoparticles as measured in bright field mode. From this we can infer that the proportion of the particles which do grow by palladium oxide migration is a relatively small fraction, as particles selected for EDX analysis must first be found on the sample grid using of Z-contrast STEM imaging, and larger particles show up disproportionately by this technique; it is also easier to lock onto these samples long enough to collect the amount of x-rays required to build a successful rendering of each particle. Conversely, conventional bright field images are the result of several sources of contrast, and accurately display projections of smaller particles and larger particles, such that it is relatively safe to assume the distribution of sizes measured by this technique is accurate. As will be discussed, TPR and XAFS results indicate that the lower percentage Pd@Au/SiO_2 catalysts behave differently than the 3.8 Pd@Au/SiO_2.

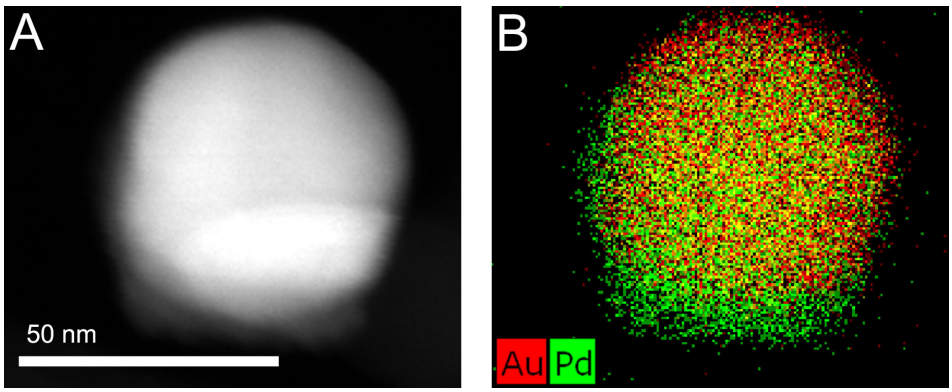

Figure 15: A) HAADF-STEM image and B) the corresponding EDX-STEM image of a 3.8Pd@Au/SiO_2 particle, post-calcination, displaying alloy formation as well as Pd segregation and significant particle growth.

Previous work in the literature has also revealed Au as an inhibitor of Pd oxidation, and has shed light on the underlying sources of the interaction. It has been

found in electrochemical investigations performed on AuPd bimetallic systems that thin layers of palladium deposited on a gold electrode oxidize at a higher applied potential relative to pure palladium electrodes.[68] In this study, the authors concluded that when the Pd overlayer is thin, it interacts with Au to practically make it easier to re-reduce the oxide of Pd once it does form than it is to reduce the oxidized surface of a thick Pd layer.[69] This suggests that the root of this interaction lies in an electronic interaction between Au and Pd. The inclusion of Au in Pd particle catalysts as an alloy has also been observed to increase the electrochemical potential at which surface oxide begins to form relative to Pd only catalysts.[70] Additionally, the electrochemical potential increases as the percentage of Pd present decreases, indicating that the more Au present, the more stable AuPd alloy particles are in the face of oxidative environments.[70] The authors here suggest, in agreement with conclusions drawn from the just-discussed work by Cadle, that this effect is electronic in nature, specifically a result of Au having a higher electronegativity than Pd and thereby exhibiting an electron-withdrawing effect on the surface Pd.[71] Because the 3.8 Pd@Au/SiO_2 particles have the highest palladium content of the three particles here, it follows that the alloying observed by EDX accurately describes the transformation of the lower Pd content catalysts as well; this is indirectly confirmed by DRIFTS analysis, to be discussed in the following subsection.

Additionally, analysis of AuPd alloyed surfaces of different composition using Auger electron and photoelectron spectroscopy revealed that when the alloy surface is Au-rich, it does not oxidize in the presence of oxygen between 300 and 600 °C.[71] Conversely, Pd-rich surfaces are coated with a layer of PdO under similar conditions; heating at 60% atomic weight Pd-Au alloy at 500 °C results in up to 90% of the Pd per particle migrating to the surface as a result of PdO formation.[71] This offers an explanation as to why the 3.8

Pd@Au/SiO_2 particles, coated with several very Pd-rich if not completely pure Pd monolayers, is susceptible to partial oxidation and the attendant Pd segregation observed.

3.1.2 DRIFTS analysis confirming alloying and showing transformation of surface sites

DRIFT spectra of adsorbed CO on the catalysts before and after calcination and reduction provides further evidence not only that the Pd@Au nanoparticles alloy during pretreatment, but also give an idea of the relative electronic states of the surface sites at the particle surface in both the core-shell and alloyed states. Figure 16 shows the DRIFT spectra of CO adsorbed on the surface of the Pd@Au catalysts before heat treatment, after being heated at 100 °C for 1 h in flowing H_2, and after the typical calcination and reduction heat treatments, respectively. The as-prepared catalysts, shown in Figure 16A, was initially treated in flowing H_2(g) at 25 °C to reduce any superficial oxide if present, something that, based on the EDX analysis of the 3.8 Pd@Au/SiO_2 after exposure and XAFS analysis of all of the samples, seems to be the case for the 3.8 but not the 1.9 or 0.7 Pd@Au/SiO_2 catalysts. The observed CO stretching frequencies on all of the Pd@Au catalysts fall at 2032 and 1932 cm^{-1}, and are assigned to linear (or atop) and two-fold bridging CO bound to Pd surface sites, respectively; these are in agreement with similar frequency assignments for adsorbed CO on various other reported Pd model catalysts.[69-72] The intensity of the CO bridging band is very strong for all of the catalysts, and the relative ratio of the bridging and linear intensities increases proportionally with the nominal thickness of the Pd shell surrounding the Au core. This indicates that the relative number of available multiatom surface sites increases with the Pd loading per particle, and this may be attributed to several possible differences in the particles. The

relative increase in multiatom sites may be due to the slightly larger area of the terrace sites on the particles with a thicker shell; the increase in diameter between the 0.7 and 3.8 Pd@Au particles translates into a 24% difference in particle surface area. An alternative explanation is that the closer the surface of the particle is to the Au core-Pd shell, the higher the degree of Au incorporation into the surface layer. XAFS data for the Pd@Au particles, to be presented later in this chapter, indicates that a degree of intermixing is present in the core-shell particles, which increases as the monolayer thickness of the Pd shell on the Au core decreases.

The decrease in multiatom sites could also be related to electronic interactions between the Au and Pd, which, based on the shifts of the CO stretching frequencies of CO adsorbed on Pd@Au relative to those found for Pd only, may have a non-trivial effect on the binding strength of adsorbates to the surface. Computational studies of PdAu(111) surfaces have shown that pairs of Pd atoms in first nearest neighbor positions on a Au(111) surface are energetically unfavorable, and furthermore that Pd-Au bonds are stronger than either homometallic bond on such a surface.[73] This may predict a certain degree of intermixing of Au at the surface of the bimetallic particles even before being subjected to heat that becomes more pronounced as the percentage of Pd per particle diminishes from 28.5% to 20.2% and finally to 10% (all in weight % of total metal) in the particles. It is also possible that the presence of PVP on the catalyst surface may contribute to the

The DRIFT spectrum of adsorbed CO on the Pd/SiO_2 (iw) catalyst, which is comprised of Pd particles that are on average 4 - 5 nm in diameter, makes for a stabilizer-free point of comparison to use in interpreting the spectra of the AuPd catalysts, and for assessing if, in fact, the increase in the relative bridging intensity on

these catalysts has to do with an increased Pd character of the surface. The monometallic catalyst synthesized *via* the incipient wetness method, shown in Figure 16, also exhibits stretching frequencies at 2094 cm^{-1} and 1990 cm^{-1} that can also be assigned to the atop and bridging frequencies of CO, but these are shifted by approximately 60 cm^{-1} to higher wavenumbers relative to the Pd@Au catalysts. The ratio of the heights of the bridging-to-atop peaks on the Pd/SiO_2 (iw) catalyst is, even larger than the relative ratio of the same two peaks of the 3.8 $Pd@Au/SiO_2$ in Figure 16A, making for another point that supports the correlation between the thickness of Pd at the surface of the particle and the number of multiatom sites on the surface of the particle.

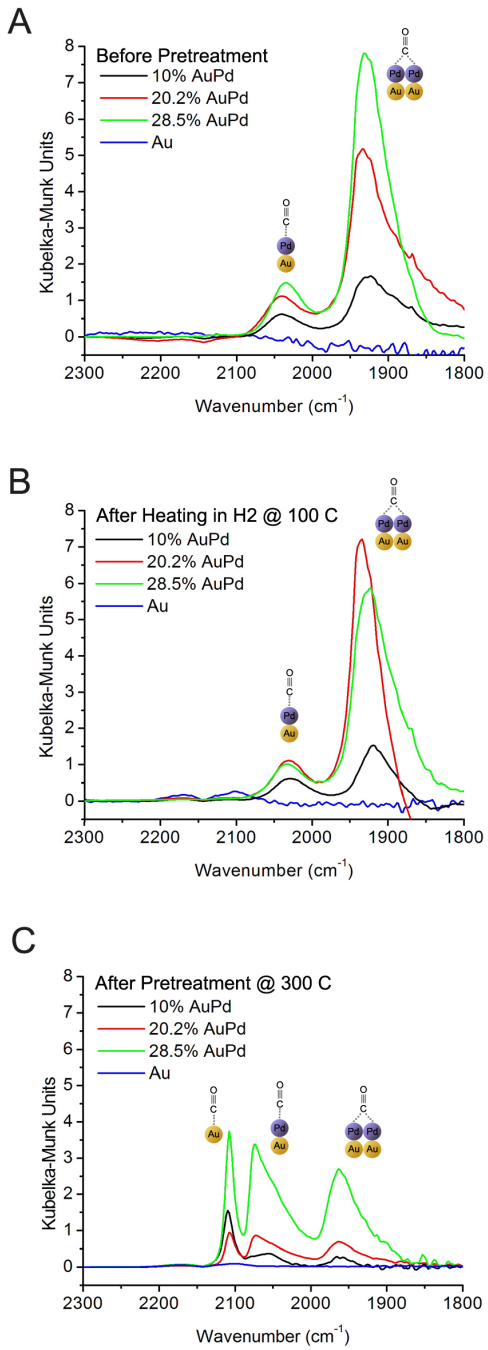

Figure 16: DRIFTS spectra of supported catalysts A) before calcination or reduction, B) after reduction (without calcination) at 100 °C, and C) after calcination and reduction at 300 °C. Catalysts are designated by the %Pd (w/w) present per particle.

The already-mentioned electronic shift of the Pd-CO bridging and atop stretching frequencies deserve further attention, because this even more directly reveals the electronic change of the surface due to bimetallic interaction that leads to the prevention of oxide formation. For supported Pd catalysts that have been completely saturated with CO, the bridging stretching frequency appears between 1990 and 1970 cm^{-1}, which fits with what would be expected for a combination of single crystalline (100) and (111) facets of Pd.[114-116] This is also in keeping with the observed features of the Pd/SiO_2 (iw). The relative decrease (i.e., red shift) in CO stretching frequencies that is observed when Au is present at the core of the particle suggests that Au is donating *d*-electron density to the Pd shell in the Pd@Au configuration. An increase in the electron density in the Pd d-state band would translate into a higher back donation to the anti-bonding pi orbital of CO, translating into a lower frequency vibration. This in turn can explain why Au inhibits Pd oxidation during calcination, in that Au moves the Pd *d*-band center away from the Fermi level and weakens its interaction with any adsorbed species, oxygen included.[74]

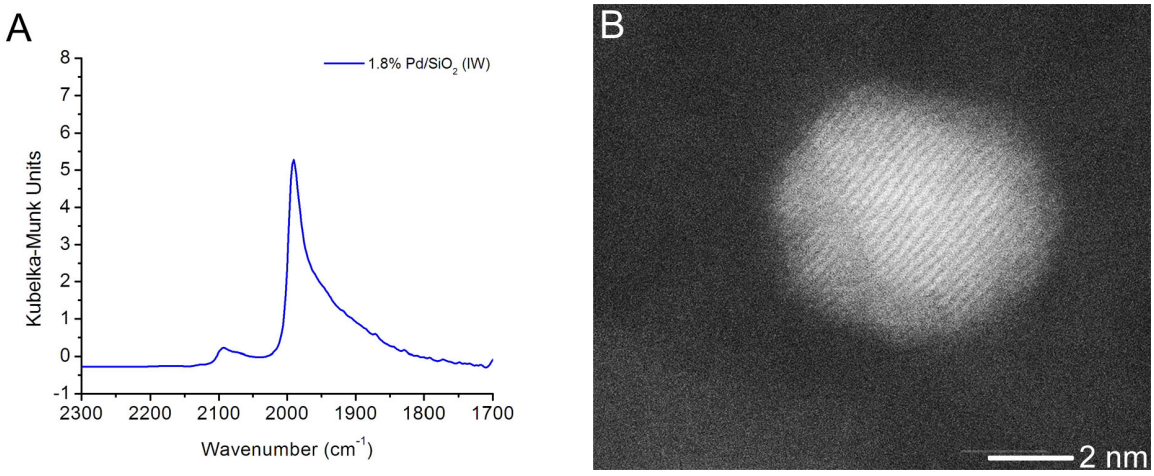

Figure 17: A) CO DRIFT spectra of Pd/SiO_2 (iw) prepared by incipient wetness impregnation after *in situ* reduction of the catalyst at 300 °C. B) HAADF-STEM shows the Pd particles on the (iw) catalyst at 1.78% (w/w) Pd loading.

The CO DRIFT spectra in Figure 16B were recorded after treating each Pd@Au catalyst in situ in flowing H_2(g) at 100 °C for 1 h, and are important to mention with respect to their qualitative similarity to those in Figure 16A. This indicates that the initial core-shell structure of the catalysts are retained after heating to 100 °C in a reductive environment. We do see here that the intensities of the 1.9 and 3.8 Pd@Au CO bridging stretches at 1932 cm^{-1}, taken in comparison to one another as heights normalized to the heights of the corresponding atop CO vibrational frequencies, are almost identical to one another and closely match what was seen for unheated 3.8Pd@Au/SiO_2 sample. This suggests that more multiatom sites were liberated on the 1.9 Pd@Au sample uniquely during this treatment; the cause of this is not entirely understood and could be attributed to either removal of a small amount of surface oxide or of PVP. It could also have to do with the release of a hydride upon heating of the 1.9 Pd@Au/SiO_2. In addition to confirming the retention of the core-shell morphology until the calcination step, this experiment also confirms that the presence of PVP on the particle surface does not prevent the adsorption of CO and therefore does not preclude catalyst activity, even in vapor phase reaction conditions. This conclusions has been reached in previously reported work as well.[75]

Three significant changes in the CO DRIFT spectra of the AuPd catalysts occur after the calcination and reduction of the Pd@Au/SiO_2 catalysts, as shown in Figure 16C. First, a stretching frequency that corresponds to atop CO bound to Au appears at 2100 cm^{-1} in each of the bimetallic spectra.[49] This indicates that Au has migrated to the surface of the particles. This conclusion is reinforced by the observation that the atop Pd-CO stretches observed after pretreatment are larger in intensity relative to the two-fold Pd-CO stretching frequencies present, which indicates that there is a break up of

multiatom Pd ensembles after heating. There is also a 28 cm^{-1} blue shift of the atop and bridging Pd-CO stretches to 2060 cm^{-1} and 1960 cm^{-1}, respectively. The blue shift of these frequencies suggests that upon the conversion from a core-shell to an alloyed structure there is a subtle shift of *d*-electron density from Pd to Au; however, this shift could also be due to the variations dipole-dipole coupling of the adsorbed CO species to one another that are dependent on the surface coverage of the catalyst.[76] In a CO DRIFTS study of AuPd bimetallic nanoparticles, it was found that the position of linearly bound CO on alumina supported Pd(111) shifted by 16 cm^{-1} to lower wavenumbers as the surface coverage of CO decreased.[90, 112, 114, 115] In our system, it is plausible to expect that once the particles alloy and allow for more linearly-adsorbed CO species to exist on the surface, the packing configuration of the of CO predisposes it to a higher degree of inter-adsorbate coupling and therefore a slight shift to higher stretching frequencies. The frequencies observed over the AuPd alloy catalysts are still red shifted from frequencies observed over monometallic Pd catalysts, like that seen in the analysis of the Pd/SiO_2 (iw) catalyst, which exhibited linear and bridging Pd-CO frequencies at 2090 cm^{-1} and 1990 cm^{-1}, respectively. This implies that there is still an overall red shift in the stretching frequencies when Au is present in the particles due to a transfer of *d*-electron density from Au to the Pd band, regardless of whether the morphology is core-shell or alloy.[49, 59] There is also a small peak present at 2050 cm^{-1} that closely matches a shoulder assigned by Marx *et al.* to CO linearly-bound to Au on AuPd alloy nanoparticles, and as such this peak can be tentatively interpreted as the same for the alloy AuPd particles.[59]

The frequencies of the CO adsorbed onto the surface of the nanoparticle catalysts gives an idea of the active surface site geometries of the Pd@Au, and how they change upon exposure to different treatment conditions. When the catalysts are exposed to

temperature conditions that facilitate conversion to an alloy ordering scheme, there is a break up in multiatom Pd ensemble sites, indicating a migration of Pd to the interior of the particle. Au also acts as an active surface site, and introduces weakly binding surface sites to the particle surface. Together, these two phenomena make the particle surface overall a weaker binding surface for adsorbates, including oxygen. The red shift of the Pd-bound stretching frequencies on the AuPd and Pd@Au catalysts, regardless of the morphology, relative to the same types of stretches on Pd only catalysts indicate that the presence of Au does indeed, through electronic interactions with Pd, weaken the binding strength of O (and presumably other adsorbates) such that the formation of PdO is less likely. The overall intensities of the stretching frequencies, in fact, on the three types of alloy particle suggests that for the 10 and 20.2% Pd per particle alloy catalysts, the overall amount of bound species is severely diminished when compared to the intensity observed on the core-shell particles (*Fig 12A*) and also when compared to the degree of CO adsorption observed on the 28.5% AuPd catalyst. This disparity in behavior also points to a composition dependency on the ability of Au to prevent oxidation of Pd; the apparent increase in surface sites that is observed on the 28.5% AuPd catalyst could mean that enough oxygen can adsorb during exposure to cause the degree of oxide observed by TPR and XAFS and discussed below.

3.1.3. XAFS analysis of Pd@Au/SiO_2 catalysts

As a bulk technique, XAFS is still useful for determining the oxidation states of the metals that constitute a supported nanoparticle catalyst sample. Additionally, due to the high surface-to-volume ratios of nanoparticles, the data gathered by this technique does provide surface sensitive information in this case. Analyses of the three catalyst

samples after the several of the same treatments analyzed using DRIFTS - as is, after heating in H_2 at 100 °C, after calcination at 300 °C, and after calcination and subsequent reduction at 300 °C - are shown in Figure 18, Figure 19, and Figure 20. It should be noted that the number of spectra acquired at the Advanced Photon Source was limited by time constraints, and for this reason, the XAFS spectra of 0.7 and 1.0 Pd@Au/SiO_2 alloy samples (that is, the samples subjected to calcination conditions) were not collected.

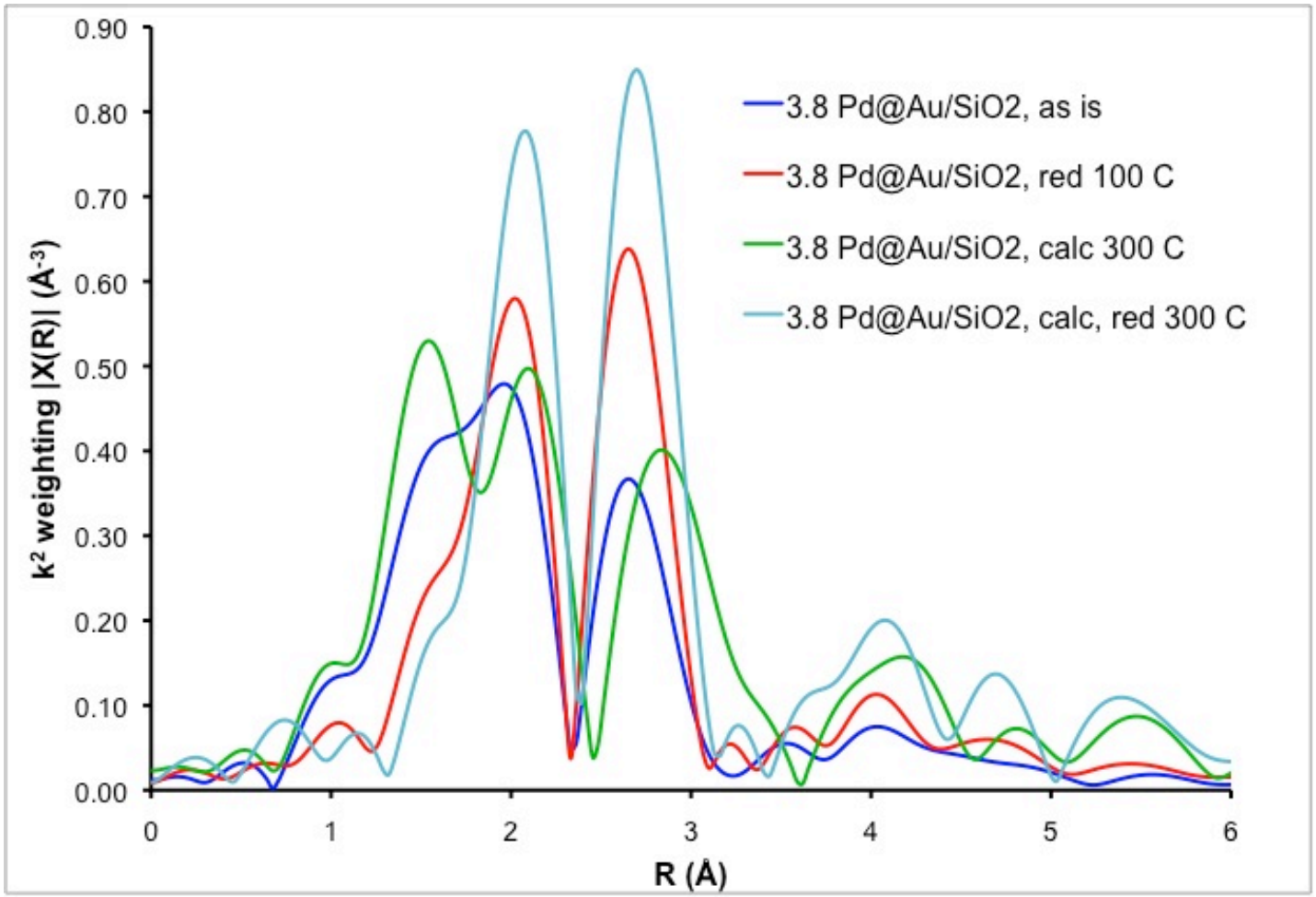

Figure 18: Pd K edge XAFS data for the 3.8 Pd@Au/SiO_2 catalyst as is, after reduction at 100 °C, after calcination at 300 °C, and after calcination and subsequent reduction at 300 °C over a k-range of 2.2 - 10.

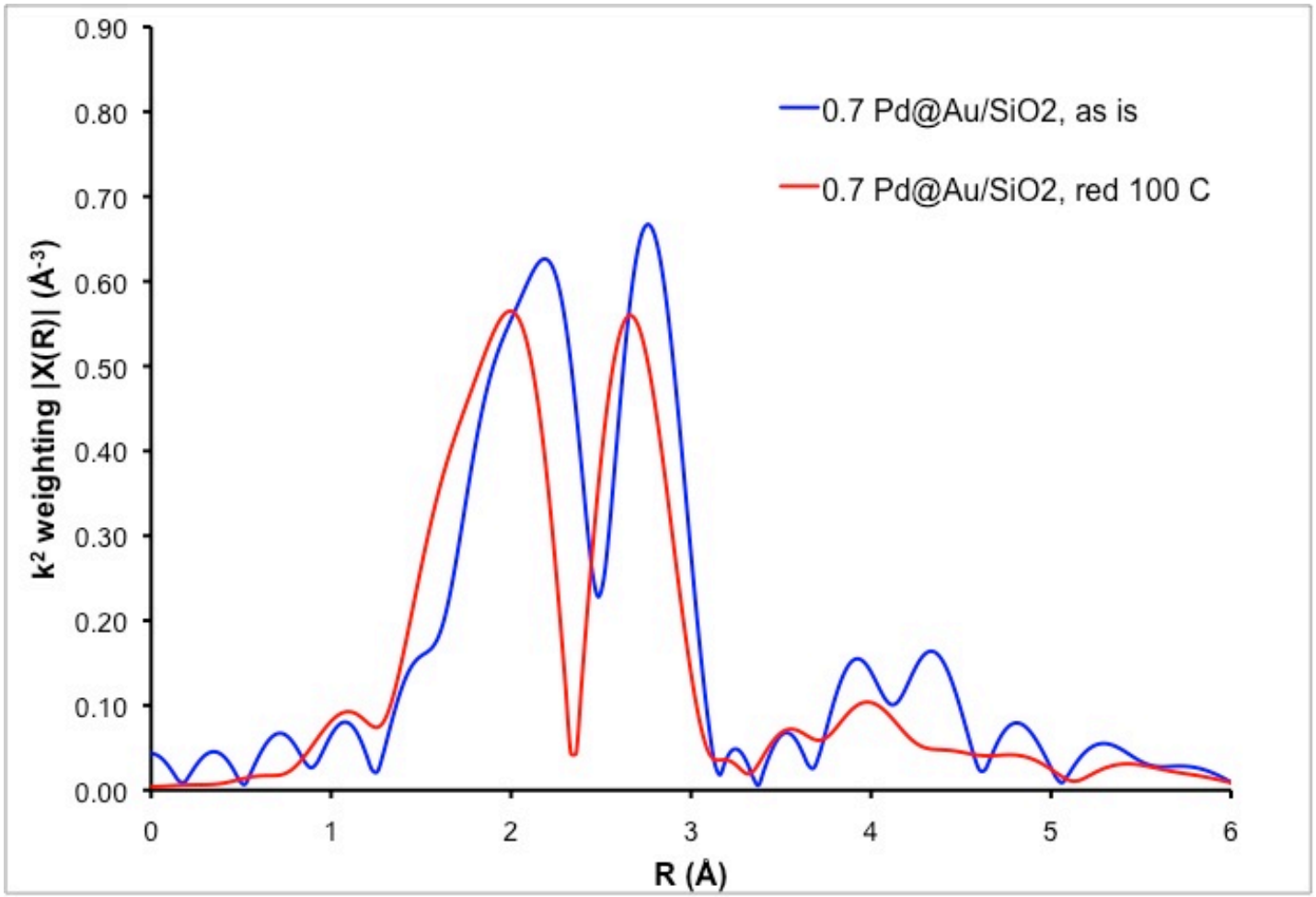

Figure 19: Pd K edge XAFS data of 0.7 Pd@Au/SiO_2 catalyst as is and after reduction at 100 °C in H_2 (k-range = 2.5 - 11.2).

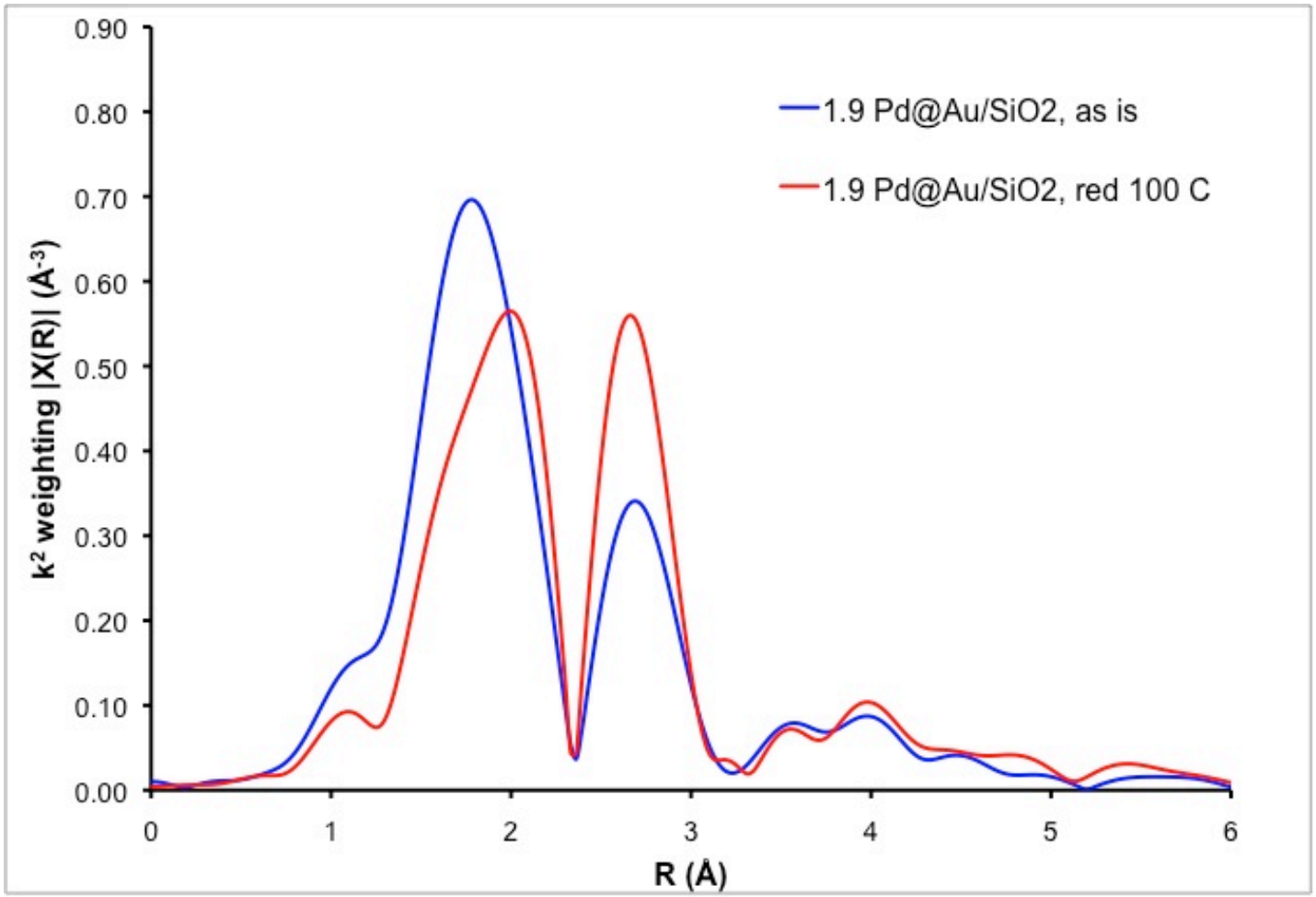

Figure 20: Pd K edge XAFS data of 1.9 Pd@Au/SiO_2 as is and after reduction at 100 °C in H_2 for 1 h (k-range = 2.0 - 10.2).

Figure 18 shows the XAFS data collected at the Pd K edge for the 3.8 Pd@Au/SiO_2 catalyst at each step in the pretreatment process, and as such, is useful to discuss first in terms of teasing out absorber-backscatterer interactions present in the data. It is immediately apparent that the catalyst undergoes significant changes at each step in the treatment process. When considering the potential interactions of a Pd absorber in the Pd@Au nanoparticle environment, there are two backscattering species that are certain to factor into the overall appearance of the data: the Pd absorber - Pd backscatterer (Pd-Pd) pair and the Pd absorber - Au backscatterer (Pd-Au) pair. For this reason both types of interactions are included in the theoretical model that is used to fit the data depicted here. Because the samples are bimetallic in nature, the theoretical model was constructed using a crystal containing a 1:1 atomic ratio of Pd and Au atoms. Additionally, a Pd-O contribution was factored into the theoretical model during the fitting process. This third contribution, that of Pd photoelectron-waves backscattering from O results in a significant Pd-O bond distance contribution to the XAFS data shown in Figure 18 around R of approximately 2.07 Å for the "as is" sample and at 2.04 Å for the sample exposed to calcination conditions. Note that the values for the bond distances are calculated by fitting the data shown with a theoretical model in which shifts in the phase are considered, and as such, the bond distances are not directly readable from the data in Figure 18, Figure 19, and Figure 20, which have not been phase-shift corrected. In these figures, the Pd-O contribution falls around 1.5 Å. We see that before exposure to any treatment, the 3.8 Pd@Au/SiO_2 catalyst has an appreciable amount of oxide present; the Pd-O contribution to the data is almost as large here as is present after calcination. This peak is not present on the data acquired on "as is" 0.7 Pd@Au/SiO_2 or 1.9 Pd@Au/SiO_2 (Figure 19 and Figure 20), a testament to the inherently different,

monometallic Pd-like nature of the 3.8 Pd@Au/SiO_2 compared to the 0.7 Pd@Au/SiO_2 and 1.9 Pd@Au/SiO_2 samples.

For comparison, the XAFS data for the untreated monometallic Pd/SiO_2 catalyst at the Pd K edge, plotted in R space, is shown in Figure 21. The fit shown was produced by including theoretical input files that describe the crystal structures of Pd metal and PdO. In general, fits to XAFS data are optimized by minimizing a chi function that is dependent on the real and imaginary parts of the Fourier transform of the theoretical contributions. The output of the fit gives the best fit of the minimization process for the coordination number, coordination distance, Debye-Waller factor, and energy edge shift, along with the associated uncertainties. These uncertainties are composed of contributions of noise as well systematic error sources, like sample inhomogeneity, detector response, background removal errors, and the like.

The parameters of the fit of the monometallic Pd catalyst, as well as the fit for the 3.8 Pd@Au/SiO_2 in the two oxidized samples ("as is" and calcined), are shown in Table 3. The R-factor of the fit to the monometallic Pd sample, which comprised of Pd-Pd and Pd-O contributions only, at 0.0242, is a so-called "good" fit, and on average, each Pd absorber is surrounded by 9.8 other Pd atoms, but also 1.6 O atoms. The same peak on the "as is" and calcined 3.8 Pd@Au/SiO_2 samples, when fit considering the contributions of scattering from Pd, Au, and O, return Pd-O coordination numbers of 1.67 $\pm$ 0.78 and 1.69 $\pm$ 0.68, respectively, indicating that in each case the coordination of Pd to O is to the same degree as a monometallic surface, even though there is on average a significant presence of metal backscatterers surrounding the Pd absorbers in these samples. Also telling is the loss of the oxide peak once the sample is exposed to reducing conditions, as there is notably no loss of a peak below 2 Å in terms of details in R-space when the 0.7

Pd@Au/SiO_2 and 1.9 Pd@Au/SiO_2 samples are reduced at 100 °C. These observations are evidence that the presence of Au at compositions above 80% in our core-shell particles is effective in preventing oxidation of the superficial Pd.

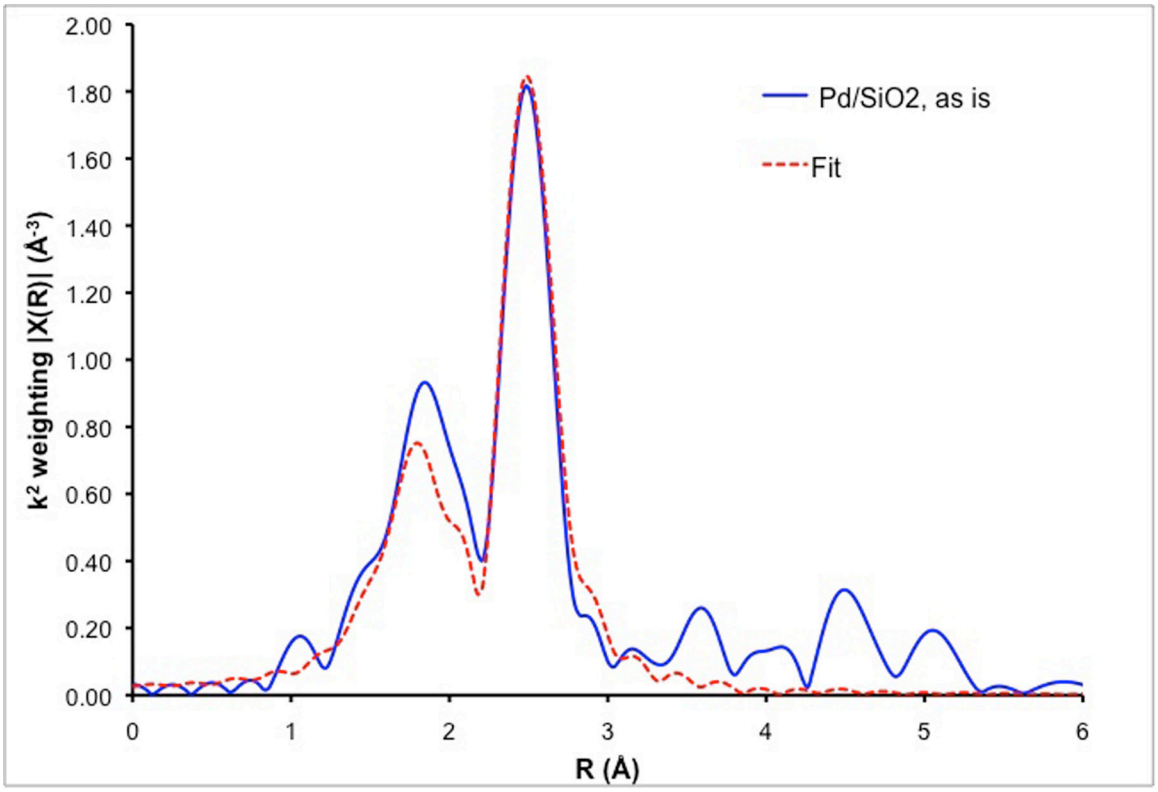

Figure 21: XAFS data at the Pd K edge collected for the monometallic Pd/SiO_2 catalyst without exposure to any treatment (k-range = 2.5 - 11.4).

On the other hand, quantitative fit analysis carried out on the 3.8 Pd@Au/SiO_2 catalyst after calcination and reduction further reveals the loss of any robustness imparted by Au once its composition drops to below 80% in 5 nm core-shell particles. The Pd K edge XAFS data collected for this sample is shown in Figure 22, and the fit

parameters, determined over a Fourier transform range of k = 2.5 - 11.4 and a fit range of R = 1.29 - 3.14, are included in Table 3.

Table 3: Pd K edge (and Au LIII edge where acquired) fitting parameters for untreated Pd/SiO_2 and 3.8 $Pd@Au/SiO_2$, as is, after reduction at 100 °C, after calcination at 300 °C, and after calcination and reduction. S_0^2 was set to 0.76 for fitting Pd absorber data, and to 0.88 for Au absorber data. [a]The coordination number of backscatterers surrounding the absorbing atom; [b]average bond distance between absorber and backscatterer; [c]Debye-Waller factor, [d]shift from the absorption edge to fit the data; [e]measure of the goodness of fit.

catalyst	treatment	absorber	backscatterer	N[a]	R[b]	σ^2 (10^{-3})[c]	ΔE^2 [d]	R-factor[e]
Pd/SiO_2	as is	Pd	Pd	9.8 ± 1.6	2.76 ± 0.006	8.1 ± 0.8	-4.1 ± 1.5	0.0242
		Pd	O	1.6 ± 1.0	2.16 ± 0.02	2 ± 4	(9)	
3.8$Pd@Au/SiO_2$	as is	Pd	Pd	1.4 ± 0.6	2.74 ± 0.03	5 ± 7	(-8)	
		Pd	Au	5.3 ± 2.3	2.78 ± 0.01	8 ± 7	(-6)	
		Pd	O	1.7 ± 0.8	2.07 ± 0.03	8 ± 8	9.2 ± 3.4	
3.8 $Pd@Au/SiO_2$	air/300 °C	Pd	Pd	1.1 ± 0.9	2.77 ± 0.03	-0.1 ± 6	(-9)	
		Pd	Au	6.3 ± 2.0	2.86 ± 0.03	5 ± 4	-2.5 ± 2.7	
		Pd	O	1.7 ± 0.7	2.04 ± 0.01	2 ± 5	(9)	
3.8 $Pd@Au/SiO_2$	H_2/100 °C	Pd	Pd	3.7 ± 1.2	2.79 ± 0.02	8.2 ± 3.7	(-7)	0.01747
		Pd	Au	6.7 ± 2.3	2.79 ± 0.01	9.6 ± 5.1	(-6)	
		Au	Pd	1.5 ± 0.5	2.77 ± 0.02	8.0 ± 2.2	3.5 ± 2.9	0.0092
		Au	Au	9.0 ± 0.8	2.84 ± 0.006	8.1 ± 0.6	4.9 ± 0.9	
3.8 $Pd@Au/SiO_2$	air/300 °C, H_2/300 °C	Pd	Pd	3.7 ± 0.6	2.80 ± 0.01	6.6 ± 1.6	-6.1 ± 1.3	0.00201
		Pd	Au	7.8 ± 0.9	2.79 ± 0.009	6.6 ± 1.4	-5.9 ± 1.0	
		Au	Pd	2.6 ± 0.5	2.81 ± 0.01	7.1 ± 1.4	4.8 ± 1.6	0.00742
		Au	Au	8.1 ± 0.8	2.83 ± 0.008	7.6 ± 0.7	4.8 ± 1.0	

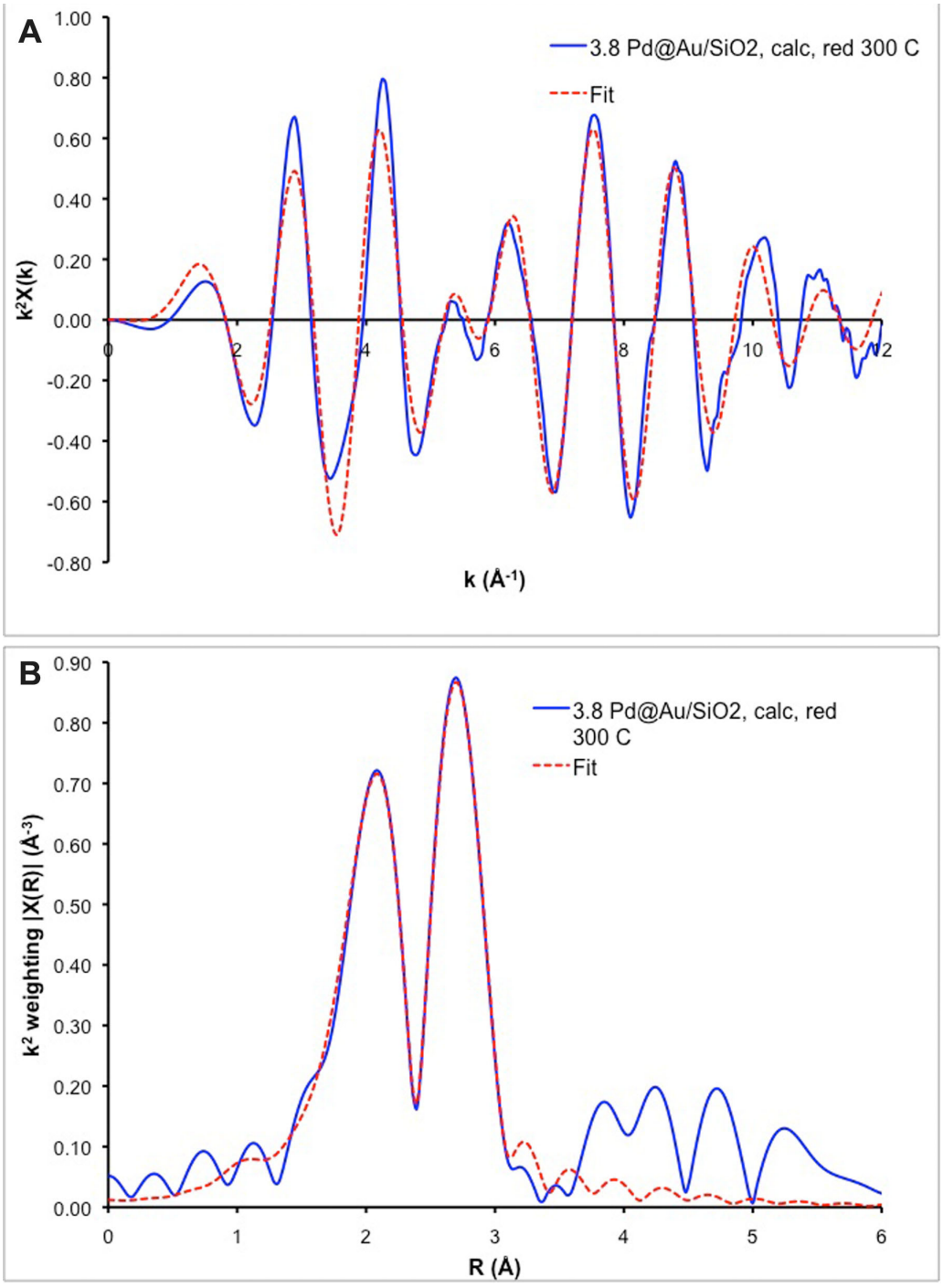

Figure 22: Pd K edge XAFS data (blue solid line) and calculated first-shell fit (red dashed) in *k* and *r* space for the 3.8 Pd@Au/SiO_2 catalyst after calcination and subsequent reduction at 300 °C for 1h (k-range = 2.5 - 11.4, R-range = 1.29 - 3.14).

The data for the 3.8 Pd@Au/SiO_2 sample after reduction at 100 °C and after calcination and reduction at 300 °C is interesting in that it allows comparison of the differences in the structure after being exposed to treatments at a lower and higher temperature. The coordination numbers for the Pd absorber after being heated to 100 °C and 300 °C are 10.5 and 11.5, respectively, implying that Pd has moved more fully into higher coordination sites - i.e., has alloyed more extensively - in the latter case. Of these coordination shells, there are on average 6.7 and 7.8 Au atoms surrounding Pd, again pointing to an overall diffusion of Pd more fully into the Au bulk of the particle after calcination and reduction. We also observe a slight decrease in Au-Au bond distance once the particles have been treated with oxygen and hydrogen at 300 °C. Vegard's law, which describes the linear correlation between bond distance and composition in alloys, forms the basis for ascribing this decrease as an indirect indicator of a higher degree of Pd diffusion into the Au core, as Pd, with a bond distance of 2.75 Å, would lower that lattice parameter of a AuPd alloy structure as the mole fraction of it increases. The σ^2 values of calcined and reduced 3.8 Pd@Au/SiO_2 are consistently lower than those of 3.8 Pd@Au/SiO_2 reduced at 100 °C, signifying that the sample treated at higher temperature exhibits a lower degree of static disorder and thus possesses a more homogeneous metal distribution. For both treatments regimes of 3.8 Pd@Au/SiO_2, the Pd absorber NN distances are at intermediate values between the Pd-Pd (2.75 Å) and Au-Au (2.88 Å) bond distances in the pure metal lattices, as predicted by Vegard's Law. The Au-Pd NN distances are somewhat interesting: for example, the Au-Pd value for the 100 °C reduced 3.8 Pd@Au/SiO_2 is 2.77 ± 0.01 Å, which is smaller than the Pd-Au bond distance for the particle (2.79 ± 0.02 Å). Although, statistically, these two values are the same, this trend in magnitudes has been observed for supported PdAu alloy particles previously, and the

lattice contraction of 0.02 Å observed in that case was attributed to local ordering of Au and Pd that arises from an exothermic heat of mixing of Pd and Au.[77] The value of the Au-Pd NN distance for the calcined and reduced sample is 2.81 Å, larger than in the low-temperature reduction sample, likely because of a relative expansion of the lattice surrounding each Au on average, as the Pd is now dispersed more fully throughout and is effectively a more dilute backscatterer. There is a loss of any contribution of Pd-O scattering interactions to either data set, indicating the removal of oxide after heating in H_2.

The fits for the XAFS analysis of the samples in the context of bimetallic intermixing will be discussed in more quantitative detail in the next chapter. The XAFS results presented here back up the hypothesis that Au acts to prevent oxidation in core-shell particles, with its efficacy dependent on the amount of Au per particle.

3.1.4 Temperature-programmed reduction of Pd@Au/SiO_2 catalysts to assess the degree of oxidation upon calcination

Temperature-programmed reduction (TPR) data was collected for all of the samples after subjecting them to calcining conditions. The results reveal that there is a composition-dependence to the oxidation inhibition capability of Au present in otherwise Pd catalyst particles. The TPR results for each catalyst as a function of reduction time are shown in Figure 23. These profiles are the result of the initial interaction of the sample with 5% H_2 in Ar carrier gas as the temperature of the sample was increased to 300 °C at a constant rate of 10 °C/min, and as such, since they were initially in a calcined state, represent the amount of reducible species present on the sample in terms of the volume of hydrogen uptake. The results of the three catalysts are drastically different from one another, though the only variable is the amount of Pd present per particle. The trends in the data are thought to arise from the degree of Au

present near the surface, which correlates with the reported propensity for Au-rich alloys to experience Au surface enrichment at bulk molar fractions of Au above approximately 0.45, as calculated from surface energies using a regular solution model.[90, 116] Figure 24 is a reproduction of regular solution and ideal solution calculations reported by Reifsnyder *et al* that show the degree of surface enrichment as a function of the bulk molar fraction of Au in AuPd alloys which demonstrates the principle that Au-rich alloys are more likely to have a increase in Au segregation to the surface.[59] It is interesting to note that this model predicts that bulk alloys with a composition of more than 40% Au will have a Au enriched surface, yet the 3.8 Pd@Au particles have clearly displayed a tendency for Pd to remain at the surface of the particle and oxidize from our characterization results. This disparity can be explained by the core-shell morphology of the 3.8 Pd@Au particles: because most of the Pd is present in a Au-poor region of the particle, it effectively falls on the lower bulk composition end of the chart in Figure 24. Thus, the Pd shell surface is self-sustaining, thereby exposing itself to oxidation. In addition to indicating that shells larger than 2 monolayers of Pd lose the beneficial effect of having Au present in terms of oxide prevention, this also supports the hypothesis that there is a degree of intermixing of the Pd and Au at the interface in the 0.7 and 1.9 Pd@Au particles that allows them to behave as an alloy would. Slight intermixing would render the composition of Au in the shell to be lower than the overall percentage of Au in the particle, but for the 0.7 and 1.9 Pd@Au particles, with bulk Au compositions of 90% and 80% (w/w), respectively, this value is likely still above 40% Au at the surface.

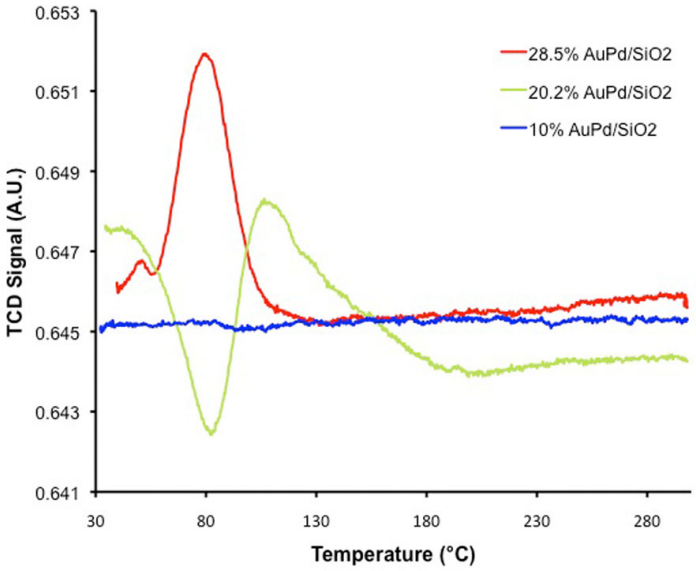

Figure 23: Comparison of TPR data collected over the alloyed catalysts after having been subjected to calcination conditions.

The 3.8 Pd@Au/SiO_2 catalyst, however, when analyzed after exposure to calcination conditions, exhibits a significant H_2 uptake peak within 5 min, at a temperature of 77 °C, indicative of the reduction of an oxide species on the catalyst. This tells us that the lower composition of Au in the 3.8 Pd@Au particles reduces its ability to completely prevent oxide formation. This could be due to the higher proportion of multiatom Pd ensembles on the surface of the 3.8 Pd@Au/SiO_2 catalyst (see Figure 16A), making it easier to form a more tenacious bond to adsorbates, and making it behave most like a monometallic Pd catalyst, out of all of the Pd@Au catalysts. Perhaps most interesting is the behavior of 1.9 Pd@Au/SiO_2 after calcination and upon first exposure to H_2 under increasing temperatures; not only does the 1.9 Pd@Au not uptake H_2, it *releases* a significant amount of H_2. The position of the hydrogen sorption peak for this sample in terms of temperature, occurring at 80.2 °C, is close to the temperature reported for the desorption of hydrogen from bulk palladium in a Pd/SiO_2 catalyst formed by the cation exchange

preparation method (90 °C).[44] This will be discussed further in the context of subsurface hydrogen reserves within the particles in the next chapter, but important here is that, again, the presence of Au seems to be effective in inhibiting the oxidation of Pd.

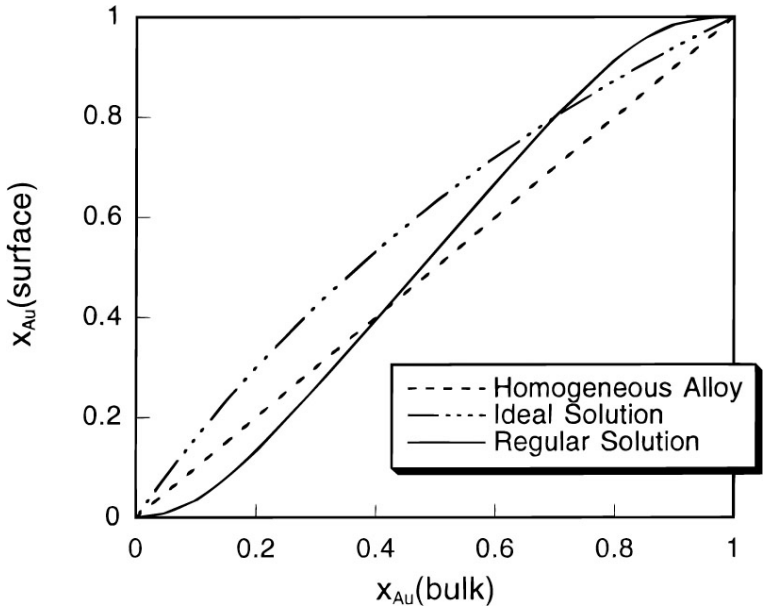

Figure 24: Surface enrichment of AuPd alloys as a function of Au molar fraction in the bulk of the material.[44]

3.2 Observation of the effects of sintering prevention in the Pd catalyzed conversion of α−limonene to p-cymene

The utilization of the alloy AuPd particles in the high temperature conversion of α-limonene to its fully dehydrogenated form, *p*-cymene, demonstrates the practical utility of being able to prevent sintering through adding a high percentage (greater than 80% Au per particle) of Au to the nanoparticles. The performance of the alloyed particles was compared to that of both monometallic Au and Pd silica-supported nanoparticles, as well as monometallic silica-supported Pd catalysts prepared by incipient wetness (iw) and ion exchange (i.e.) methods.

The production of *p*-cymene is an industrially practical reaction to study because it is used in the production of resins, fragrances, pesticides, and industrial solvents, and as such it is a valuable material.[44] Traditionally produced from petroleum feedstocks, it has been found that one potential method for generating *p*-cymene in an environmentally friendly way is to dehydrogenate α-limonene, an abundant chemical waste product of the citrus juice industry.[120-123] Both Pd and Au have been tested as monometallic catalysts in the conversion of limonene to *p*-cymene, and it has been found that while Pd catalyzes the conversion with high selectivity, Au exhibits almost no activity.[78] In these investigations, it was proposed that the production of *p*-cymene proceeds through the full hydrogenation of limonene to form *p*-menthane as an intermediate.[78] There have been, however, no investigations into the performance of supported AuPd nanoparticle catalysts in selectively converting limonene to cymene. Using the AuPd alloy nanoparticle catalysts to catalyze limonene conversion, affords the opportunity to probe how the addition of Au to Pd, and the preservation of the nanoparticle size stemming from this addition, alters the reaction pathway.

As the reaction data in Figure 25 demonstrates, the solution-phase synthesized catalyst particles are active for the conversion of limonene to *p*-cymene.[121, 124] The AuPd/SiO_2 catalysts in particular, above a certain threshold amount of Pd per particle, demonstrate a particularly high conversion to *p*-cymene; the yield of *p*-cymene was 65.5, 83.2, and 84.1% over the 10, 20.2, and 28.5% AuPd/SiO_2 catalysts, respectively, and for all bimetallics, limonene was completely converted to other products. As discussed in the introduction, three other terpinene isomers of limonene were monitored for during the reaction: α-terpinene, γ-terpinene, and terpinolene (see Figure 10). Conversely, limonene was only partially converted when passed over the monometallic Au/SiO_2 and SiO_2 controls: only 54% was converted over the former and 60% over the latter. In

addition to a drop in the activity when Pd was not present, a decrease in the selectivity was also observed over the catalysts that did not contain Pd, with only 18% of limonene that was converted being transformed to *p*-cymene over the Au/SiO_2 catalyst, and the rest of the product stream leaving the reactor as a mixture of menthane, α-terpinene, and other unidentified products.

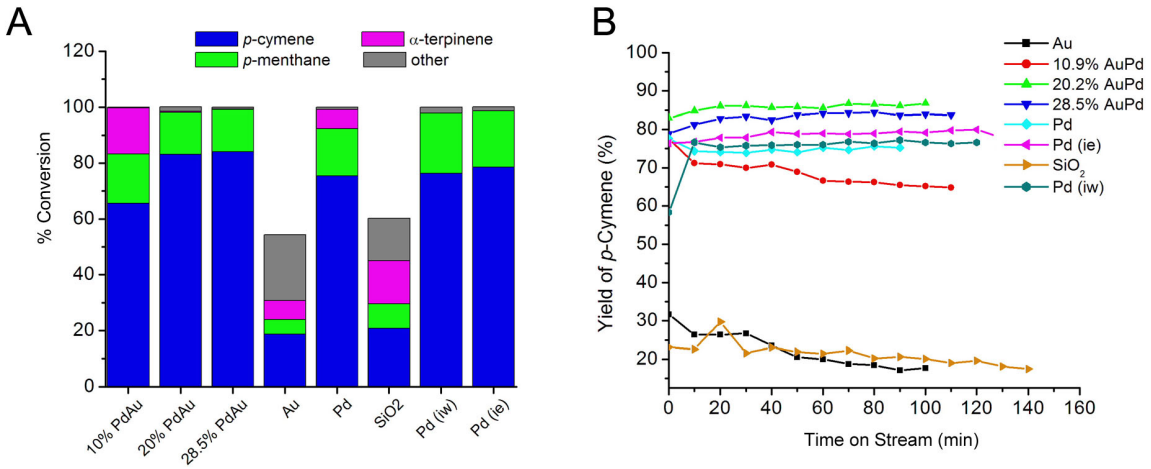

Figure 25: The A) average percent conversion of limonene to various products over AuPd catalysts and monometallic control catalysts and B) the yield of *p*-cymene over each catalyst as a function of reaction time.[4] Conversion of limonene was carried out at 250 °C under a stream of 50 sccm H_2 and limonene injected continuously at 6 uL/min.

The monometallic Pd catalysts, as expected, all performed similarly to one another, fully converting limonene as it flows through the fixed catalyst bed and yielding approximately 80% *p*-cymene in the product stream. While there was a very small percentage of unidentified product that appeared in the mixture of products for all of the Pd/SiO_2 catalysts, the PVP-coated Pd/SiO_2 also generated an appreciable amount of α-terpinene, while the incipient wetness and ion exchange catalysts yielded only *p*-menthane. This difference may be attributable to the initial presence of PVP on that catalyst. The 10% $AuPd/SiO_2$ catalyst also yielded α-terpinene, while the 20 and 28.5%

AuPd catalysts did not. Additionally, as shown in Figure 25B, the non-Pd containing Au/SiO_2 and silica catalysts readily deactivated with time, whereas the productivity of the Pd-containing catalysts was relatively constant as their time on stream progressed.

Focusing on the selectivity of each of the Pd-containing catalysts to *p*-cymene brings an interesting point to light, which is that the higher Pd-loading $AuPd/SiO_2$ catalysts are more selective to *p*-cymene than any of the Pd catalysts, as is most visually obvious in Figure 25B. In addition to preserving the size of the AuPd nanoparticles, then, the addition of Au allows the amount of Pd per particle to be minimized while still improving the selectivity to *p*-cymene. In the reductive environment required for the limonene reaction to proceed, the ability of the Au to minimize oxidation and the resultant mobility of the oxidized Pd formed does not directly factor into the outcome of the reaction, but its functionality in maintaining the size of the nanoparticles during pretreatment is likely a pivotal factor in rendering the bimetallic catalysts not only competitive but slightly better in terms of selectively catalyzing the reaction. Fundamentally, the robustness imparted to the AuPd alloy particles lets one vary the Pd composition to a certain degree, as we have done here, to maximize the performance of the catalyst while minimizing the Pd content.

Taken together, these results also inform a new understanding of the reaction pathway over Pd-containing catalysts. Previous work, as mentioned above, suggests that limonene conversion to *p*-cymene over silica-supported Pd catalysts proceeds via a two-step pathway, in which limonene is first fully hydrogenated to *p*-menthane before undergoing complete dehydrogenation to *p*-cymene, and terpene isomers of limonene are produced only in the absence of Pd or H_2.[4] The results gathered and presented here, on the other hand, suggest that both silica-supported Pd and AuPd alloy particles produce *p*-cymene through a two-step isomerization-dehydrogenation pathway, similar

to the mechanism reported for solution-phase Pd nanoparticles.[78] This conclusion is partially drawn from examining the product break-down of samples on which one would expect for there to be a limited number of multiatom sites: the 10% $AuPd/SiO_2$ sample and the PVP-stabilized Pd/SiO_2, for both of which (based on DRIFTS data and the growth of the Pd particles to a catalytically huge size, respectively) we expect there to be a lower number of sites upon which the catalyst reaction will take place. For the 10% $AuPd/SiO_2$ reaction in particular, the behavior observed in terms of selectivity is in good agreement with the assessment of the strength of the adsorbate-surface site bonds as measured by DRIFTS and XAFS, in that the Au-rich surface of this particle type coupled with the shift of electron density to the Pd surface atoms diminishes the particle's propensity to bind with adsorbates (both for oxygen, as discussed before, as well as the hydrogen and the limonene intermediates that figure into the reaction at the center of this discussion).

The mechanism derived for this reaction is also based upon the observation that a very low yield of *p*-cymene is produced when *p*-menthane is flowed over the catalyst bed as the reactant at 250 °C (Table 4). This result is surprising given that *p*-cymene is the thermodynamically favored product at this temperature.[78] If *p*-cymene were primarily produced via reversible dehydrogenation of *p*-menthane, one would expect to see a pattern in the TOFs of the catalysts that is similar to the yields of *p*-cymene displayed in Figure 25A. However, no correspondence between the TOFs in Table 4 and the selectivities to *p*-cymene shown in Figure 25A is observed.

It is also noted that the 10% AuPd catalyst possesses the highest TOF for p-menthane dehydrogenation. While all of the other supported Pd catalysts have p-menthane TOFs in the ~10-20- h^{-1} range, the TOF for this catalyst was calculated to be 160 h^{-1}. It has been previously reported that small islands of Pd deposited on Au

surfaces evolve hydrogen at higher rates than a Pd surface.[79] This enhancement could be attributed to surface diffusion of atomic hydrogen from Pd sites on the 10% AuPd particle surface, shown to be primarily single atom sites, to the sea of Au atoms that surround them. Because hydrogen binds much more weakly to inert Au than it does to Pd, associative desorption of from the surface once it spills over from Pd becomes a more facile process.[80] In the reaction described would facilitate the removal of hydrogen from limonene and reaction intermediates bound to the surface, as well as from menthane.

Table 4: Chemisorption results for each alloy catalyst as well as the percentage of *p*-menthane converted over each catalyst and the resultant calculated turnover frequency (TOF).[78]

Catalyst	CO adsorbed (μmol/g)	*p*-menthane conversion (%)	TOF (h^{-1})
10% AuPd	0.69 ± 0.1	1.42 ± 0.008	162.7 ± 17.8
20% AuPd	5.13 ± 0.6	1.39 ± 0.001	20.8 ± 2.4
28.5% AuPd	5.51 ± 0.7	1.32 ± 0.06	16.1 ± 2.0
Pd/SiO_2	0.77 ± 0.2	1.23 ± 0.001	7.6 ± 0.09
Pd/SiO_2 (i.e.)	27.1 ± 1.4	7.17 ± 0.2	21.3 ± 0.8
Pd/SiO_2 (iw)	15.7 ± 0.8	1.88 ± 0.09	9.7 ± 0.3

As such, the scheme in Figure 26 is proposed as the pathway of conversion from limonene to *p*-cymene, with *p*-menthane being as a byproduct rather than as an intermediate.

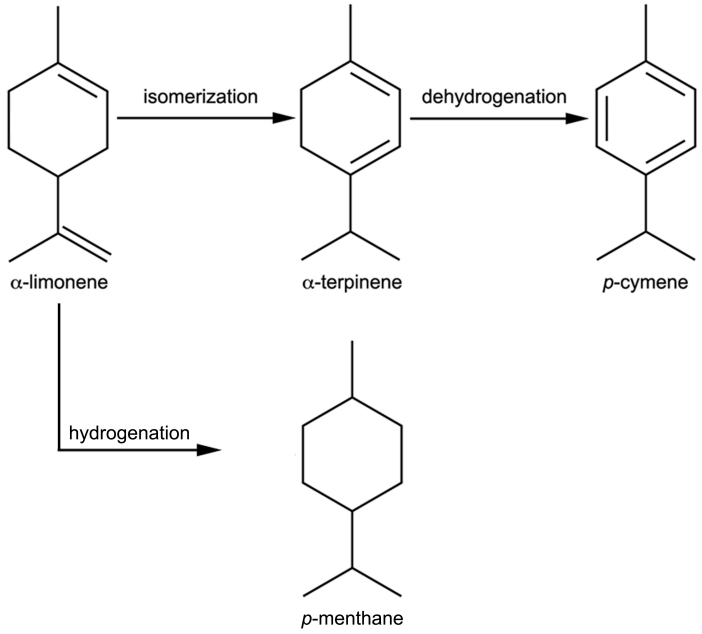

Figure 26: Proposed scheme for the conversion of α-limonene to *p*-cymene.

In sum, one of the most fundamental ways that Au affects the behavior when combined with Pd in nanoparticle made in a solution-phase process as described here is by preventing particle growth through sintering upon exposure to higher temperatures in an oxidative environment. On its own, Pd succumbs to oxidation quite rapidly under conditions that are necessary for calcination of solution-phase constructed nanoparticle catalysts. However, when Au is present in high enough quantities in a AuPd alloy, it is thermodynamically favored for Au to enrich the surface such that the surface composition of Au is higher than the overall bulk composition. This explains the tendency of the bimetallic particles to alloy when calcined as opposed growing and segregating. An investigation into the three types of particles synthesized demonstrates that the nominal percentage of Au present, and more specifically the effective alloy

composition near the shell surface, affects the ability of the Au present to prevent oxidation and to facilitate homogeneous alloying of itself with the Pd present. XAFS analysis of the catalysts indicates that there is a degree of intermixing at the Au-Pd interface in the core-shell particles, and for a shell as thick as up to 1.9 monolayers of Pd, we find that this is sufficient to impose an effective alloy composition close to the mole fraction cutoff for Au surface enrichment (near 0.40 Au for bulk AuPd alloys - see Figure 24). Once the shell reaches 3.8 monolayers, however, intermixing at the interface is not sufficient to prevent partial oxidation and subsequent partitioning of the Pd in the shell during the calcination step. Still, the particles also alloy, and their size distribution is, by and large, maintained. The preservation of size in the face of oxidative treatments is useful for keeping the catalyst particles in a catalytically relevant size range and makes them useful for improving upon the properties of monometallic solution-phase synthesized monometallic Pd/SiO_2 catalysts, as was demonstrated in the vapor-phase conversion of limonene to *p*-cymene.

4. Bimetallic Contribution 2: Subsurface Hydrogen Reserves in Pd@Au particles

Many metals are capable of forming metal hydride complexes through the interstitial inclusion and rearrangement of the solid metal when exposed to hydrogen. As such, these materials are the subject of investigation into their utility as hydrogen storage materials, the development of which would allow a hydrogen economy to come to fruition as a viable energy alternative to fossil fuel-based energy sources.[79] Palladium is in the class of metals that form a hydride phase, and in fact, hydrogen is more stable when it is present below the surface, or in the subsurface, of pure Pd than it is in its gaseous form.[126-128] The hydride phase of Pd has been extensively studied in the context of catalysis, since palladium materials are abundantly used in industrial processes involving hydrogen.[81] From decades of study, it is known that palladium hydride can not only form at low temperatures and low pressures of hydrogen on palladium surfaces, but also that hydride formation can occur on supported palladium particles with a relatively high dispersion.[82, 83] Furthermore, the tendency of palladium hydride to form is size dependent, decreasing with increasing dispersion of Pd.[82]

It is found that the 1.9 Pd@Au/SiO_2 catalyst seems to be unique in its capacity to harbor subsurface hydrogen, and the source of this phenomenon may be traced to a unique balance that exists for this catalyst that is present neither for the 0.7 nor the 3.8 Pd@Au/SiO_2 catalyst. According to Boudart *et al.*, the solubility of hydrogen in palladium is dependent on both the dispersion of the metal, as well as the amount of hydrogen that is chemisorbed to the surface.[130, 132, 133] As is seen through the quantitative fit analysis of XAFS data, the 0.7 Pd@Au particles do not possess a distinct submonolayer of Pd, but rather, Pd has to a degree alloyed with the Au core beneath, causing the surface to reconstruct into an alloy with a lower degree of Pd in the surface.

The 3.8 Pd@Au particles seem to alloy to a greater degree than the 1.9 Pd@Au particles after treatment in H_2 at 100 °C for 1 h. Pulsed CO chemisorption analysis of the three catalysts and the Pd controls show that the 1.9 Pd@Au/SiO_2 catalyst has a much higher dispersion than any of the others. TPR and TPHD data confirm the presence of subsurface hydrogen in the 1.9 Pd@Au catalyst exclusively, which disappears once the catalyst is reduced after calcination. Ethylene hydrogenation by bulk hydrogen has been found to occur successfully over metal surfaces where surface-adsorbed hydrogen exhibits no activity.[84] We compare the performance of the Pd@Au core-shell and AuPd alloy nanoparticles to one another in the hydrogenation of ethylene, and find evidence that subsurface hydrogen does factor into the catalysts' performance in this reaction. The catalyst results here demonstrate the utility of using Au to tune the ability of a bimetallic AuPd particle to hold a reserve of hydrogen that can promote a given reaction according to the requirements of the system in which they are employed.

4.1 Subsurface hydrogen reservoir formation in Pd@Au/SiO_2 as determined by TPR and TPHD

In Figure 23, the temperature-programmed reduction of the 0.7, 1.9, and 3.8 Pd@Au/SiO_2 catalysts, acquired after calcination at 300 °C, is shown. As discussed in Chapter 3, after being exposed to these conditions 3.8 Pd@Au/SiO_2 alone contains a significant amount of oxide, as evidenced by the large hydrogen uptake peak present on the TPR. The 1.9 Pd@Au/SiO_2 sample, on the other hand, exhibits a prominent that indicates there a release of hydrogen from the particle upon heating in a 5% H_2/Ar mixture. This is a direct indication that the 1.9 Pd@Au particles are capable of harboring subsurface hydrogen species. Palladium forms a β-hydride phase at temperatures at room temperature in H_2 pressures above two hundredths of an atmosphere.[85] The loss of this subsurface hydrogen has been found to occur simply by outgassing a sample

containing it at room temperature for a little more than 10 seconds[86]; thus, not only is easy to form this species of absorbed hydrogen, but it also remains readily available as a reservoir. In Figure 23, desorption for 1.9 Pd@Au/SiO_2 begins around t = 1.6 min, which corresponds to an initial release temperature of 39 °C. The shape of the peak corresponds with the H_2 desorption peak during the second cycle of TPR on carbon-supported Pd nanoparticles (Figure 27B), which shows hydrogen desorption to begin at 40 °C.[86] The second cycle TPR trends (TPHD) for both the 1.9 and 3.8 Pd@Au particles, shown in Figure 27A, also resemble this desorption peak. In fact, the behavior of 3.8 Pd@Au/SiO_2 during the first and second cycles of the TPR experiment represent exactly what was observed over the carbon-supported Pd catalyst studied by Nag, indicating that in the context of oxidation and hydrogen adsorption propensity, the highest Pd percentage catalyst behaves effectively like a Pd-only catalyst.[82]

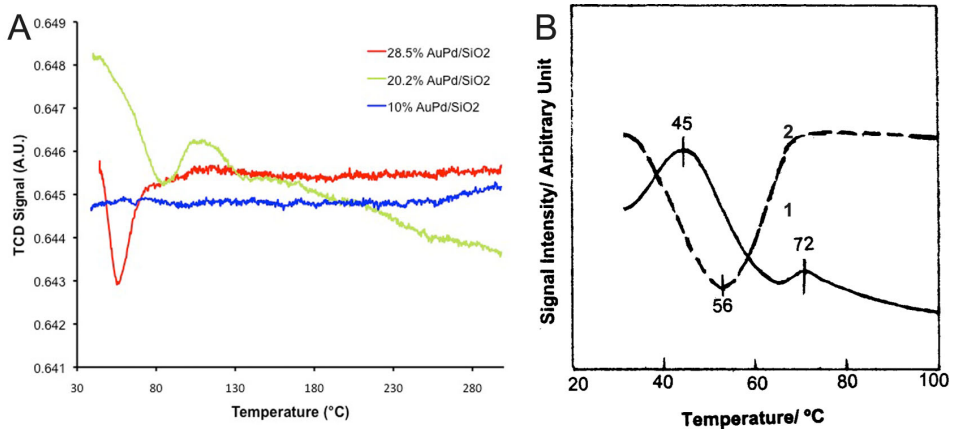

Figure 27: A) Second-cycle TPR, aka TPHD, of the AuPd samples after calcination. B) shows the first and second (1 and 2, respectively) cycles of TPR over a carbon-supported Pd catalyst.[82]

The 1.9 Pd@Au/SiO_2 catalyst desorbs H_2 at a slightly later time, indicating stronger retention of the hydride species. As this implies by the linear increase in temperature with time, there is variation in the desorption temperatures over each catalyst, and a slight offset in the temperature at which the maximum desorption occurs

compared to the Pd/C particles. Maximum desorption of H_2 from Pd/C occurs around 56 °C, while the maximum volume of H_2 is released at 81.8 °C and 83.5 °C for the first and second cycles of TPR over 1.9 Pd@Au/SiO_2. Conversely, the maximum release of hydrogen during the second cycle of TPR over 3.8 Pd@Au/SiO_2 occurs at 55.2 °C. This temperature is nearly identical to that observed for release from Pd/C, and so it may be assumed that the H_2 evolved from 3.8 Pd@Au/SiO_2 during TPHD was generated by the formation of a hydride phase during exposure to hydrogen during TPR and upon cooling. This conclusion is strengthened by the match in the hydrogen uptake peak character (Figure 23) for 3.8 Pd@Au/SiO_2 relative to the first cycle TPR of the Pd/C catalyst. The Pd present in this catalysts is most like pure Pd in its ability to form an oxide at ambient temperatures, and the existence of an oxide layer such as the one observed on 3.8 Pd@Au/SiO_2 (Figure 18) may passivate the particle surface against uptake of any hydrogen as a hydride.[82] This interpretation helps to explain why hydride may not form on this catalyst even though calcined 3.8 Pd@Au/SiO_2 shows a similar degree of Pd-Pd first shell coordination to 1.9 Pd@Au/SiO_2 (Table 5). Since oxide formation can influence subsurface hydrogen uptake, it follows that the distance of the AuPd interface from the surface is a major factor in subsurface hydrogen formation in this regard.

Unlike 3.8 Pd@Au/SiO_2 and Pd/C, 1.9 Pd@Au/SiO_2 consistently exhibits a hydrogen release around 80 °C, indicating that the interaction of H_2 with this catalyst is a stronger one than is found for pure Pd and that the increased stability of the subsurface hydrogen phase, the specific character of the phase aside, is facilitated by the presence of Au within the particle. The difference between the hydrogen holding behavior of 1.9 Pd@Au/SiO_2 and 3.8 Pd@Au/SiO_2 is strong evidence that the amount of

hydrogen stored in bimetallic particles can be tuned by adjusting the initial shell thickness of the particle.

This gets to a complex point of the hydride formation: 1.9 Pd@Au/SiO_2 forms a subsurface, hydrogen-containing phase that somehow survives high temperature exposure to oxygen and remains present once the particles have alloyed during the oxidative treatment. The existence of a unique phase is also particularly apparent when one tries to fit the Pd K edge XAFS data acquired for untreated 1.9 Pd@Au/SiO_2 with only Pd-Pd and Pd-Au contributions included in the fitting model; it is exceedingly difficult to do so, indicating the existence of a contribution that likely has to do with this phase observed by TPR. As such, it is worth considering the breadth of literature regarding bimetallic AuPd surfaces and their ability to trap hydrogen beyond adsorption to the surface.

A similar difficulty, for example, in capturing the behavior of Pd present in a shell on Au nanoparticles was encountered by Tang *et al*. in the context of attempting to accurately model the observed shifts in localized surface plasmon resonances of Au upon the uptake of hydrogen. In this case, the researchers concluded that it was possible that Au and Pd may have interdiffused to create an altered hydride-bearing chemical species within the nanoparticles studied.[82]

Using density functional theory, Kandoi *et al*. have calculated the binding energies of surface and subsurface hydrogen on a monolayer of Pd over a close-packed Au substrate.[81] In several capacities, this simulation is a good representation of the 1.9 Pd@Au/SiO_2 particle surface; specifically, the nanoparticles studied here are assumed to be faceted by Pd(111) pseudomorphically grown on Au, something observed for the Pd@Au particles through HAADF-STEM characterization (Figure 8) and numerically by XAFS quantitation of bond distances (Table 5). Moreover, like the simulated surface, the

1.9 Pd@Au particles have at least a full monolayer of Pd on the surface of the Au core. In their investigation, it was found that when Pd is layered on a noble metal such as Au, which has a fuller d-band than Pd, electron density is transferred to the emptier Pd overlayer, raising its d-band center closer to the Fermi level, and thus strengthening binding between Pd and H.[87] Additionally, the tensile strain imposed by depositing Pd on a material with a larger lattice parameter influences the electronic properties of adsorbate binding, such that they are bound more strongly to the Pd surface, although this is not the primary contributing factor to changes in nature of the Pd-adsorbate bond.[87] Overall, a combination of electronic effects and strain effects as described lead to an increase in the binding energy of surface hydrogen bound to Pd overlayers on a Au substrate; however, subsurface hydrogen was calculated to bind less strongly at the Au-Pd interface than it does below the surface in pure Pd (-1.87 eV versus -2.53 eV as calculated, respectively).[87] It may be that because there are almost two full monolayers comprising the Pd shell on the 1.9 Pd@Au/SiO_2 particles, the binding energy of subsurface hydrogen falls more closely in line with that of a pure Pd surface; however, this fails to explain how the hydrogen reservoir observed in 1.9 Pd@Au/SiO_2 survives calcination when Pd releases subsurface hydrogen under less harsh conditions.

The stabilization of surface hydrogen that is revealed by these calculations is useful, though, in that it informs our interpretation of the results of ethylene hydrogenation over the core-shell catalysts.[87] Although these results do not offer an explanation for the hydrogen retention of 1.9 Pd@Au/SiO_2, they do show that subsurface hydrogen also affects the d-band of the surface metal and therefore can directly influence the binding of surface hydrogen and ethylene.[87]

4.2 Quantitative Characterization of XAFS Analysis of the Pd@Au/SiO_2 Samples

XAFS analysis of the core-shell and the 28.5% (w/w) AuPd alloy samples after reduction to remove oxide contributions from the surface gives a more thorough overall idea of the average character of coordination environment around the Pd absorbing atoms, and this, helps to provide an explanation of the unique behavior of 1.9 Pd@Au/SiO_2 in harboring subsurface hydrogen. XAFS data was successfully fit for Pd@Au/SiO_2 catalysts after reduction at 100 °C in H_2 for 1h, as well as for the 3.8 Pd@Au/SiO_2 catalysts after calcination in air at 300 °C for 1h and subsequent reduction at the same temperature. The k-space and R-space data and their corresponding fits are shown in Figure 28 and Figure 29 , and Figure 30, as well as in Figure 22 in Chapter 3; the results of fitting of these data as well as Au absorber data are shown in Table 5 and Table 3.

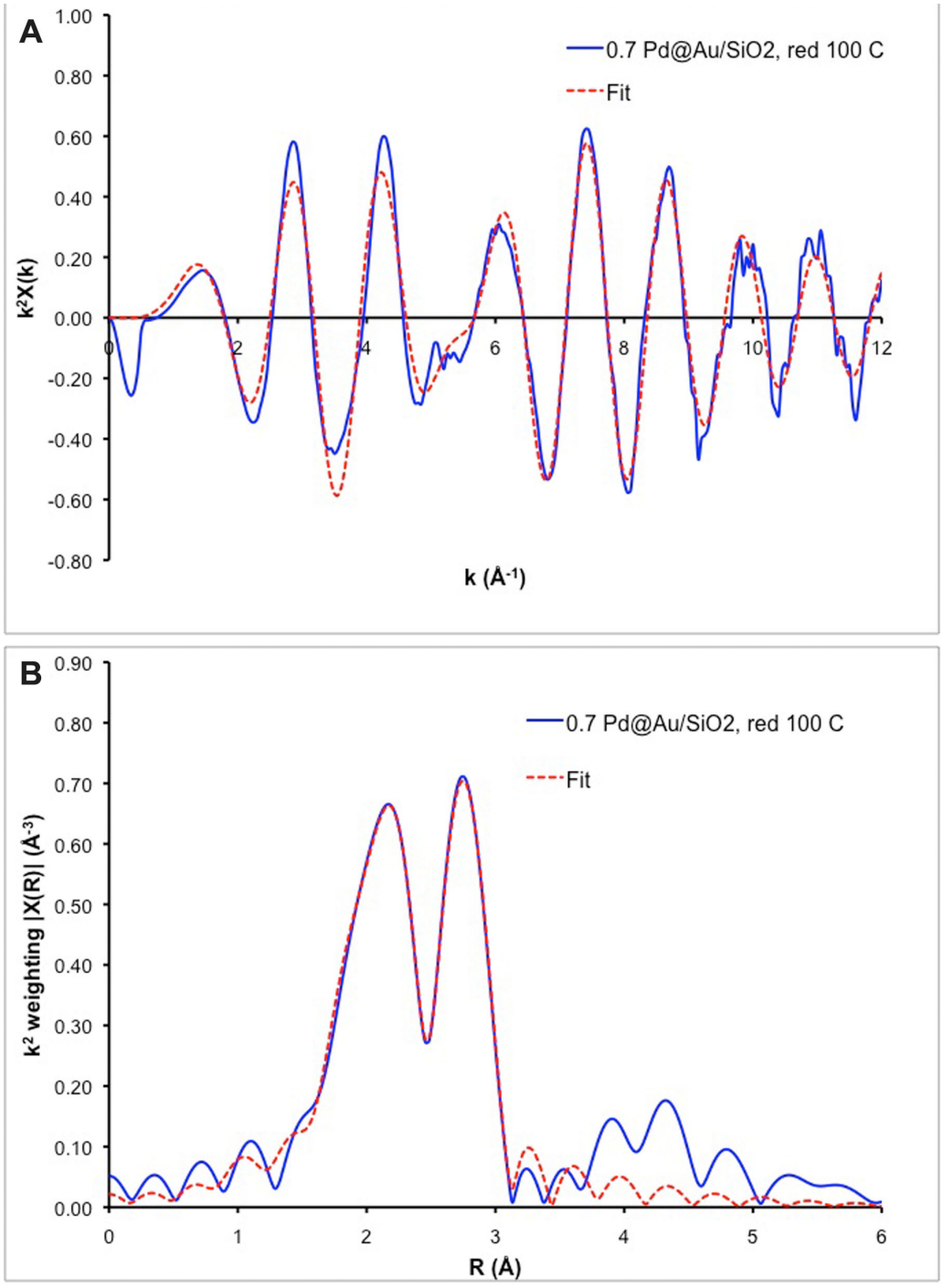

Figure 28: Pd K edge XAFS data (blue solid line) and calculated first-shell fit (red dashed) in *k* and *r* space for the 0.7 Pd@Au/SiO_2 catalyst after reduction at 100 °C for 1h (k-range = 2.5 - 11.2, R-range = 1.28 - 3.37).

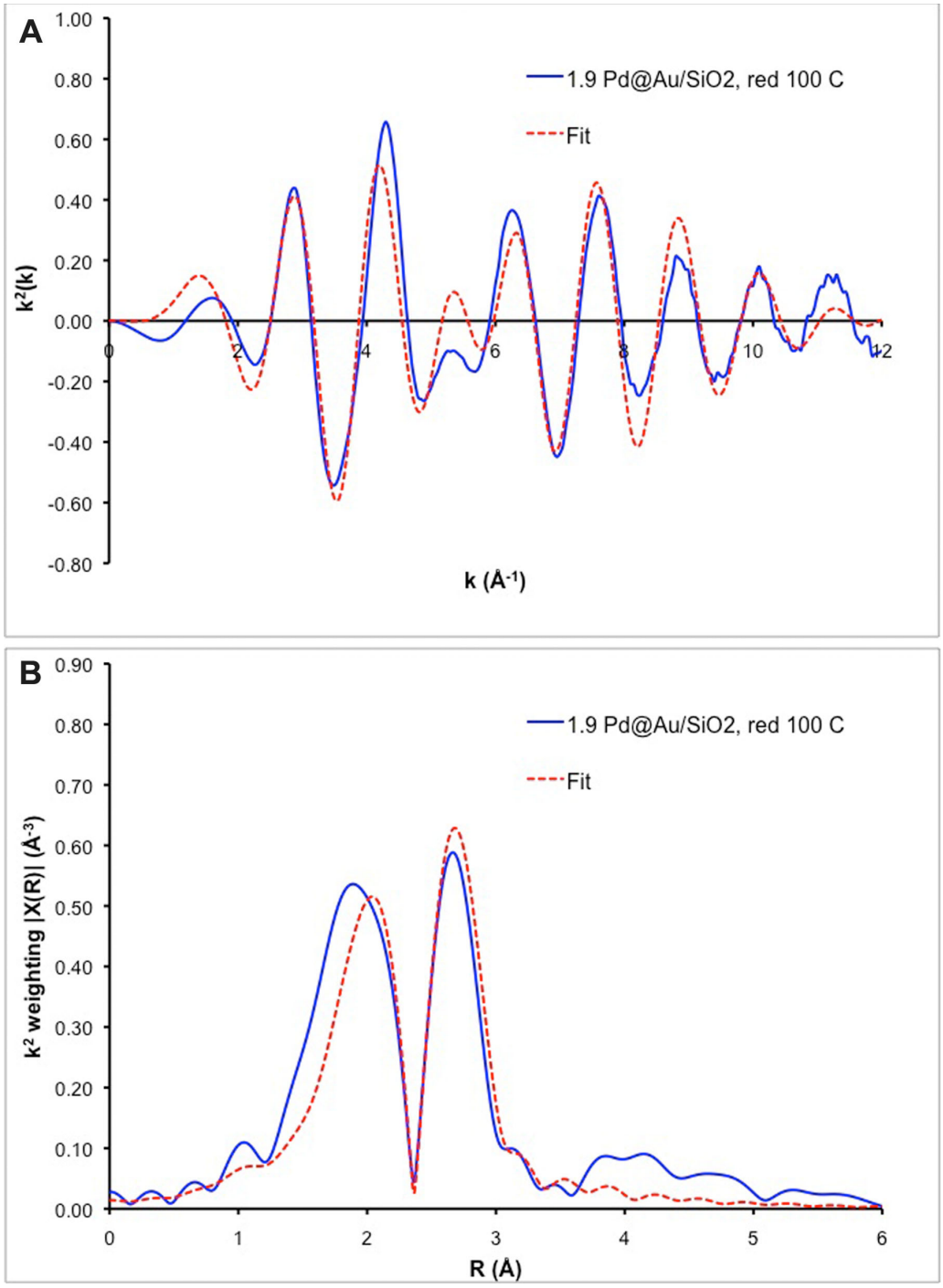

Figure 29: Pd K edge XAFS data (blue solid line) and calculated first-shell fit (red dashed) in *k* and *r* space for the 1.9 Pd@Au/SiO_2 catalyst after reduction at 100 °C for 1h (k-range = 2.5 - 11.5, R-range = 1.21 - 3.35).

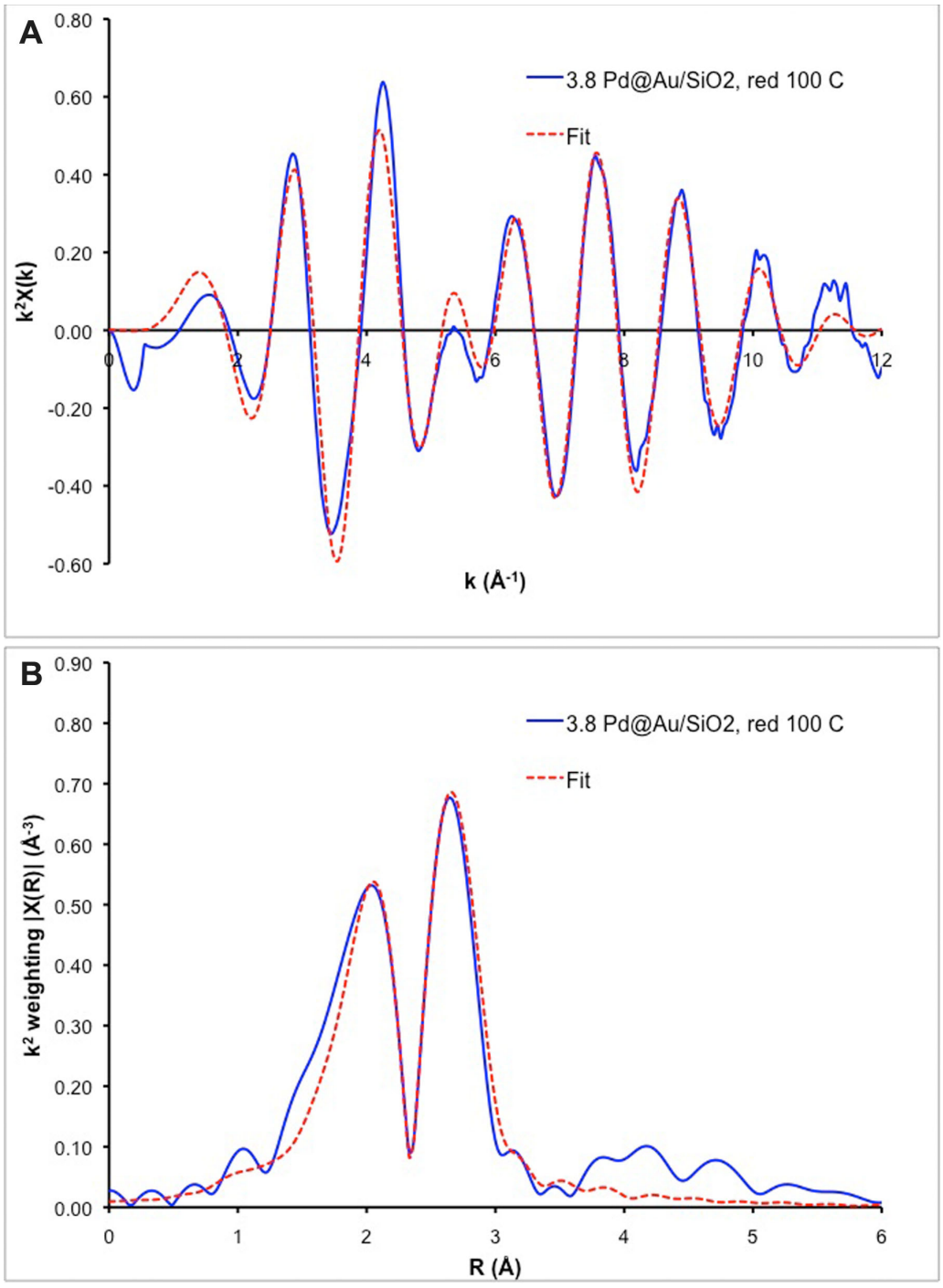

Figure 30: Pd K edge XAFS data (blue solid line) and calculated first-shell fit (red dashed) in *k* and *r* space for the 3.8 Pd@Au/SiO_2 catalyst after reduction at 100 °C for 1h (k-range = 2.5 - 11.5, R-range = 1.22 - 3.35).

The fits to the XAFS spectra acquired for the 0.7 Pd@Au/SiO_2 and 3.8 Pd@Au/SiO_2 catalysts agree very well with the experimental data in both k-space and R-space (given as the magnitude of the Fourier transform of the k-space data), as shown in Figure 28, Figure 30, and Figure 22 and as indicated by the R-factors given for the Pd absorber fits to each of these data sets in Table 5. The R-factor quantifies the misfit between the experimental data and its theoretical fit, and as a rule, factors below a magnitude of 0.05 indicate a "good" fit. The 1.9 Pd@Au/SiO_2 catalyst, however, proved extremely difficult to fit, as signified by the R-factor of the Pd-K edge fit, and is clearly visible in the mismatch of the dotted red and solid blue lines in both k-space and R-space in Figure 29. Moreover, the fit shown here, based on contributions from the Pd-Pd and Pd-Au scattering interactions, could not be improved upon by inclusion of a Pd-O contribution, assuming any oxide contribution would arise in the form of a Pd-O crystal structure. This is further illustrated in Figure 32, in which the imaginary component of the Fourier transformed fit in R-space have been broken down into their Pd-Pd and Pd-Au contributions for the 0.7 Pd@Au/SiO_2 and 1.9 Pd@Au/SiO_2 reduced samples, respectively. Where it is clear that for 0.7 Pd@Au/SiO_2 that the Pd and Au backscatterer contributions are sufficient to fully account for the features within the experimental data, the same contributions to the fit of the 1.9 data neglect to account for a feature occurring below 2 Å on the experimental R-space spectrum. This misfit is inherently amplified in the R-space magnitude plot, which is the summation of the real and imaginary parts of the Fourier transform of the k-space data.

It has been shown previously that palladium oxide formation on supported Pd particles leads to features on the XAFS R-space plot that fall below 2 Å.[87] This is inherently due to the shorter bond distance between Pd and O, and yet, consideration of a typical short Pd-O distance as a contributing factor to the fit is not sufficient to account

for the misfit in the 1.9 Pd@Au/SiO_2 experimental data. It is possible that if this feature does arise from an oxide based contribution, it could incorporate oxygen that is still a part of PVP residing on the surface of the particle, for which the bond distances would not be described by the theoretical PdO structure. However, one would expect a coordinative bond between PVP and Pd to be longer than where the missing contribution on the R-space data lies.

Studies by other researchers of palladium hydride formation using Pd edge XAFS revealed that the lattice of Pd expands from its typical value of 2.75 Å upon the formation of a hydride phase in supported particles.[88] All of the catalysts reported in Table 5, on the other hand, have a R_{Pd-Pd} of approximately 2.79 Å. Since the 1.9 Pd@Au/SiO_2 catalyst was not studied by XAFS after being exposed to calcination and calcination/reduction, it is not possible to speak to the changes in the Pd-Pd or heteroatomic bond distances as a function of treatment. However, since the Pd-Pd and heteroatom bonds are both effectively already expanded because of the presence of Au, it may be that the interstitial sites in the bimetallic samples are predisposed to absorption of hydrogen. It is observed that the heteroatomic and Pd-Pd bond distances in all of the catalysts are similar after reduction, indicating that this expansion is only one facet of the reason that 1.9 Pd@Au/SiO_2 alone seems to form a stable hydrogen reservoir. As already mentioned, the resistance to Pd oxide by this catalyst, something that does not extend to the 3.8 Pd@Au/SiO_2 sample, provides a viable reason that the expanded 1.9 Pd@Au subsurface sites are accessible to hydrogen while those within the 3.8 Pd@Au particles are not.

Looking into the numbers of Pd and Au backscatterers present in the first coordination shell of each catalyst gives an idea of the degree of alloying of the samples, as well as the homogeneity of the types of bonds between each absorber and

backscatterer. For the 0.7 Pd@Au/SiO_2 catalyst, the Pd absorber is surrounded by a total of 11.3 atoms on average, which, when one considers the overall coordination to be a weighted average of the coordination shells of the surface and bulk Pd atoms, matches the average coordination one would expect for a 5 nm particle, for which the dispersion is typically 20%. This high degree of coordination indicates that the Pd atoms within the 0.7 Pd@Au catalyst are not part of a separate Pd shell, but rather have migrated into the underlying Au core; a segregated shell of Pd on these particles would have a diminished average coordination sphere that was representative of the submonolayer amount of Pd on the core. Of the atoms in the first shell, approximately 10 of them are Au, further supporting the conclusion that Pd does not comprise a discrete layer on the particle surface. The Au coordination sphere is also comprised of 10.7 total atoms, 9 of which are Au backscatterers, which indicates that the Au core is intact. The fact that the intermetallic coordination numbers N are small but non-zero, taken with the overall retention of the Au core structure, signifies that Pd is present in an intermixed Pd-Au layer that is localized at the surface of the particle. The bond distances of all of the absorber-backscatterer interactions containing Pd are statistically equivalent to one another at 2.81 and 2.80 Å, while the Au-Au distance is 2.83 Å, again indicating the presence of two separate coordination environments for Au in the form of the Au core and a Pd-Au intermixed shell, with the shorted bond length arising from a favorable enthalpy of Au-Pd mixing. The Debye-Waller factors (σ^2) are also quite low for the interactions in the 0.7 Pd@Au particles aside from the Au-Pd interaction - this higher value likely derives from a larger distribution of types of Au-Pd bonds in the particles.

The 1.9 Pd@Au/SiO_2 results are more difficult to accurately interpret, because, as discussed above, Pd-Au and Pd-Pd contributions alone were not sufficient to fit the experimental data well. With these contributions only, we observe that the Debye-

Waller factors of the fit achieved for any of the absorber-backscatterer interactions that involve Pd are quite large relative to those for the other samples. The coordination numbers and NN distances, as in the other samples, suggest that the Au core is still present, and that at the core-shell interface, there is a certain degree of intermixing. However, the errors in the number of first shell backscatterers surrounding Pd are very large, another indication that the fit is not sufficient to fully describe the 1.9 Pd@Au/SiO_2 sample. In general, this data shows that of the three catalysts, the 1.9 Pd@Au/SiO_2 sample is unique in its composition and morphology. It should be noted that the Pd K edge 1.9 Pd@Au/SiO_2 XAFS data can be fit if the edge energies of the Pd-Pd and Pd-Au contributions are allowed to shift to a degree that generally points to an unreasonable fit ($|\Delta E^2| > 10$). In an investigation into the effect of Pd particle size on the existence of subsurface hydrogen using both experimental x-ray absorption near-edge spectroscopy (XANES) and XANES simulations, it was found that the presence of bulk hydrogen within the particles caused significant changes to the spectra, including a large edge shift.[44] Thus, the difficulty associated with achieving a good fit and small edge shifts for the 1.9 Pd@Au/SiO_2 sample may be an indication in itself that the sample contains bulk hydride.

It may be that the combination of the Pd layer thickness and the intermixing at the Au-Pd interface, observed from the XAFS fitting above, create a unique environment in the surface layers of the 1.9 Pd@Au/SiO_2 catalyst that drastically promotes hydrogen solubility. In a study on the thermodynamics of hydrogen inclusion at 1 atm within Pd-Au alloys of varying composition, the set of isotherms shown in Figure 31 was derived, and it was found that for a range of temperatures, the solubility of hydrogen within a structure increases significantly between Au compositions of 30 and 60%.[89] In other work, it was found that under the same H_2 pressure conditions AuPd alloys with a

molar composition of Au falling in between $\chi_{Au} = 0.15$ and 0.30 exhibit relatively constant H_2 solubilities even though the enthalpies and entropies of H_2 adsorption differ over this range because of their compensating effect when taken together.[90] The effective near surface alloy created by intermixing at the 1.9 Pd@Au core-shell interface is not as Au-rich as the alloy particle would be, as XAFS shows the shell to remain distinct from the particle core after heating at 100 °C in hydrogen, which could very well put the surface alloy composition within range of the promoted solubility regions seen on the isotherm at some point during pretreatment.

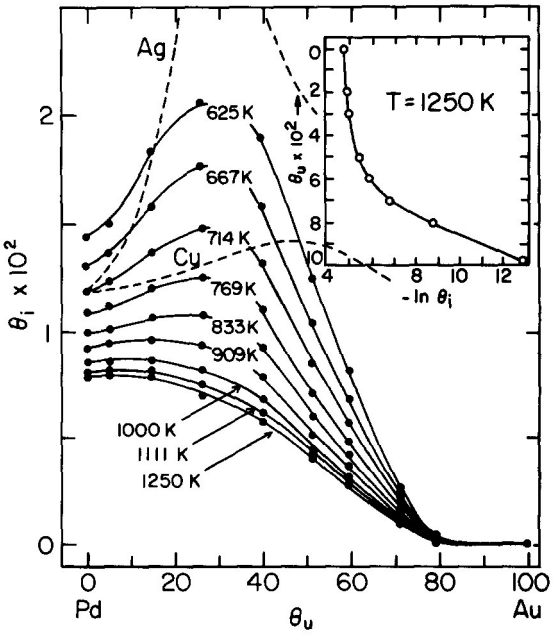

Figure 31: Hydrogen solubility isobars in Pd-Au-H ternary solid solutions.[89]

To summarize the XAFS analysis conducted on the 0.7, 1.9, and 3.8 Pd@Au/SiO_2 reduced at 100 °C and the 3.8 Pd@Au/SiO_2 catalyst after calcination and reduction at 300 °C, we do see intermixing in the shell layers to a certain extent after reduction at 100 °C but also that the core-shell morphology is retained in the particles. This is something

that has already been observed to affect the properties of the particles in limonene conversion and more generally in their propensity to prevent oxidation of Pd at higher temperatures. The 3.8 Pd@Au particles, when calcined and reduced, alloy by a different pathway than the partially alloyed Pd@Au samples that are observed after reduction at 100 °C, but we see that the particles both exhibit intermixing, and that the calcined and reduced alloy more fully than the sample reduced at low temperature. The 1.9 Pd@Au/SiO_2 sample, after reduction at 100 °C, is very difficult to fit, when the other catalysts relatively easy to fit after the same heat treatment. From Figure 20, we find that the analysis of reduced and as 1.9 Pd@Au/SiO_2 result in nearly identical XAFS data, and so we can infer that in both states there is an additional contributing factor to the structure. It is possible that PVP, which should still be present on the surface, may be introducing an oxygen contribution to the spectrum through interaction of its carbonyl functional group to Pd surface atoms. However, this does not seem to be a significant contributor to 3.8 Pd@Au/SiO_2 spectrum, which should bind PVP as well, although perhaps not as tenaciously as the 1.9 Pd@Au surface (for which electron density donation from Au affects Pd surface atom d-states to a greater degree).

Table 5: Pd K edge XAFS fitting parameters for Pd@Au/SiO_2 catalysts after exposure to different heat treatments. S_0^2 was set to 0.76 for fitting Pd absorber data, and to 0.88 for Au absorber data. [a]The coordination number of backscatterers surrounding the absorbing atom; [b]average bond distance between absorber and backscatterer; [c]Debye-Waller factor, [d]shift from the absorption edge to fit the data; [e]measure of the goodness of fit.

catalyst	treatment	absorber	backscatterer	N[a]	R[b]	σ^2 (10^{-3})[c]	ΔE^2 [d]	R-factor[e]
0.7 Pd@Au/SiO_2	H_2/100 °C	Pd	Pd	0.95 ± 0.5	2.80 ± 0.04	5.4 ± 4.5	-7.4 ± 4.4	0.00204
		Pd	Au	10.3 ± 1.0	2.80 ± 0.008	8.3 ± 1.4	-6.2 ± 0.8	
		Au	Pd	1.6 ± 0.7	2.81 ± 0.03	10.3 ± 3.5	4.0 ± 3.6	0.0072
		Au	Au	9.1 ± 0.9	2.83 ± 0.007	8.6 ± 0.7	5.0 ± 1.0	
1.9 Pd@Au/SiO_2	H_2/100 °C	Pd	Pd	4.5 ± 3.8	2.79 ± 0.04	13.3 ± 11.5	(-7)	0.07068
		Pd	Au	7.0 ± 4.3	2.77 ± 0.04	11.0 ± 7.5	(-6)	
		Au	Pd	1.4 ± 0.6	2.78 ± 0.03	10.6 ± 3.5	2.5 ± 4.0	0.00641
		Au	Au	9.8 ± 0.8	2.84 ± 0.005	8.7 ± 0.6	4.9 ± 0.9	
3.8 Pd@Au/SiO_2	H_2/100 °C	Pd	Pd	3.7 ± 1.2	2.79 ± 0.02	8.2 ± 3.7	(-7)	0.01747
		Pd	Au	6.7 ± 2.3	2.79 ± 0.01	9.6 ± 5.1	(-6)	
		Au	Pd	1.5 ± 0.5	2.77 ± 0.02	8.0 ± 2.2	3.5 ± 2.9	0.0092
		Au	Au	9.0 ± 0.8	2.84 ± 0.006	8.1 ± 0.6	4.9 ± 0.9	
3.8 Pd@Au/SiO_2	air/300 °C, H_2/300 °C	Pd	Pd	3.7 ± 0.6	2.80 ± 0.01	6.6 ± 1.6	-6.1 ± 1.3	0.00201
		Pd	Au	7.8 ± 0.9	2.79 ± 0.009	6.6 ± 1.4	-5.9 ± 1.0	
		Au	Pd	2.6 ± 0.5	2.81 ± 0.01	7.1 ± 1.4	4.8 ± 1.6	0.00742
		Au	Au	8.1 ± 0.8	2.83 ± 0.008	7.6 ± 0.7	4.8 ± 1.0	

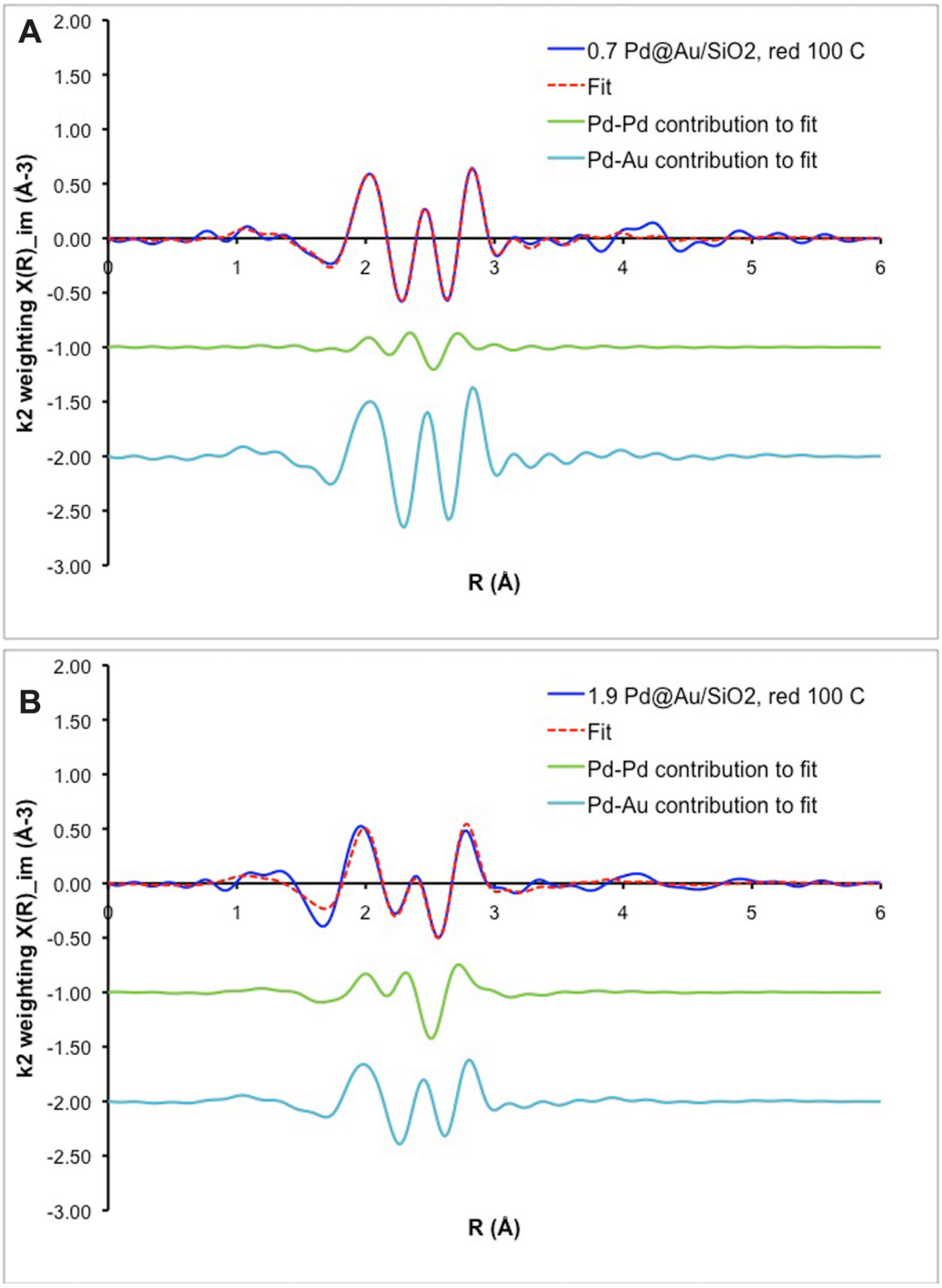

Figure 32: Comparison of the Pd (green) and Au (aqua) contributions to the overall fit (dashed red line) to the Pd K edge data collected for the A) 0.7 Pd@Au/SiO_2 catalyst and the B) 1.9 Pd@Au/SiO_2 catalyst, both after reduction at 100 °C for 1h.

4.3 Ethylene hydrogenation over Pd@Au/SiO_2 and AuPd/SiO_2 catalysts

Ethylene hydrogenation at room temperature offers the opportunity to not only test the catalytic properties of the core-shell Pd@Au particles against those of the alloy particles, but also to gauge the affect of the ability of the particles to absorb subsurface hydrogen on the rate of hydrogenation of an adsorbate. Ethylene hydrogenation catalyzed over platinum group metals is one of the most extensively studied reactions in the field of heterogeneous catalysis, and it is generally understood to be a structure insensitive process based on decades of single crystalline surface studies.[77] This terminology in itself is meant to denote that shape and size of, as well as the ordering of surface atoms on, a metal catalyst does not change the activity of the catalyst. However, recent studies have shown that supported Pd nanoparticles may behave differently than single crystal surfaces because of the presence of subsurface hydrogen stores that are closer to the surface of a nanoparticle than they are in bulk, therefore becoming accessible to adsorbing alkenes.[91] More recent studies have also demonstrated that the addition of a second metal, such as Ag, to Pd, can modulate its selectivity in alkene hydrogenation.[91] To the best of our knowledge, the data presented here represents the first instance in which a series of AuPd bimetallic catalysts has been employed in ethylene hydrogenation to ethane.

Initially, it was found that the bimetallic and alloy catalysts, at the per particle concentration discussed in the experimental descriptions, were all extremely active in the conversion of ethylene to ethane such that the conversion at the ethylene flow rate used was observed to be 100%. Full conversion, somewhat counter intuitively, poses a problem in determining the TOF of a catalyst, in that when a reactant is fully converted over a catalyst bed, it is uncertain what fraction of the catalyst bed is necessary to achieve full conversion of the amount of reactant flowing through the reactor at a given

moment. Likely, only a fraction of the bed has catalyzed the complete conversion, and as such, turnover frequency calculations based on the full amount of catalyst loaded into the reactor will underestimate the activity of surface sites on that catalyst. Even at higher partial conversions, TOFs calculated will be inaccurate, since the amount of starting material passing through the catalyst bed greatly diminishes as it makes its along the height of the bed; effectively, the TOF determined is an average over a range of starting concentrations of reactant in the flow, with the catalyst closer to the bottom of the reactor contributing less to the overall conversion than is assumed. For this reason, the construction of the bimetallic catalysts was modified so that the concentrations of particles on the silica support were diluted by 500, 250, and 15 fold for the 3.8, 1.9, and 0.7 Pd@Au/SiO_2 catalysts, respectively. The dilution was achieved by increasing the ratio of silica per volume of nanoparticle solution during catalyst preparation, such that the particles were evenly dispersed over the support material. The monometallic catalysts were both diluted 50x for comparison, expecting that diluting the Pd-only catalyst would do little to diminish its activity, and that diluting the Au catalyst would likely not make much difference, as Au is not active for ethylene hydrogenation. For each run, the mass of diluted catalyst loaded into the reactor was approximately 0.110 g, and ethylene and H_2, diluted in He, were flowed in at a rate of 235 mL/min at a concentration of 15% (v/v) and a C_2H_4:H_2 ratio of 1:6 over the course of several hours.

Table 6 is a summary of the rates of ethylene conversion to ethane per minute per gram of catalyst used. These rates are shown principally to reveal the basis for the TOF calculations given in Table 5, for which the rate of conversion has been normalized to the number of Pd active surface sites per gram as calculated by two methods: from the theoretical structure of each type of particle and as determined from pulsed CO chemisorption analysis. For the geometry-based calculations, the particles were

assumed to have a spherical shape, and the average surface area of each type of particle was determined by calculating surface area for every particle diameter measured in the determination of size distribution (Figure 9). Each Pd atom (or Au in the case of the monometallic Au/SiO_2 catalyst) was assumed to be a circle with a diameter equal to the homonuclear bond length, and these were assumed to close-pack on the surface of the nanoparticle with a packing factor of 0.9069.[92] In both cases, it was assumed that the average Pd atom:active surface site ratio was 1.5. This takes into account, as seen experimentally in DRIFTS (Figure 16) as well as CO chemisorption analysis, that Pd active sites are comprised both of single and multiatom Pd ensembles to which adsorbates can bind.[93]

Table 6: Rates of ethylene hydrogenation as the amount of ethylene converted per minute per grams of catalyst over diluted $Pd@Au/SiO_2$ catalysts. [a]Catalyst conversion over Pd was 100%and so error could not be calculated.

		Rate (mmol ethylene converted/min/g catalyst)		
Sample	Particle dilution factor	As is	Reduced, 100 °C	Calcined and reduced, 300 °C
3.8 $Pd@Au/SiO_2$	500	50 ± 5	38 ± 7	13 ± 0.3
1.9 $Pd@Au/SiO_2$	250	57 ± 0.7	59.5 ± 6	2.6 ± 0.2
0.7 $Pd@Au/SiO_2$	15	5.2 ± 0.5	1.6 ± 0.03	0.5 ± 0.1
Au/SiO_2	50	0.5 ± 0.03	0.9 ± 0.6	0.9 ± 0.1
Pd/SiO_2	50	7.9 ± 1.0	59 ± 3	97.1[a]

From the values in Table 6, it is shown that except for the Pd/SiO_2, all of the catalysts that contain Pd and are therefore expected to catalyze ethylene hydrogenation exhibit a drop in rate after calcination and reduction. This is likely due to the rearrangement of surface sites that occurs upon alloying under heat treatment. For the Pd/SiO_2 catalyst, the rates are much higher than for any of the other catalysts, and in fact reach 100% after calcination and reduction, such that the accurate determination of TOF for this particular

sample is not possible. However, the results presented for pure Pd represent the lower limit of the conversion rate over the monometallic catalyst, and so it can be concluded that it catalyzes the hydrogenation much better than the bimetallic catalysts.

Turnover frequencies (TOFs) displayed in Table 7 show that the 1.9 Pd@Au/SiO_2 either performs just as well as or even better than the other Pd@Au catalysts prior to exposure to calcination. In the "as is" state, the 1.9 Pd@Au/SiO_2 and the 3.8 Pd@Au/SiO_2 both yielded similar TOFs , with that of 1.9 Pd@Au/SiO_2 being slightly higher, and both are several times larger than the TOF over as is 0.7 Pd@Au/SiO_2. Once the catalysts have been exposed to hydrogen at 100 °C, an interesting phenomenon is observed relative to the as is data for the TOFs that have been calculated using the geometry-derived active site densities: the catalytic activity of the 0.7 Pd@Au/SiO_2 and 3.8 Pd@Au/SiO_2catalysts both drop off, while that of 1.9 Pd@Au/SiO_2 persists. The TOFs calculated using CO chemisorption show the same relative trend in the conversions over the three catalysts, with 1.9 Pd@Au/SiO_2 yielding ethane at a rate approximately 1.3 times faster than over 3.8 Pd@Au/SiO_2, and approximately 10 times faster than the 0.7 Pd@Au/SiO_2 catalyst produces ethane. The uniform factor of three increase in the TOFs calculated with the experimental chemisorption could have to do with a loss of surface sites due to PVP association with the particle surface, something that was not accounted for in calculating the number of sites per gram of catalyst using geometry. Given that the observed increase in TOF is uniform over all three catalysts, it may not be unreasonable to use this as a gauge of the percentage of the surface blocked by PVP that remains on the surface after treatment at 100 °C; the observed increase would indicate that PVP blocks two-thirds of the surface sites on each catalyst. This could also be an indication that ethylene, the limiting reactant, only occupies one-third of the surface sites on the particles, and that ethylene hydrogenation proceeds by a

Langmuir-Hinshelwood mechanism. This is in keeping with the accepted literature description of the hydrogenation of ethylene on solid catalysts, known as the Horiuti-Polyani mechanism.[9, 142]

Table 7: TOF of ethylene hydrogenation over Pd@Au/SiO_2 catalysts as based on surface active site determination through geometry-based surface site calculation and pulsed CO chemisorption analysis. Dashes indicate that the chemisorption of CO on the surface of the catalyst was recorded as zero. [a] The TOFs for Pd/SiO_2 are not accurate due to the high conversion of C_2H_4. [b]Chemisorption data was not acquired for this sample.

	TOF ($\times 10^3$ molecules ethylene/min/Pd active site)				
	Based on calculated surface area			Based on pulsed CO chemisorption	
Sample	As is	Reduced, 100 °C	Calcined and reduced, 300 °C	Reduced, 100 °C	Calcined and reduced, 300 °C
3.8 Pd@Au/SiO_2	1.4 ± 0.5	1.1 ± 0.4	1.1 ± 0.4	2.9 ± 0.5	1.05 ± 0.03
1.9 Pd@Au/SiO_2	1.8 ± 0.5	1.9 ± 0.5	0.4 ± 0.1	3.7 ±0.4	0.36 ± 0.03
0.7 Pd@Au/SiO_2	0.22 ± 0.05	0.10 ± 0.03	0.20 ± 0.06	0.331 ± 0.006	0.36 ± 0.07
Au/SiO_2	0.023 ± 0.007	0.04 ± 0.03	0.04 ± 0.01	-	-
Pd/SiO_2	2.1 ± 0.7	15.8 ± 4.5	21	1.99 ± 0.09	- [a]

Once the catalysts have been calcined and reduced at 300 °C, the trends observed in conversion change markedly. When normalized using geometry, the TOF of the 3.8 Pd@Au/SiO_2 catalyst remains the same as found after reduction at 100 °C, as does the 0.7 Pd@Au/SiO_2, but the 1.9 Pd@Au/SiO_2 conversion drops precipitously, to a frequency that is nearly 5 times lower than when simply reduced at 100 °C. The constancy in conversion over 3.8 Pd@Au/SiO_2 is consistent with findings regarding XAFS analysis of this catalyst, in that this particle type has already undergone transformation to its quasi-alloyed form upon exposure at 100 °C, something that can be attributed to the diminished efficacy of Au to thermodynamically partition to the surface and prevent partitioning and oxidation of Pd when it is located further away from the particle surface initially. The TOFs calculated for the calcined and reduced catalysts

using chemisorption are very similar to those derived from geometry. The largest change is seen the Pd@Au/SiO_2 catalysts after reduction at 100 °C, for which there is a three-fold increase difference in TOF when comparing geometry-based to CO chemisorption derived values (as discussed above). The monometallic Pd/SiO_2, after calcination and reduction, converts ethylene completely to ethane, and in fact, as expected, under all conditions converted ethane at sufficiently high conversion rates that the calculated TOFs should not be taken as accurate.

The reason for the change in the trends in TOF upon conversion to the alloy morphology may have to do with the mechanism by which ethylene binds to a Pd-Au surface. Upon studying the effect of alloy composition on AuPd surfaces, it was found that the presence of Au in a Pd surface as an alloy tends to weaken binding of the ethylene and hydrogen to the surface of the catalyst, and that the effect is composition dependent, such that fractional surface coverages of Au higher than 0.7 lead exclusively to π-bonded ethylene adsorbed to the surface, the weaker of two configurations by which ethylene binds to a surface (the other being a σ-bound ethylidene species).[94] The weaklier that ethylene and hydrogen bind to a surface, the more likely that it will form ethane. Furthermore, the presence of σ-bound ethylidene on the surface can suppress the adsorption of the more easily formed π-bound ethylene intermediate.[95, 96] This would indicate that the alloying that occurs within the Pd@Au particles upon calcination and reduction, and which enriches the particle surface with Au, facilitates the formation of the less tightly bound ethylene intermediate.

Interestingly, computational studies on ethylene hydrogenation show that the inclusion of Au on a surface of a 19-atom Pd cluster does not appreciably change the catalytic properties of the cluster with respect to a Pd-only control, mainly because the weakened metal-adsorbate bonds that enhance the catalytic rate are effectively canceled

out by the diminished number of hydrogen adsorption sites on the catalyst diluted at the surface by Au.[97] The fact the TOFs for the Pd@Au catalysts vary with composition, then, serves to suggest again that subsurface hydrogen plays a role in the structure sensitivity of the reaction over these catalysts. Previous work has shown that the degree of subsurface hydrogen formed within silica-supported Pd nanoparticles is highly size dependent, and will not form in particles smaller than 2.6 nm but which increases upon an increase in size and corresponding decrease in particle dispersion.[95]

However, the 1.9 Pd@Au/SiO_2 catalyst's ability to catalyze the efficient seems to correlate directly with the presence of hydrogen absorbed in its bulk. While in the core-shell form, the catalyst possesses a resistance to a loss in activity, only behaving like the 0.7 Pd@Au/SiO_2 catalyst after being subjected to calcination and reduction. As is seen from the treatment carried out during TPR analysis of the 1.9 Pd@Au/SiO_2 catalyst, reduction at high temperatures of the catalyst at temperatures higher than 80 °C in a reducing atmosphere post-alloying triggers a release of this reserve, so that we would expect subsurface hydrogen reserves to not be present in the calcined/reduced alloy catalyst form of 1.9 Pd@Au/SiO_2.

It is possible that the core-shell structure of the particles is necessary for the absorption of hydrogen into its bulk. Work supporting this hypothesis was presented by Yamauchi *et al*., who studied the formation of subsurface hydrogen in Pd_{core}-Pt_{shell} nanoparticles.[138, 147] In their work, the authors found that over a range of pressures from fractions of an atmosphere to 1 atm, hydrogen absorbed into PdPt bimetallic particles does not cause lattice expansion in the way it does when absorbed into Pd only particles, an indication of hydrogen interpolation in the Pd lattice as a hydride phase.[98] Rather, they found through NMR analysis that hydrogen was dispersed throughout both metals and was concentrated at the interfacial region of the core-shell particles, concluding that

the bimetallic intermixed region of the particle provides an energetically favorable area for bimetallic hydride to form. While EXAFS showed AuPd intermixing to occur in all of the Pd@Au catalysts, the 1.9 Pd@Au/SiO_2 is unique in that the intermixed region is present near the surface, which is not oxidized, as in the 3.8 Pd@Au catalyst (which passivates the surface to the formation of a hydride) and is almost fully Pd, unlike in the 0.7 Pd@Au particles.

Studying the ethylene hydrogenation behavior of the Pd@Au/SiO_2 catalysts and comparing them against their alloy counterparts gives us a reaction platform for studying both how the inclusion of Au affect the outcome of the hydrogenation reaction and how the particular arrangement of Au and Pd within the structure of the particles contribute to the variation in catalyst performance, in the context of ability of the particles to hold hydrogen reserves within their bulk. We find that both the amount and relative location of Au within the particles affects the TOF observed for the catalysts, revealing a composition-based structure sensitivity element to ethylene hydrogenation. XAFS and TPR analyses of the catalysts aid in our understanding of how the changes in morphology of the AuPd particles affect the conversion of ethylene to ethane, and both highlight the fact that of the three bimetallic catalysts, the 1.9 Pd@Au/SiO_2 alone creates a unique chemical environment in which subsurface hydrogen is especially prone to form.

5. Future Directions

The results above show that the Pd@Au model catalysts synthesized here have uniform, distinct core-shell structures that can be changed into alloyed particles by heat-treating them. The shell thickness is a principal determining factor in the transformation. As the distance grows, the Pd shell becomes more apt to behave as pure Pd does under higher temperature conditions in the presence of oxygen; that is, it is more likely to oxidize and migrate on the surface of the particle. This is the behavior observed of the 3.8 Pd@Au/SiO_2 under calcination conditions, although the presence of Au still maintains the particle size under conditions in which pure Pd particles exhibit significant sintering. It was also found that by tuning the amount of Pd deposited on the surface of the Au core during synthesis, the propensity of the particle to absorb hydrogen within its bulk can be altered dramatically. For the 1.9 Pd@Au/SiO_2 catalyst in particular, a combination of slight intermixing at the interface of the core-shell interface and the nearness of that region to the surface of the particle is thought to render the particle exceptionally amenable to hydrogen absorption. Both of the observed outcomes of Au-Pd interactions discussed in this work can be and are explained as a combination of fundamental electronic and geometric influences, but can also be directly correlated to the particle behavior in the two reactions studied here. Since particle size retention and the absorption of hydrogen are broadly relevant to industrial catalysis, and so are useful parameters by which to construct a structure-based understanding of performance of bimetallic particles. To continue developing our understanding of the behavior of bimetallic catalysts in this practical way, there are two areas of further inquiry: (1) investigation of other observable effects of Au-Pd particles, such as resistance to CO poisoning or spillover effects for improved ease of adsorbate

desorption, and (2) the behavior of other two-metal systems, ideally still containing Pd and investigating the same reactions. We have continued working in the first direction, by using the well-characterized catalysts described here to probe their utility for other conferring desirable alterations to catalyst behavior, specifically, heightened resistance to CO poisoning of the catalyst surface.

5.1 Selective solution-phase formic acid decomposition to carbon dioxide

Studying the formic acid dehydrogenation reaction incorporates investigations into both the selectivities and activities of the AuPd catalysts in a solution-phase reaction, something that has not yet been investigated with the series of catalysts described here. Formic acid (HCOOH) decomposes via a two pathway process that can result in either the formation of H_2 and CO_2 or, alternatively, in the production of H_2O and CO. The latter of these two pathways is an undesired one, in large part because CO is a catalyst poison, causing the deactivation of surface sites over time and therefore reducing catalyst activity. From an application-based perspective, the development of a high efficiency way to release H_2 from formic acid renders this reaction into a viable chemical storage mechanism for H_2-based energy applications.[48, 98]

Generally, it has been shown that HCOOH dehydrogenation can be carried out over bimetallic catalysts such as AgPd and AuPd, but that the reaction temperatures required to achieve appreciable TOFs, nearing 100 °C, also cause a significant amount of dehydration to occur.[99] Improving the monodispersity of the constituent nanoparticles, however, enhanced TOF to 230 h^{-1} over AuPd alloy catalysts at 50 °C.[21] This reaction, then offers a way to simultaneously employ our particles in a reaction where tuning of the AuPd alloy composition in a controlled way may lead to useful improvements in the

catalytic activity of formic acid dehydrogenation while giving us a platform to compare the ability of the catalysts to resist poisoning by CO.

5.1.1 Selective dehydrogenation over AuPd catalysts at room temperature

In experiments currently being carried out in the laboratory, the Pd@Au/SiO_2 catalysts in their as is state and the corresponding alloys generated by calcination are being utilized in a straightforward solution-phase reactor setup based on the experimental design reported by Metin *et al*.[21] In the reaction, 180 mg of catalyst powder and DI H_2O are mixed, and the reaction vessel is connected to a gas burette to monitor the output of gaseous products from the flask upon the injection of formic acid. In order to determine the selectivity of the product distribution to carbon dioxide and hydrogen gas evolution, as opposed to carbon monoxide and water formation, a second set of experiments were performed using concentrated sodium hydroxide (10 M) to fill the gas burette. When the evolved gas passes through this trap, carbon dioxide is selectively dissolved into the NaOH solution such that comparing the initial rates of gas evolution for the same catalyst with and without the trap present speaks to the exclusivity of hydrogen evolution over carbon monoxide production.[21]

The resistance to CO poisoning can and will be measured in two ways. The first method is by comparing the ratio of volumes of gas evolved with and without a NaOH trap present in the experimental setup to the overall initial rate of gas production without a trap. If the rate is very large, for example, but doesn't diminish appreciably upon the introduction of the NaOH trap, it can be concluded that the particle is principally producing CO and H_2O but that CO is not hindering the turnover of molecules at the catalyst surface. Conversely, if the rate is low and the inclusion of the

NaOH trap does not change the rate, it can be inferred that CO production is prevalent and that it is affecting the rate.

To corroborate any conclusions arrived at through comparison of the NaOH trap results with those rates recorded without it, one can also poison the catalyst by passing CO over the powder catalyst prior to its introduction to the reaction. In this way, additionally, the CO poisoning resistance of catalysts that do selectively dehydrogenate HCOOH, and therefore do not produce any CO, which might poison the surface, can be tested.

Experimental results so far show that there is a marked difference in the catalyst performance depending on whether the particles possess core-shell or alloyed morphologies. For example, the 1.9 Pd@Au/SiO_2 catalyst, after transformation to the 20.2%AuPd/SiO_2 alloy catalyst, exhibits a 14-fold increase in initial gas evolution rate as measured before normalization to active surface site concentration. Continuing work will focus on testing the repeatability of formic acid decomposition, and the utilization of NaOH trap experiments as well as GC analysis to determine the selectivity to catalyzed dehydrogenation over dehydration. Additionally, the deliberate CO poisoning experiment, as described above, will be carried out.

References

1. Bartholomew, C. H. F., R.J., *Fundamentals of Industrial Catalytic Processes*. Second ed.; John Wiley and Sons: Hoboken, New Jersey, 2006.

2. Balcha, T.; Strobl, J. R.; Fowler, C.; Dash, P.; Scott, R. W. J. Selective Aerobic Oxidation of Crotyl Alcohol Using AuPd Core-Shell Nanoparticles. *ACS Catalysis* **2011,** *1*, 425-436.

3. Kesavan, L.; Tiruvalam, R.; Rahim, M. H. A.; bin Saiman, M. I.; Enache, D. I.; Jenkins, R. L.; Dimitratos, N.; Lopez-Sanchez, J. A.; Taylor, S. H.; Knight, D. W.; Kiely, C. J.; Hutchings, G. J. Solvent-Free Oxidation of Primary Carbon-Hydrogen Bonds in Toluene Using Au-Pd Alloy Nanoparticles. *Science* **2011,** *331*, 195-199.

4. Wilson, A. R.; Sun, K.; Chi, M.; White, R. M.; LeBeau, J. M.; Lamb, H. H.; Wiley, B. J. From Core-Shell to Alloys: The Preparation and Characterization of Solution-Synthesized AuPd Nanoparticle Catalysts. *The Journal of Physical Chemistry C* **2013,** *117*, 17557-17566.

5. Somorjai, G. A.; Li, Y., *Introduction to surface chemistry and catalysis*. John Wiley & Sons: 2010.

6. Gajewicz, A.; Puzyn, T.; Rasulev, B.; Leszczynska, D.; Leszczynski, J. Metal oxide nanoparticles: size-dependence of quantum-mechanical properties. *Nanoscience & Nanotechnology-Asia* **2011,** *1*, 53-58.

7. Daniel, M.-C.; Astruc, D. Gold nanoparticles: assembly, supramolecular chemistry, quantum-size-related properties, and applications toward biology, catalysis, and nanotechnology. *Chemical reviews* **2004,** *104*, 293-346.

8. Pawelec, B.; Venezia, A. M.; La Parola, V.; Cano-Serrano, E.; Campos-Martin, J. M.; Fierro, J. L. G. AuPd alloy formation in Au-Pd/Al2O3 catalysts and its role on aromatics hydrogenation. *Applied Surface Science* **2005,** *242*, 380 - 391.

9. Ghampson, I. T.; Newman, C.; Kong, L.; Pier, E.; Hurley, K. D.; Pollock, R. A.; Walsh, B. R.; Goundie, B.; Wright, J.; Wheeler, M. C.; Meulenberg, R. W.; DeSisto, W. J.; Frederick, B. G.; Austin, R. N. Effects of pore diameter on particle size, phase, and turnover frequency in mesoporous silica supported cobalt Fischer-Tropsch catalysts. *Journal of Catalysis* **2010,** *388*, 57 - 67.

10. Grass, M. E.; Joo, S. H.; Zhang, Y.; Somorjai, G. A. Colloidally Synthesized Monodisperse Rh Nanoparticles Supported on SBA-15 for Size- and Pretreatment-Dependent Studies of CO Oxidation. *The Journal of Physical Chemistry C* **2009,** *113*, 8616-8623.

11. Meenakshisundaram, S.; Nowicka, E.; Miedziak, P. J.; Brett, G. L.; Jenkins, R. L.; Dimitratos, N.; Taylor, S. H.; Knight, D. W.; Bethell, D.; Hutchings, G. J. Oxidation of alcohols using supported gold and gold-palladium nanoparticles. *Faraday Discussions* **2010,** *145*, 341- 356.

12. Lopez-Sanchez, J. A.; Dimitratos, N.; Miedziak, P.; Ntainjua, E.; Edwards, J. K.; Morgan, D.; Carley, A. F.; Tiruvalam, R.; Kiely, C. J.; Hutchings, G. J. Au-Pd supported nanocrystals prepared by a sol immobilisation technique as catalysts for selective chemical synthesis. *Physical Chemistry Chemical Physics* **2008,** *10*, 1921-1930.

13. Hong, J. W.; Kim, D.; Lee, Y. W.; Kim, M.; Kang, S. W.; Han, S. W. Atomic-Distribution-Dependent Electrocatalytic Activity of Au–Pd Bimetallic Nanocrystals. *Angewandte Chemie International Edition* **2011,** *50*, 8876-8880.

14. Lee, Y. W.; Kim, N. H.; Lee, K. Y.; Kwon, K.; Kim, M.; Han, S. W. Synthesis and Characterization of Flower-Shaped Porous Au-Pd Alloy Nanoparticles. *The Journal of Physical Chemistry C* **2008,** *112*, 6717-6722.

15. Tian, N.; Zhou, Z.-Y.; Sun, S.-G.; Ding, Y.; Wang, Z. L. Synthesis of Tetrahexahedral Platinum Nanocrystals with High-Index Facets and High Electro-Oxidation Activity. *Science* **2007,** *316*, 732-735.

16. Zhang, G.-R.; Xu, B.-Q. Surprisingly strong effect of stabilizer on the properties of Au nanoparticles and Pt^Au nanostructures in electrocatalysis. *Nanoscale* **2010,** *2*, 2798-2804.

17. Grass, M. E.; Zhang, Y.; Butcher, D. R.; Park, J. Y.; Li, Y.; Bluhm, H.; Bratlie, K. M.; Zhang, T.; Somorjai, G. A. A Reactive Oxide Overlayer on Rhodium Nanoparticles during CO Oxidation and Its Size Dependence Studied by In Situ Ambient-Pressure X-ray Photoelectron Spectroscopy. *Angewandte Chemie International Edition* **2008,** *47*, 8893-8896.

18. Kedia, A.; Kumar, P. S. Solvent-Adaptable Poly(vinylpyrrolidone) Binding Induced Anisotropic Shape Control of Gold Nanostructures. *The Journal of Physical Chemistry C* **2012,** *116*, 23721-23728.

19. Pekcevik, I. C.; Poon, L. C. H.; Wang, M. C. P.; Gates, B. D. Tunable Loading of Single-Stranded DNA on Gold Nanorods through the Displacement of Polyvinylpyrrolidone. *Analytical Chemistry* **2013,** *85*, 9960-9967.

20. Herzing, A. A.; Carley, A. F.; Edwards, J. K.; Hutchings, G. J.; Kiely, C. J. Microstructural Development and Catalytic Performance of Au,àíPd Nanoparticles on Al2O3 Supports: The Effect of Heat Treatment Temperature and Atmosphere. *Chemistry of Materials* **2008,** *20*, 1492-1501.

21. Metin, O.; Sun, X.; Sun, S. Monodisperse gold-palladium alloy nanoparticles and their composition-controlled catalysis in formic acid dehydrogenation under mild conditions. *Nanoscale* **2013,** *5*, 910-912.

22. Kumar, D.; Chen, M. S.; Goodman, D. W. Synthesis of vinyl acetate on Pd-based catalysts. *Catalysis Today* **2007,** *123*, 77 - 85.

23. Corti, C. W.; Holliday, R. J.; Thompson, D. T. Progress towards the commercial application of gold catalysts. *Top Catal* **2007,** *44*, 331-343.

24. Iglesia, E.; Soled, S. L.; Fiato, R. A.; Via, G. H. Bimetallic Synergy in Cobalt Ruthenium Fischer-Tropsch Synthesis Catalysts. *Journal of Catalysis* **1993,** *143*, 345 - 368.

25. Bowker, M.; Morton, C.; Kennedy, J.; Bahruji, H.; Greves, J.; Jones, W.; Davies, P. R.; Brookes, C.; Wells, P. P.; Dimitratos, N. Hydrogen production by photoreforming of biofuels using Au, Pd and Au-Pd/TiO2 photocatalysts. *Journal of Catalysis* **2014,** *310*, 10 - 15.

26. Pongthawornsakun, B.; Fujita, S.-i.; Arai, M.; Mekasuwandumrong, O.; Panpranot, J. Mono- and bi-metallic Au–Pd/TiO2 catalysts synthesized by one-step flame spray pyrolysis for liquid-phase hydrogenation of 1-heptyne. *Applied Catalysis A - General* **2013,** *467*, 132 - 141.

27. Faria, J.; Ruiz, M. P.; Resasco, D. E. Phase-Selective Catalysis in Emulsions Stabilized by Janus Silica-Nanoparticles. *Advanced Synthesis & Catalysis* **2010,** *352*, 2359-2364.

28. Crossley, S.; Faria, J.; Shen, M.; Resasco, D. E. Solid Nanoparticles that Catalyze Biofuel Upgrade Reactions at the Water/Oil Interface. *Science* **2010,** *327*, 68-72.

29. Song, Y.; Liu, K.; Chen, S. AgAu Bimetallic Janus Nanoparticles and Their Electrocatalytic Activity for Oxygen Reduction in Alkaline Media. *Langmuir* **2012,** *28*, 17143-17152.

30. Song, Y.; Chen, S. Trimetallic Ag@AuPt Neapolitan nanoparticles. *Nanoscale* **2013,** *5*, 7284-7289.

31. Ferrer, D.; Torres-Castro, A.; Gao, X.; Sepúlveda-Guzmán, S.; Ortiz-Méndez, U.; José-Yacamán, M. Three-Layer Core/Shell Structure in Au-Pd Bimetallic Nanoparticles. *Nano Letters* **2007,** *7*, 1701-1705.

32. Zhang, J.; Lima, F. H. B.; Shao, M. H.; Sasaki, K.; Wang, J. X.; Hanson, J.; Adzic, R. R. Platinum Monolayer on Nonnoble Metal-Noble Metal Core-Shell Nanoparticle Electrocatalysts for O2 Reduction. *The Journal of Physical Chemistry B* **2005,** *109*, 22701-22704.

33. Tedsree, K.; Li, T.; Jones, S.; Chan, C. W. A.; Yu, K. M. K.; Bagot, P. A. J.; Marquis, E. A.; Smith, G. D. W.; Tsang, S. C. E. Hydrogen production from formic acid decomposition at room temperature using a Ag-Pd core-shell nanocatalyst. *Nature Nanotechnology* **2011,** *6*, 302 - 307.

34. Rothenberg, G., The Basics of Catalysis. In *Catalysis*, Wiley-VCH Verlag GmbH & Co. KGaA: 2008; pp 39-75.

35. Logadottir, A.; Rod, T. H.; Nørskov, J. K.; Hammer, B.; Dahl, S.; Jacobsen, C. J. H. The Brønsted–Evans–Polanyi Relation and the Volcano Plot for Ammonia Synthesis over Transition Metal Catalysts. *Journal of Catalysis* **2001,** *197*, 229 - 231.

36. Ruban, A.; Hammer, B.; Stoltze, P.; Skriver, H. L.; Nørskov, J. K. Surface electronic structure and reactivity of transition and noble metals. *Journal of Molecular Catalysis A: Chemical* **1997,** *115*, 421 - 429.

37. Bligaard, T.; Nørskov, J. K.; Dahl, S.; Matthiesen, J.; Christensen, C. H.; Sehested, J. The Brønsted–Evans–Polanyi relation and the volcano curve in heterogeneous catalysis. *Journal of Catalysis* **2004,** *224*, 206 - 217.

38. Rodriguez, J. A.; Goodman, D. W. The Nature of the Metal-Metal Bond in Bimetallic Surfaces. *Science* **1992,** *257*, 897- 903.

39. Aranda, D. A. G.; Schmal, M. Ligand and Geometric Effects on Pt/Nb2O5and Pt–Sn/Nb2O5Catalysts. *Journal of Catalysis* **1997,** *171*, 398 - 405.

40. Venezia, A. M.; La Parola, V.; Deganello, G.; Pawelec, B.; Fierro, J. L. G. Synergetic effect of gold in Au/Pd catalysts during hydrodesulfurization reactions of model compounds. *Journal of Catalysis* **2003,** *215*, 317 - 325.

41. Koh, S.; Strasser, P. Electrocatalysis on Bimetallic Surfaces: Modifying Catalytic Reactivity for Oxygen Reduction by Voltammetric Surface Dealloying. *Journal of the American Chemical Society* **2007,** *129*, 12624-12625.

42. Ferrer, D.; Blom, D. A.; Allard, L. F.; Mejia, S.; Perez-Tijerina, E.; Jose-Yacaman, M. Atomic structure of three-layer Au/Pd nanoparticles revealed by aberration-corrected scanning transmission electron microscopy. *Journal of Materials Chemistry* **2008,** *18*, 2442-2446.

43. Alayoglu, S.; Nilekar, A. U.; Mavrikakis, M.; Eichhorn, B. Ru-Pt core-shell nanoparticles for preferential oxidation of carbon monoxide in hydrogen. *Nature Materials* **2008,** *7*, 333 - 338.

44. Reifsnyder, S. N.; Lamb, H. H. Characterization of Silica-Supported Pd-Au Clusters by X-ray Absorption Spectroscopy. *The Journal of Physical Chemistry B* **1998,** *103*, 321 - 329.

45. Edwards, J. K.; Carley, A. F.; Herzing, A. A.; Kiely, C. J.; Hutchings, G. J. Direct synthesis of hydrogen peroxide from H2 and O2 using supported Au-Pd catalysts. *Faraday Discussions* **2008,** *138*, 225-239.

46. Yuan, D.; Gong, X.; Wu, R. Origin of High Activity and Selectivity of PdAu(001) Bimetallic Surfaces toward Vinyl Acetate Synthesis. *The Journal of Physical Chemistry C* **2008,** *112*, 1539-1543.

47. Solsona, B. E.; Edwards, J. K.; Landon, P.; Carley, A. F.; Herzing, A.; Kiely, C. J.; Hutchings, G. J. Direct Synthesis of Hydrogen Peroxide from H2 and O2 Using Al2O3 Supported Au-Pd Catalysts. *Chem Mater* **2006,** *18*, 2689-2695.

48. Coq, B.; Figueras, F. Bimetallic palladium catalysts: influence of the co-metal on the catalyst performance. *Journal of Molecular Catalysis A: Chemical* **2001,** *173*, 117 - 134.

49. Gao, F.; Goodman, D. W. Pd-Au bimetallic catalysts: understanding alloy effects from planar models and (supported) nanoparticles. *Chemical Society Reviews* **2012,** *41*, 8009-8020.

50. Enache, D. I.; Edwards, J. K.; Landon, P.; Solsona-Espriu, B.; Carley, A. F.; Herzing, A. A.; Watanabe, M.; Kiely, C. J.; Knight, D. W.; Hutchings, G. J. Solvent-Free Oxidation of Primary Alcohols to Aldehydes Using Au-Pd/TiO2 Catalysts. *Science* **2006,** *311*, 362-365.

51. Rebelli, J.; Detwiler, M.; Ma, S.; Williams, C. T.; Monnier, J. R. Synthesis and characterization of Au–Pd/SiO2 bimetallic catalysts prepared by electroless deposition. *Journal of Catalysis* **2010,** *270*, 224 - 233.

52. Mayrhofer, K. J. J.; Blizanac, B. B.; Arenz, M.; Stamenkovic, V. R.; Ross, P. N.; Markovic, N. M. The Impact of Geometric and Surface Electronic Properties of Pt-Catalysts on the Particle Size Effect in Electrocatalysis. *The Journal of Physical Chemistry B* **2005,** *109*, 14433-14440.

53. Tierney, H. L.; Baber, A. E.; Kitchin, J. R.; Sykes, E. C. H. Hydrogen Dissociation and Spillover on Individual Isolated Palladium Atoms. *Physical Review Letters* **2009,** *103*, 246102.

54. Nilekar, A. U.; Greeley, J.; Mavrikakis, M. A Simple Rule of Thumb for Diffusion on Transition-Metal Surfaces. *Angewandte Chemie International Edition* **2006,** *45*, 7046-7049.

55. Nasibulin, A. G.; Moisala, A.; Brown, D. P.; Kauppinen, E. I. Carbon nanotubes and onions from carbon monoxide using Ni(acac)2 and Cu(acac)2 as catalyst precursors. *Carbon* **2003,** *41*, 2711 - 2724.

56. Williams, D. B. C., C. Barry, *Transmission Electron Microscopy: A Textbook for Materials Science*. 2nd ed. ed.; Springer: 2009.

57. Akita, T.; Hiroki, T.; Tanaka, S.; Kojima, T.; Kohyama, M.; Iwase, A.; Hori, F. **2008,** *131*, - 97.

58. Hammer, B.; Morikawa, Y.; Nørskov, J. K. CO Chemisorption at Metal Surfaces and Overlayers. *Physical Review Letters* **1996,** *76*, 2141-2144.

59. Marx, S.; Krumeich, F.; Baiker, A. Surface Properties of Supported, Colloid-Derived Gold/Palladium Mono- and Bimetallic Nanoparticles. *The Journal of Physical Chemistry C* **2011,** *115*, 8195-8205.

60. Weimar, U. DRIFT Spectroscopy. http://weimar.ipc.uni-tuebingen.de/index.php?id=834 (accessed 16 March).

61. Newville, M. *Fundamentals of XAFS*; University of Chicago: Chicago, IL, July 23, 2004, 2004.

62. Bunker, G., Elements of XAFS. In *Physics Department, Illinois Institute of Technology*, pAPS XAFS School: Chicago, IL, 2005.

63. Venezia, A. M.; Parola, V. L.; Pawelec, B.; Fierro, J. L. G. Hydrogenation of aromatics over Au-Pd/SiO2-Al2O3 catalysts; support acidity effect. *Applied Catalysis A - General* **2004,** *264*, 43-51.

64. Liu, R. J.; Crozier, P. A.; Smith, C. M.; Hucul, D. A.; Blackson, J.; Salaita, G. Metal sintering mechanisms and regeneration of palladium/alumina hydrogenation catalysts. *Applied Catalysis A: General* **2005,** *282*, 111 - 121.

65. Lin, T.-B.; Chou, T.-C. Pd Migration. 1. A Possible Reason for the Deactivation of Pyrolysis Gasoline Partial Hydrogenation Catalysts. *Industrial & Engineering Chemistry Research* **1995,** *34*, 128-134.

66. Chen, J. J.; Ruckenstein, E. Role of interfacial phenomena in the behavior of alumina-supported palladium crystallites in oxygen. *The Journal of Physical Chemistry* **1981,** *85*, 1606-1612.

67. Gabasch, H.; Unterberger, W.; Hayek, K.; Klötzer, B.; Kleimenov, E.; Teschner, D.; Zafeiratos, S.; Hävecker, M.; Knop-Gericke, A.; Schlögl, R.; Han, J.; Ribeiro, F. H.; Aszalos-Kiss, B.; Curtin, T.; Zemlyanov, D. In situ XPS study of Pd(1 1 1) oxidation at

elevated pressure, Part 2: Palladium oxidation in the 10−1 mbar range. *Surface Science* **2006,** *600*, 2980 - 2989.

68. Wang, H.; Sun, Z.; Yang, Y.; Su, D. The growth and enhanced catalytic performance of Au@Pd core-shell nanodendrites. *Nanoscale* **2013,** *5*, 139-142.

69. Hilaire, L.; Leǵare, P.; Holl, Y.; Maire, G. Interaction of oxygen and hydrogen with Pd-Au alloys: An AES and XPS study. *Surface Science* **1981,** *103*, 125 - 140.

70. Cadle, S. H. Electrochemical oxidation of thin palladium films on gold. *Analytical Chemistry* **1974,** *46*, 587-590.

71. Xu, J. B.; Zhao, T. S.; Shen, S. Y.; Li, Y. S. Stabilization of the palladium electrocatalyst with alloyed gold for ethanol oxidation. *International Journal of Hydrogen Energy* **2010,** *35*, 6490 - 6500.

72. Gao, F.; Wang, Y.; Goodman, D. W. CO Oxidation over AuPd(100) from Ultrahigh Vacuum to Near-Atmospheric Pressures: The Critical Role of Contiguous Pd Atoms. *Journal of the American Chemical Society* **2009,** *131*, 5734-5735.

73. Wang, J. X.; Inada, H.; Wu, L.; Zhu, Y.; Choi, Y.; Liu, P.; Zhou, W.-P.; Adzic, R. R. Oxygen Reduction on Well-Defined Core-Shell Nanocatalysts: Particle Size, Facet, and Pt Shell Thickness Effects. *Journal of the American Chemical Society* **2009,** *131*, 17298-17302.

74. Yuan, D.; Gong, X.; Wu, R. Atomic configurations of Pd atoms in PdAu(111) bimetallic surfaces investigated using the first-principles pseudopotential plane wave approach. *Physical Review B* **2007,** *75*, 085428.

75. Lear, T.; Marshall, R.; Antonio Lopez-Sanchez, J.; Jackson, S. D.; Klapötke, T. M.; Bäumer, M.; Rupprechter, G.; Freund, H.-J.; Lennon, D. The application of infrared spectroscopy to probe the surface morphology of alumina-supported palladium catalysts. *The Journal of Chemical Physics* **2005,** *123*.

76. Borodko, Y.; Lee, H. S.; Joo, S. H.; Zhang, Y.; Somorjai, G. Spectroscopic Study of the Thermal Degradation of PVP-Capped Rh and Pt Nanoparticles in H2 and O2 Environments. *The Journal of Physical Chemistry C* **2009,** *114*, 1117-1126.

77. Tew, M. W.; Miller, J. T.; van Bokhoven, J. A. Particle Size Effect of Hydride Formation and Surface Hydrogen Adsorption of Nanosized Palladium Catalysts: L3 Edge vs K Edge X-ray Absorption Spectroscopy. *The Journal of Physical Chemistry C* **2009,** *113*, 15140-15147.

78. Zhao, C.; Gan, W.; Fan, X.; Cai, Z.; Dyson, P. J.; Kou, Y. Aqueous-phase biphasic dehydroaromatization of bio-derived limonene into *p*-cymene by soluble Pd nanocluster catalysts. *Journal of Catalysis* **2008,** *254*, 244-250.

79. Santana, J. A.; Rosch, N. Hydrogen adsorption on and spillover from Au- and Cu-supported Pt3 and Pd3 clusters: a density functional study. *Physical Chemistry Chemical Physics* **2012,** *14*, 16062-16069.

80. Buhl, D.; Roberge, D. M.; Hölderich, W. F. Production of p-cymene from α-limonene over silica supported Pd catalysts. *Applied Catalysis A: General* **1999,** *188*, 287 - 299.

81. Tang, M. L.; Liu, N.; Dionne, J. A.; Alivisatos, A. P. Observations of Shape-Dependent Hydrogen Uptake Trajectories from Single Nanocrystals. *Journal of the American Chemical Society* **2011,** *133*, 13220-13223.

82. Nag, N. K. A Study on the Formation of Palladium Hydride in a Carbon-Supported Palladium Catalyst. *The Journal of Physical Chemistry B* **2001,** *105*, 5945-5949.

83. Paál, Z.; Menon, P. G., *Hydrogen effects in catalysis: fundamentals and practical applications*. Marcel Dekker, Inc.: New York, 1988.

84. Boudart, M.; Hwang, H. S. Solubility of hydrogen in small particles of palladium. *Journal of Catalysis* **1975,** *39*, 44 - 52.

85. Daley, S. P.; Utz, A. L.; Trautman, T. R.; Ceyer, S. T. Ethylene Hydrogenation on Ni(111) by Bulk Hydrogen. *Journal of the American Chemical Society* **1994,** *116*, 6001-6002.

86. Benson, J. E.; Hwang, H. S.; Boudart, M. Hydrogen-oxygen titration method for the measurement of supported palladium surface areas. *Journal of Catalysis* **1973,** *30*, 146 - 153.

87. Kandoi, S.; Ferrin, P. A.; Mavrikakis, M. Hydrogen on and in Selected Overlayer Near-Surface Alloys and the Effect of Subsurface Hydrogen on the Reactivity of Alloy Surfaces. *Top Catal* **2010,** *53*, 384-392.

88. Okumura, K.; Amano, J.; Yasunobu, N.; Niwa, M. X-ray Absorption Fine Structure Study of the Formation of the Highly Dispersed PdO over ZSM-5 and the Structural Change of Pd Induced by Adsorption of NO. *The Journal of Physical Chemistry B* **2000,** *104*, 1050-1057.

89. McLellan, R. B.; Yoshihara, M. The thermodynamics of dilute solutions of hydrogen in palladium and its substitutional alloys. *Acta Metallurgica* **1987,** *35*, 197 - 225.

90. Luo, S.; Wang, D.; Flanagan, T. B. Thermodynamics of Hydrogen in fcc Pd-Au Alloys. *The Journal of Physical Chemistry B* **2010,** *114*, 6117 - 6125.

91. Doyle, A. M.; Shaikhutdinov, S. K.; Jackson, S. D.; Freund, H.-J. Hydrogenation on Metal Surfaces: Why are Nanoparticles More Active than Single Crystals? *Angewandte Chemie International Edition* **2003,** *42*, 5240-5243.

92. Khan, N. A.; Shaikhutdinov, S.; Freund, H. J. Acetylene and Ethylene Hydrogenation on Alumina Supported Pd-Ag Model Catalysts. *Catalysis Letters* **2006,** *108*, 159-164.

93. Clare, B. W.; Kepert, D. L. The optimal packing of circles on a sphere. *J Math Chem* **1991,** *6*, 325-349.

94. Cremer, P. S.; Somorjai, G. A. Surface science and catalysis of ethylene hydrogenation. *Journal of the Chemical Society, Faraday Transactions* **1995,** *91*, 3671-3677.

95. Mei, D.; Hansen, E. W.; Neurock, M. Ethylene Hydrogenation over Bimetallic Pd/Au(111) Surfaces: Application of Quantum Chemical Results and Dynamic Monte Carlo Simulation. *The Journal of Physical Chemistry B* **2002,** *107*, 798-810.

96.Stacchiola, D.; Tysoe, W. T. The effect of subsurface hydrogen on the adsorption of ethylene on Pd(1 1 1). *Surface Science* **2003,** *540,* L600 - L604.

97.Stacchiola, D.; Tysoe, W. T. The adsorption of ethylene on ethylidyne-covered Pd(111). *Surface Science Letters* **2002,** *513,* L431 - L435.

98.Yamauchi, M.; Kobayashi, H.; Kitagawa, H. Hydrogen Storage Mediated by Pd and Pt Nanoparticles. *Chem Phys Chem* **2009,** *10,* 2566-2576.

99.Zhang, S.; Metin, Ö.; Su, D.; Sun, S. Monodisperse AgPd Alloy Nanoparticles and Their Superior Catalysis for the Dehydrogenation of Formic Acid. *Angewandte Chemie International Edition* **2013,** *52,* 3681-3684.

Biography

Adria R. Wilson was born in Marlton, New Jersey on September 20, 1986, and graduated from Drexel University in Philadelphia, Pennsylvania in 2009 with a B.S. in Chemistry and minors in Political Science and Italian Studies. She began working on her PhD under Prof. Benjamin Wiley at Duke University in 2009, where she has researched the two-metal interactions of bimetallic nanoparticle catalysts. She has helped to author several articles regarding the interaction of Au and Pd in catalytic reactions, including "From Core-Shell to Alloys: The Preparation and Characterization of Solution-Synthesized AuPd Nanoparticle Catalysts" and "Synthesis and Catalytic Properties of Au–Pd Nanoflowers". She has also contributed to work involving the elucidation of copper nanowire growth, including the following publications: “Optically Transparent Water Oxidation Catalysts Based on Copper Nanowires” and "A rapid synthesis of high aspect ratio copper nanowires for performance transparent conducting films". As a graduate student, Adria has also received several academic honors. She is a NSF Graduate Research Fellow and a James B. Duke Fellow, and was also awarded a Pellham Wilder Fellowship and a Graduate Program Nanoscience Fellowship at various points during her time at Duke. She is the current treasurer of the Duke Materials Research Society student chapter, and has taken on varied roles as a member of the Duke student Phi Lambda Upsilon chapter (the national chemistry honors society); in turn playing the roles of co-president, travel grant chair, Hill lecture student co-chair, and event planner/caterer/barkeep. In 2013, Adria was chosen to accompany the U.S. delegation to the Lindau meeting of Nobel Laureates in Chemistry as a Young Researcher. Her first move as a doctor will likely be to adopt a lion-maned rabbit, and to name him Harold.